

# ***FY23 Status: Corrosion-Resistant Coatings on Spent Nuclear Fuel Canisters to Mitigate and Repair Potential Stress Corrosion Cracking***

## **Spent Fuel and Waste Disposition**

*Prepared for  
US Department of Energy  
Spent Fuel and Waste Science and  
Technology*

*Brendan Nation, Andrew Knight,  
Makeila Maguire, Samay Verma,  
Natalie Click, Gavin DeBrun, Tyler  
McCready, Ryan Katona, Rebecca  
Schaller, and Charles Bryan  
Sandia National Laboratories*

*August 10, 2023  
M3SF-23SN010207052  
SAND2023-09205R*



**DISCLAIMER**

This information was prepared as an account of work sponsored by an agency of the U.S. Government. Neither the U.S. Government nor any agency thereof, nor any of their employees, makes any warranty, expressed or implied, or assumes any legal liability or responsibility for the accuracy, completeness, or usefulness, of any information, apparatus, product, or process disclosed, or represents that its use would not infringe privately owned rights. References herein to any specific commercial product, process, or service by trade name, trademark, manufacturer, or otherwise, does not necessarily constitute or imply its endorsement, recommendation, or favoring by the U.S. Government or any agency thereof. The views and opinions of authors expressed herein do not necessarily state or reflect those of the U.S. Government or any agency thereof.

Sandia National Laboratories is a multi-mission laboratory managed and operated by National Technology & Engineering Solutions of Sandia, LLC., a wholly owned subsidiary of Honeywell International, Inc., for the U.S. Department of Energy's National Nuclear Security Administration under contract DE-NA0003525.



**Sandia National Laboratories**



**APPENDIX E**  
**NFCSC DOCUMENT COVER SHEET<sup>1</sup>**

Name/Title of

Deliverable/Milestone/Revision No. M3SF-23SN010207052: FY23 Status: Corrosion-Resistant Coatings on Spent Nuclear Fuel Canisters to Mitigate and Repair Potential Stress Corrosion Cracking

Work Package Title and Number: Canister Coatings for Prevention and Remediation- SNL: SF-23SN01020705

Work Package WBS Number: 1.08.01.02.07

Responsible Work Package Manager Andrew Knight Andrew Knight 8/10/2023  
(Name/Signature). Date Submitted

Quality Rigor Level for Deliverable/Milestone <sup>2</sup>	<input type="checkbox"/> QRL-1	<input type="checkbox"/> QRL-2	<input checked="" type="checkbox"/> QRL-3	<input type="checkbox"/> QRL-4
	<input type="checkbox"/> Nuclear Data			Lab QA Program <sup>3</sup>

This deliverable was prepared in accordance with \_\_\_\_\_ (Participant/National Laboratory Name)

QA program which meets the requirements of

- DOE Order 414.1       NQA-1       Other

**This Deliverable was subjected to:**

Technical Review

**Technical Review (TR)**

**Review Documentation Provided**

- Signed TR Report or,  
 Signed TR Concurrence Sheet or,  
 Signature of TR Reviewer(s) below

below

**Name and Signature of Reviewers**

Dominic Fascitelli

Peer Review

**Peer Review (PR)**

**Review Documentation Provided**

- Signed PR Report or,  
 Signed PR Concurrence Sheet or,  
 Signature of PR Reviewer(s)

*Dominic G. Fascitelli*

**NOTE 1:** Appendix E should be filled out and submitted with the deliverable. Or, if the PICS:NE system permits, completely enter all applicable information in the PICS:NE Deliverable Form. The requirement is to ensure that all applicable information is entered either in the PICS:NE system or by using the NFCSC Document Cover Sheet.

- In some cases there may be a milestone where an item is being fabricated, maintenance is being performed on a facility, or a document is being issued through a formal document control process where it specifically calls out a formal review of the document. In these cases, documentation (e.g., inspection report, maintenance request, work planning package documentation or the documented review of the issued document through the document control process) of the completion of the activity, along with the Document Cover Sheet, is sufficient to demonstrate achieving the milestone.

**NOTE 2:** If QRL 1, 2, or 3 is not assigned, then the QRL 4 box must be checked, and the work is understood to be performed using laboratory QA requirements. This includes any deliverable developed in conformance with the respective National Laboratory / Participant, DOE or NNSA-approved QA Program.

**NOTE 3:** If the lab has an NQA-1 program and the work to be conducted requires an NQA-1 program, then the QRL-1 box must be checked in the work Package and on the Appendix E cover sheet and the work must be performed in accordance with the Lab's NQA-1 program. The QRL-4 box should not be checked.

## **SUMMARY**

This report summarizes the activities performed by Sandia National Laboratories in FY23 to identify and test coating materials for the prevention, mitigation, and/or repair of potential chloride-induced stress corrosion cracking in spent nuclear fuel dry storage canisters. This work continues efforts by Sandia National Laboratories that are summarized in previous reports from FY20 through FY22 on the same topic [1-3]. In FY23, Sandia National Laboratories, in collaboration with five industry partners through a memorandum of understanding, evaluated the physical, mechanical, and corrosion-resistance properties of eight different coating systems. The evaluation included thermal and radiation environments relevant to various time periods of storage for spent nuclear fuel canisters. The coating systems include polymeric (polyetherketoneketone, modified polyimide/polyurea, modified phenolic resin, epoxy), organic/inorganic ceramic hybrids (silane-based polyurethane hybrid and a quasi-ceramic sol-gel polyurethane hybrid), and coatings utilizing a Zn-rich primer applied to stainless steel coupons. The results and implications of these tests are summarized in this report. These analyses will be used to identify the most effective coatings for potential use on spent nuclear fuel dry storage canisters and to identify specific needs for further optimization of coating technologies for application on spent nuclear fuel canisters.

The results obtained in FY23 have provided strong differentiation between coating types and their potential feasibility for use on SNF canisters with respect to thermal and radiation stability. Advances were made in the measurement of coating thermal behavior at canister-relevant temperatures, showing that most coatings outgas water or carbon dioxide and that some coatings did not outgas or react with the environment until extremely high temperatures – beyond the scope of this application. Further, mass loss for most coatings did not begin until well after 150°C which qualifies them (thermally) as a repair coating once the maximum surface temperature is below 150 °C. This serves as early evidence that coatings meet the “first, do no harm” criterion required to be considered for application on new or existing SNF canisters.

The influence of gamma radiation on the mechanical behavior of the coatings was mixed. For some coatings (OPM-23-01-XX, LUNA-23-04-XX, and TDA-23-02-XX), the coatings did not appear to be affected or were minimally affected by gamma radiation up to 1300 Mrad. OPM-23-01-XX did not fail during adhesion testing but showed increased surface bonding strength (between the test dolly and the coating) with increasing dose. When exposed to 100 Mrad, all the coatings (except for OPM-23-01-XX) exhibited >250 psi decrease in adhesion strength when compared to as-received coatings. The adhesion failure mode also varied in some coatings as a function of radiation.. In FY24, Sandia plans to continue lab-scale testing of the coating systems and will also begin considering canister-specific application parameters.

## **ACKNOWLEDGEMENTS**

This work was funded by the U.S. Department of Energy (DOE), Office of Nuclear Energy Spent Fuel and Waste Deposition Research and Development Program. The authors would like to thank Ned Larson of the DOE-NE for program oversight. In addition, the authors acknowledge the contributions to this report from Sandia National Laboratories personnel: Rachel Callaway and Elliot Fowler for surface cleaning prior to adhesion studies; Perla Salinas for the thermalgravimetric analysis; Brett Latter for taking photo of the samples; Don Hanson and Audrey Rotert for their help on the irradiation experiments; Melissa Mills for contributions to the hardness measurements; Dominic Fascitelli who performed the technical review and Scott Sanborn for additional review comments. The authors would also like to thank Oxford Performance Materials, Whitehorse R&D, Luna Labs USA, LLC., Flora Surfaces, and TDA Research Inc. for their review comments and participation in this program.

This page is intentionally left blank.

## CONTENTS

SUMMARY .....	iv
ACKNOWLEDGEMENTS .....	v
ACRONYMS .....	xv
1. INTRODUCTION .....	17
1.1 FY23 MOU Status.....	19
2. ANALYSIS COUPONS AND PARTNERSHIP DETAILS.....	21
2.1 Surface Treatment Witness Coupons .....	22
2.2 Coating Types .....	22
2.2.1 Polymeric Coatings .....	22
2.2.1.1 Polyetherketoneketone.....	22
2.2.1.2 Modified Polyimide-Polyurea-Phenolic Resin Coatings .....	24
2.2.1.3 TDA – Sherwin-Williams Macropoxy 646N with Corrosion Inhibitors .....	25
2.2.2 Organic-inorganic Hybrid Ceramic Coatings .....	27
2.2.3 Zn-Rich Primer Based Coatings for Galvanic Protection .....	30
2.2.4 Analysis Coupons .....	32
2.3 Down-Selection.....	34
2.3.1 Continued Evaluation of EIS Data from FY22 .....	34
2.3.2 Justification for Down-Selection .....	38
3. THERMAL EVALUATION.....	41
3.1 Thermogravimetric Analysis.....	41
3.2 Outgassing Analysis.....	46
3.3 Long-term Thermal Exposure .....	49
4. RADIATION STABILITY .....	51
4.1 Experimental Set up .....	52
4.2 Visual inspection and Color Change.....	57
4.3 Mechanical Testing .....	60
4.3.1 Hardness.....	61
4.3.2 Adhesion Tests.....	64
4.3.3 Scratch Tests .....	69
4.4 Electrochemical Properties.....	73
4.4.1 Chemical and Electrochemical Properties .....	73
5. FUTURE WORK .....	83
5.1 Isolated Coating Performance Tests.....	83
5.2 Simulated Application Testing.....	83
6. CONCLUSIONS AND IMPLICATION OF COATING PERFORMANCE FOR CANISTER USE .....	85

**FY23 Status: Corrosion-Resistant Coatings on Spent Nuclear Fuel Canisters to Mitigate and Repair Potential Stress Corrosion Cracking**

August 10, 2023

viii

---

7. REFERENCES .....	87
APPENDIX A .....	91



This page is intentionally left blank.

## LIST OF FIGURES

Figure 1. Schematic showing where the mitigation/repair work fits in to the overall SNF dry storage canister SCC research at SNL as well as how prevention, mitigation and repair differentiate.....	18
Figure 2. Image showing important considerations to determining if a coating could be effective for this application.....	19
Figure 3. Photobooth used to photograph the samples in a controlled light environment.....	21
Figure 4. Scanning white light interferometry data on a freshly abraded witness coupon. $R_a$ ranged from 180nm – 230 nm.....	22
Figure 5. Intake photos of OX-PEKK <sup>®</sup> coating samples OPM-23-01-01 provided by OPM. Also shown are basic attributes (approximate thickness, cure temperature, application methods, coating type, and number of components). <i>*Note: OPM-23-01-01 was not used as it appears to have cured at a higher temperature, therefore OPM sent OPM-23-01-11. Because there was delay in the receipt of the coatings, OPM-21-01-15 was used in the radiation studies.</i> .....	23
Figure 6. Intake photos of modified polyimide-polyurea-phenolic resin coating samples WHRD-21-02-XX and WHRD-21-03-XX provided by WHRD in FY21. Also shown are basic attributes (approximate thickness, cure temperature, application methods, coating type, and number of components). <i>*Note: No new samples were provided by WHRD in FY23, therefore untested samples from FY21 were used for radiation testing.</i> .....	25
Figure 7. Intake photos of modified Sherwin-Williams Macropoxy 646N with TDA corrosion inhibitor package, TDA-23-01-XX, provided by TDA in FY23. Also shown are basic attributes (approximate thickness, cure temperature, application methods, coating type, and number of components).....	26
Figure 8. Intake photos of the organic/inorganic quasi-ceramic coating samples FC-23-01-XX provided by FC. Also shown are basic attributes (approximate thickness, cure temperature, application methods, coating type, and number of components).....	28
Figure 9. Intake photos of samples of the organic/inorganic hybrid ceramic coating, LUNA-23-03-XX, provided by LUNA. Also shown are basic attributes (approximate thickness, cure temperature, application methods, coating type, and number of components). <i>*Note: These samples were not received in time for baseline photos to be taken, therefore some of the images shown have been exposed to radiation.</i> .....	29
Figure 10. Intake photos of samples of the organic/inorganic hybrid ceramic coating on top of a Zn-rich primer, LUNA-23-04-XX, provided by LUNA. Also shown are basic attributes (approximate thickness, cure temperature, application methods, coating type, and number of components). <i>*Note: These samples were not received in time for baseline photos to be taken, therefore some of the images shown have been exposed to radiation and/or a CPP scan.</i> .....	31
Figure 11. Intake photos of modified Sherwin-Williams Zn-Clad II with TDA corrosion inhibitor package, TDA-23-02-XX, provided by TDA in FY23. Also shown are basic attributes (approximate thickness, cure temperature, application methods, coating type, and number of components).....	32
Figure 12. Equivalent circuit used to fit all EIS data as an initial estimate in FY22. This equivalent circuit is commonly used to represent organic coatings on metallic	

substrates [56, 57]. The different electrical components are used as analogues to physical or electrochemical behavior of the coating system. ....35

Figure 13. Logarithm of mean total harmonic distortion (%) of the current response signal observed for baseline coatings as a function of the logarithm of the AC perturbation voltage frequency (Hz). The black horizontal line represents a 5% threshold for nonlinearity. The trends presented for baseline coatings persisted for 30-day and 90-day exposed coatings.....36

Figure 14. Logarithm of mean total harmonic distortion (%) of the perturbation voltage input signal observed for baseline coatings as a function of the logarithm of AC perturbation voltage frequency (Hz). The trends presented for baseline coatings persisted for 30-day and 90-day exposed coatings.....37

Figure 15. a) mudcracks that formed during the curing process of OPM-21-02-XX measured by profilometry, b) visual inspection of OPM-21-02-06 after 30 days at 76%RH/40°C with 300 μg/cm<sup>2</sup> ASW showing corrosion damage and delamination, and c) a close up of the corrosion damage following atmospheric exposure. ....38

Figure 16. Optical image of LUNA-21-05-02 (Zn-rich primer only) after scratch testing at 25N force. Adhesive failure occurred at <2N, and a subsequent scratch at a separation distance of 1 mm caused delamination of the coating between the scratches. A scratch performed using a separation distance of 5 mm did not cause delamination between scratches [1].....39

Figure 17. Table showing a qualitative rationale for the initial down-selection where green shows that the coating performance was “Good for this Application” and red means the observed coating performance “Could be Improved for this Application” with respect to a given test. The coating candidates in bold were selected to be evaluated in FY23.....40

Figure 18. Schematic modified from Gilkey, Brooks [10] showing the canister surface temperatures from horizontal and vertical canisters from 0 year to 30 years.....41

Figure 19. TGA data for all coatings expressed as % weight change. Coatings were tested to temperatures >225°C to determine onset of thermal breakdown. ....42

Figure 20. TGA data on all coatings expressed as % weight change. Temperatures above 225°C were tested to determine onset of material breakdown and do not correspond to any known application condition for SNF canisters. Canister surface temperatures (shown as vertical lines) were estimated from thermal models Gilkey, Brooks [10]. ....43

Figure 21. Weight change at 80°C, 150°C, 200°C and 225°C for all coatings. ....44

Figure 22. Mass-normalized heat flow (W/g) data collected during Thermogravimetric experiments. Samples were tested past 225°C to determine onset of phase changes or other thermodynamic events.....45

Figure 23. Residual Gas Analysis of exhaust stream during heating in TGA of various species with different atomic weights (in AMU).....47

Figure 24. Thermogravimetric mass % plotted with % species detected in the exhaust by residual gas analysis. Listed gas species are most probable detected species [65].....48

Figure 25. TGA mass % plotted with % oxygen detected in the exhaust by RGA for LUNA-23-04-10. Compressed air was used as a cover gas for the TGA measurement which has an oxygen concentration of 20.5% but since the RGA was not calibrated for high concentrations this data should be regarded as relative concentration only.....49

Figure 26. Estimated dose rate at a canister surface assuming 45-48 GWd/MTU (4% <sup>235</sup>U) burnup over a period of 300 years [66]. Test intervals were chosen based on realistic inspection intervals (such as the first inspection performed after 20 years of storage). .....51

Figure 27. Wooden fixtures used to hold coating specimens in front of the linear <sup>60</sup>Co array at Sandia’s Gamma Irradiation Facility. Thin gauge 304 stainless steel wire was used to prevent the specimens from falling into the containment pool and to hold the specimens flat against the fixture during exposure. Samples were wrapped in foil to prevent abrasion against the wire (not shown). .....54

Figure 28. a) The linear array and b) the shutter array at Sandia’s Gamma Irradiation Facility. Thermocouples were used to monitor the temperature of the sample stack during exposure using the shutter array. ....55

Figure 29. Stack temperature during exposure in the GIF shutter Array (dose rate 1054 rad/s). Stack 1 was removed after 93 hours (achieved 350 Mrad). Stack 2 (735 Mrad) was replaced and self-heated to the same temperature. ....56

Figure 30. Color comparison of coatings after exposure to increasing (left to right) doses of gamma radiation. These coupons exhibited the most obvious color changes, yellowing with increasing exposure. ....58

Figure 31. Colorimetric representation of baseline and gamma irradiated samples. Some coatings had high variability in baseline color while others exhibited yellowing with increasing dose. ....59

Figure 32. Colorimetric analysis of Red (a), Green (b), and Blue (c) color channels relative to baseline values. ....60

Figure 33. Leeb hardness values for all coatings before and after exposure to gamma radiation. LUNA-23-04 comprises LUNA-23-03 coated on top of a zinc rich primer underlayer. ....62

Figure 34. Nanoindentation data from two coatings exposed to gamma radiation. Samples generally exhibited softening with increasing dose. ....63

Figure 35. Average pull off pressure (psi) as a function of coating type with clustered columns of total radiation exposure (Mrad). ....66

Figure 36. Adhesion value change for each coating with respect to baseline, unirradiated coatings. Each sample group is organized by increasing dose (left to right). High positive change in adhesion for OPM-23-01 represents an increase in surficial bond between adhesion test dolly and coating surface but does not represent an increase in actual adhesion strength. ....67

Figure 37. Photo showing the type of failure observed during the adhesion tests for TDA-23-01-XX as a function of radiation. ....68

Figure 38. Photo showing the type of failure observed during the adhesion tests for FC-23-01-XX as a function of radiation. ....69

Figure 39. Images of scratches performed on TDA-23-01-XX after irradiation. Scratch areas were calculated in Bluebeam Inc. image processing software by outlining the plastically deformed area. ....70

Figure 40. Stiffness vs gamma radiation dose derived from scratch testing data for three polymeric coatings. ....71

Figure 41. Scratch area vs average stiffness for TDA-23-01-XX. Scratch area was measured from image data. Decreased scratch area represents an increase in material stiffness. ....72

---

Figure 42. Three-electrode electrochemical cell for electrochemical measurements.....	73
Figure 43. Polarization scans of FC-23-01-XX following gamma irradiation to a) 0 Mrad, b) 105 Mrad-LA, c) 211 Mrad-LA, c) 350 Mrad-LA, e) 351 Mrad-SA, f) 724 Mrad-SA, and g) 1305 Mrad-SASA.....	75
Figure 44. Polarization scans of LUNA-23-03-XX following gamma irradiation to a) 0 Mrad, b) 105 Mrad-LA, c) 211 Mrad-LA, c) 350 Mrad-LA, e) 351 Mrad-SA, f) 724 Mrad-SA, and g) 1305 Mrad-SA.....	77
Figure 45. Polarization scans of LUNA-23-04-XX following gamma irradiation to a) 0 Mrad, b) 105 Mrad-LA, c) 211 Mrad-LA, c) 350 Mrad-LA, e) 351 Mrad-SA, f) 724 Mrad-SA, and g) 1305 Mrad-SA.....	79
Figure 46. Polarization scans of TDA-23-02-XX following gamma irradiation to a) 0 Mrad, b) 105 Mrad-LA, c) 211 Mrad -LA, c) 350 Mrad- LA, e) 351 Mrad -SA, f) 724 Mrad -SA, and g) 1305 Mrad-SA.....	81
Figure 48. Qualitative comparison of results to date on all coatings.....	86

---

## LIST OF TABLES

Table 1. Details of the coating candidates. The coupon candidates in bold were downselected and evaluated in FY23.....	33
Table 2. Experimental tests performed on each coupon provided by the vendors for FY23 samples. ....	34
Table 3. Residual Gas Analysis spectra atomic weights and probable corresponding species [65].....	47
Table 4. Gamma Irradiation Test Matrix .....	52
Table 5. Nanoindentation summary data on gamma irradiated coatings.....	63
Table 6. Detailed summary of the adhesion tests as a function of radiation for the zinc rich coatings candidates. ....	65
Table 7. Detailed summary of the adhesion tests as a function of radiation for the ceramic coating candidates. ....	65
Table 8. Detailed summary of the adhesion tests as a function of radiation for the polymer coating candidates. ....	66

## ACRONYMS

AC	alternating current
AFM	atomic force microscopy
ANSI	American National Standards Institute
ASW	artificial seawater
ASME	American Society of Mechanical Engineers
ASTM	American Society for Testing and Materials
AMU	atomic mass unit
CISCC	chloride-induced stress corrosion cracking
COTS	commercial-off-the-shelf
CPE	constant phase elements
CPP	cyclic potentiodynamic polarization
DCS	differential scanning calorimetry
DI	deionized [water]
DOE	Department of Energy
DSC	differential scanning calorimetry
EIS	electrical impedance spectroscopy
EOY	end of year
EPRI	Electric Power Research Institute
FC	Flora Surfaces
FY	fiscal year
GIF	Gamma Irradiation Facility
HAZ	heat affected zone
ISFSI	independent spent fuel storage installation
LA	linear array
LUNA	Luna Labs USA, LLC
MOU	memorandum of understanding
NE	Office of Nuclear Energy
NEUP	Nuclear Energy University Programs
NSD	non-stationary distortion
OCP	open circuit potential
OPM	Oxford Performance Materials
PAEK	polyaryletherketone
PEKK	polyetherketoneketone

---

PNNL	Pacific Northwest National Laboratory
R <sub>a</sub>	average roughness
RH	relative humidity
SA	shutter array
SC	solution cast
SCC	stress corrosion cracking
SEM	scanning electron microscope
SFWD	Spent Fuel and Waste Disposition
SNF	spent nuclear fuel
SNL	Sandia National Laboratories
SS	stainless steel
TDA	TDA Research
TGA	thermogravimetric analysis
THD	total harmonic distortion
TML	total mass loss
TOF	time of flight
TRL	technology readiness level
WHRD	White Horse Research and Development



## **SPENT FUEL AND WASTE SCIENCE AND TECHNOLOGY**

# **FY23 STATUS: CORROSION-RESISTANT COATINGS ON SPENT NUCLEAR FUEL CANISTERS TO MITIGATE AND REPAIR POTENTIAL STRESS CORROSION CRACKING**

This report fulfills milestone M3SF-23SN010207052 in the SCC Canister Coatings for Prevention and Mitigation work package (SF-23SN010207051). This work was sponsored under the Department of Energy's (DOE) Office of Nuclear Energy (NE) Spent Fuel and Waste Disposition (SFWD) campaign.

## **1. INTRODUCTION**

As the time period for spent nuclear fuel (SNF) in dry storage continues to increase, the need to develop potential mitigation and repair technologies to protect against possible stress corrosion cracking (SCC) continues to grow. This report summarizes the work performed by Sandia National Laboratories (SNL) to evaluate the performance of several commercially available coating systems against canister-relevant conditions. Specifically, in FY23 SNL focused on developing a better understanding of the ability of each of the coating systems to withstand radiation and thermal environments that could be experienced at different storage times and heat loads. This work builds off previous research performed in FY22, which evaluated coating performance when exposed to a corrosive atmospheric environment. Collectively, these results continue to provide the necessary data and methodologies to identify if a possible coating system could be used to prevent, mitigate, or repair possible SCC on an SNF canister.

For SCC to be ,occur three criteria must be met; 1) a susceptible material must be present, 2) sufficient tensile stresses must exist, and 3) a corrosive environment must persist. Because the SNF is stored in welded stainless steel (SS) canisters, it is known that the material is susceptible and that the necessary stresses are present [4-10]. Therefore, if the state of the canister allows for a corrosive brine, to form then the criteria are met and SCC is possible. This is because passive ventilation cools SNF dry storage canisters within their overpacks, allowing dust and salts to deposit onto the surface during storage at independent spent fuel storage installations (ISFSIs) located across the United States [11-15]. As storage times increase, the possibility for a corrosive brine to exist on the canister surface increases. Initially, the hot surface temperature of the canister prevents salt deliquescence from occurring due to the low relative humidity (RH); however, as the canister surface cools over time, the near-surface RH will increase and allow for salt deliquescence to occur [6, 11-14, 16-23]. In marine and near-marine environments, deliquescence of sea salt aerosols results in the formation of chloride-rich corrosive brines. Specifically, a saturated  $MgCl_2$  brine is the first sea salt brine to form as the mineral bischofite deliquesces at an RH of ~36 % and could form within 50 years of storage at some ISFSIs and canister locations [10, 24]. Currently, storage times have surpassed 25 years for some existing dry storage canisters, signifying that it is imperative to identify and implement solutions to prevent, mitigate, or repair possible SCC.

The DOE is working to address the potential occurrence of SCC by developing an understanding of the factors that control the timing and location of crack formation and growth [4-9]. This work informs testing environments, susceptible canister regions, and the relationship between brine chemistry and SCC. Figure 1 shows how mitigation and repair work fits into the larger SNL SCC program as well as how prevention, mitigation, and repair differentiate from each other in terms of what is occurring on the canister surface. The timing of a permanent disposal pathway for SNF remains uncertain and performance requirements for dry storage canisters are expected to exceed—or have already exceeded—their original 20- to 40-year licensing periods [25, 26]. The likelihood of a stable, corrosive, Cl-rich surficial brine increases as storage times increase. Thus, it is becoming increasingly important to consider methods to

prevent, mitigate, and/or repair potential SCC on existing and future dry storage canisters.

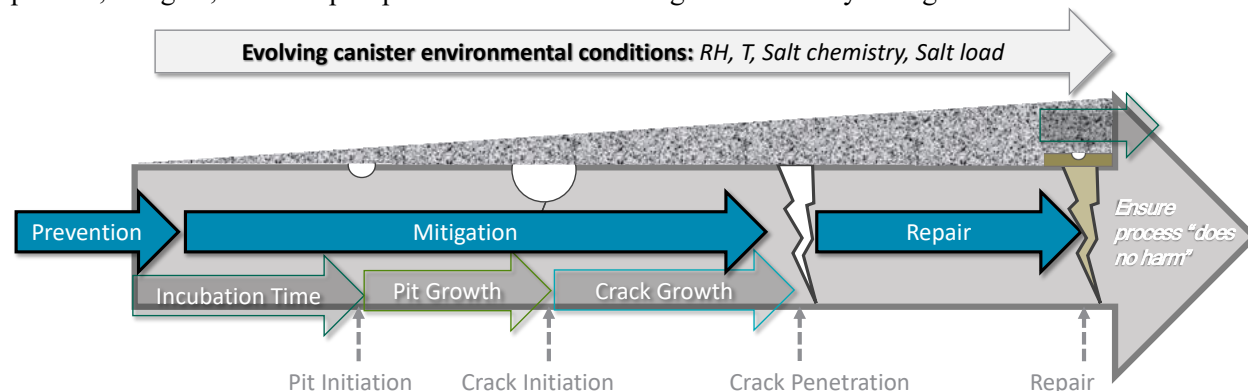


**Figure 1. Schematic showing where the mitigation/repair work fits in to the overall SNF dry storage canister SCC research at SNL as well as how prevention, mitigation and repair differentiate.**

Recent efforts by SNL and others—including other DOE National Laboratories, universities through Nuclear Energy University Program (NEUP) projects, and the Electrical Power Research Institute (EPRI)—have worked to develop a deeper understanding of possible ways to mitigate and repair SNF canisters [2, 3, 25, 27-30]. Specifically, in FY20 SNL produced a report summarizing a literature survey on possible common coating technologies for use on SNF canisters [3]. In FY21, SNL presented the framework for an SNL/industry collaboration through a memorandum of understanding (MOU) to investigate corrosion-resistant coatings for their viability for use on SNF canisters [2]. In FY22, SNL evaluated coatings for their performance with respect to mechanical durability and exposure to an atmospheric corrosive environment [30]. In FY23, SNL evaluated the performance of an updated set of samples for radiation testing, thermal testing, and more in-depth electrochemical testing. Progress in this work and considerations for testing are shown in Figure 2. To date, SNL has made progress evaluating *corrosion resistance* properties, *mechanical durability*, *thermal resistance*, and *radiation resistance*. This information has been used to inform down-selection and to develop a clear understanding of coating characteristics and properties acceptable for this application.

The timing of when a coating is applied to an SNF canister will determine the environment that the coating will experience. For example, if a coating is applied for **prevention** of SCC, it could be applied during manufacture of a new canister prior to loading the fuel. In this case, the coating would experience the highest thermal load (>250 °C in some locations [10]), radiation dose (>2 rad/sec [31]), and need to be robust enough to be transported and placed in the overpack for dry storage. Alternatively, if a coating is to be used for **mitigation** or **repair** on an existing canister, the thermal, radiation, and mechanical durability requirements may be less stringent—depending on how much time has passed—due to radioactive decay of the fuel resulting in a lower radiation flux and surface temperature. While the timing of coating application will determine the severity of the radiation and thermal environment, in all cases an applied coating must demonstrate the ability to withstand a known radiation dose and the thermal properties must be known. An in-depth understanding of these properties would aid in identifying how a given coating could be successful for this application.

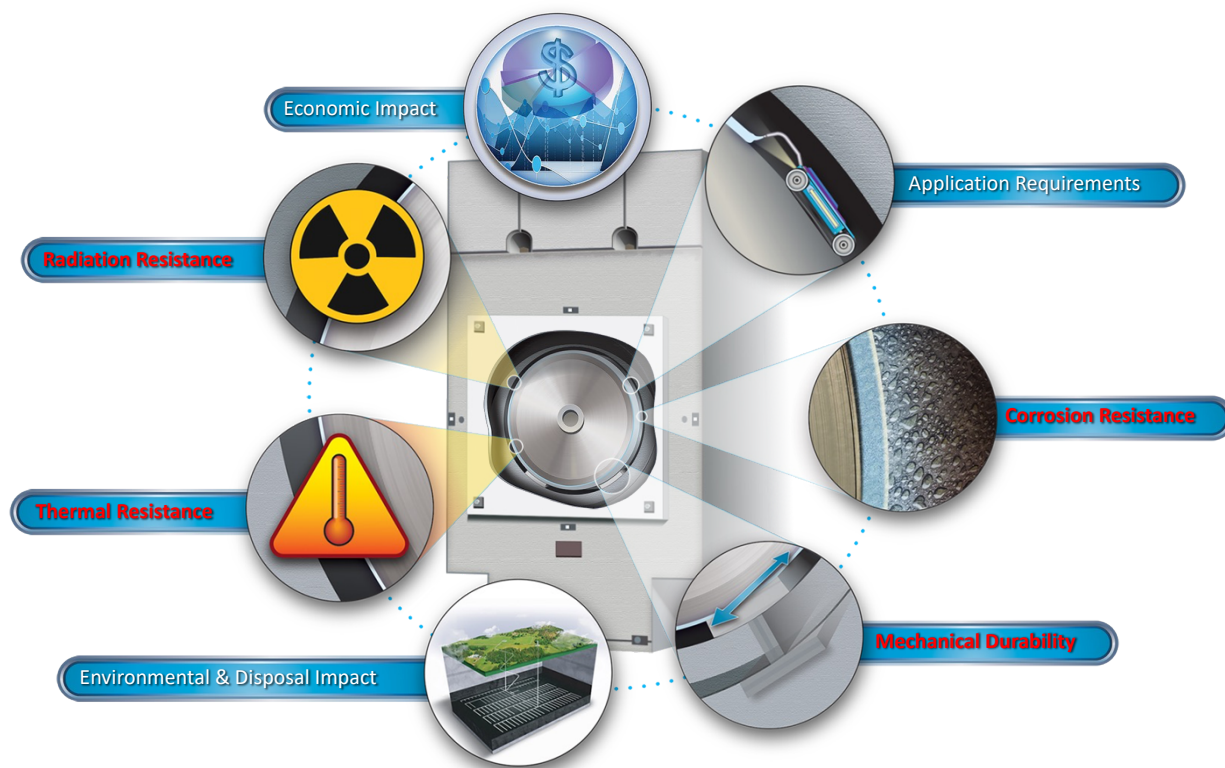


Figure 2. Image showing important considerations to determining if a coating could be effective for this application.

## 1.1 FY23 MOU Status

In the MOU created in FY21, three phases were defined to evaluate the ability of a given coating for use on an SNF canister. These phases are described in detail in our FY21 report [2] and are briefly defined as; **Phase 1: Baseline evaluation of physical, mechanical, and corrosion-resistant properties, Phase 2: Stability under canister-relevant environments, and Phase 3: Coating application considering specific limitations of each implementation scenario.** The work described in this report aligns with the goals and objectives of Phases 1 & 2. Specifically, the FY23 coating candidates were down-selected based on evaluations during Phase 1 testing in FY22. In FY23, two new coating candidates were provided by TDA and the down-selected coatings were provided to SNL as sample coupons by each of the vendors (*Note: No new samples were received from White Horse Research and Development (WHRD)*), and these FY23 coupons were evaluated for their radiation stability and thermal properties under canister-relevant conditions. The FY23 coatings candidates are described in detail in Section 2.2 and previous reports [1, 2]. The goal of Phase 2 is to test the coatings under more rigorous, canister-relevant scenarios to gain a better understanding of their performance as a prevention, mitigation, or repair technology for this application. Based on the results of Phase 2 testing, further down-selection will be performed to move the most applicable coatings to Phase 3. For this work, participating industry partners coated 10 SS coupons in FY23. Each vendor was given specific surface finish specifications and was provided the materials to prepare the surface. This was done to evaluate all coating candidates on the same surface roughness. Once the samples were received, they were either subjected to irradiation or thermal evaluation testing. The post-radiation or thermal exposure coating properties were evaluated by several different physical and chemical methods, including hardness, scratch, adhesion, and electrochemical tests.

This page is intentionally left blank.

## **2. ANALYSIS COUPONS AND PARTNERSHIP DETAILS**

Following discussions with the coating vendors and the initial down-selection, each participating vendor coated ten coupons with the FY23 coating variants. As in FY22, coatings were applied to  $3 \times 6$  in. rectangular SS coupons provided to each vendor by SNL accompanied by the necessary materials and procedure for proper surface preparation. The coupons were produced from the same sheet of 0.065 in. thick 304L SS. The surface finishes of the bare coupons were characterized by optical profilometry prior to sending to the vendors [2]. Each coupon had a face with a rough surface finish and a #8 mirror-polished side. A static-cling film was applied to both sides to protect the coupon surfaces during preliminary handling and shipping. The static cling film on the mirror-polished side was removed prior to surface preparation. Each coupon was abraded uniformly with 180-grit sandpaper and cleaned with organic solvents immediately prior to coating. The surface preparation method was tightly controlled to ensure accurate comparison of coating adhesion behavior.

All coatings were tested using identical thermal and radiation exposure methods and were evaluated for the same mechanical and electrochemical performance metrics. Coatings will be referenced in this text using a simple alphanumeric nomenclature combining the manufacturer name with a variant number in the format of “VENDOR-YEAR-VARIANT#-COUPON#”. When possible, the variant number remained consistent with the FY21 samples. For example, the first coupon of the third variant provided by LUNA in FY23 would be “LUNA-23-03-01” and is the same type of coating as LUNA-21-03-XX provided in FY21. The list of coatings, variants, and other details is given in Section 2.2.

Upon receipt of the coatings, intake photos were taken for baseline measurements of color and appearance. This was done using a method consistent with the details provided in the FY22 report [1]. A picture of this photography set up is shown in Figure 3. Results from the colorimetric study are discussed in section 4.2.

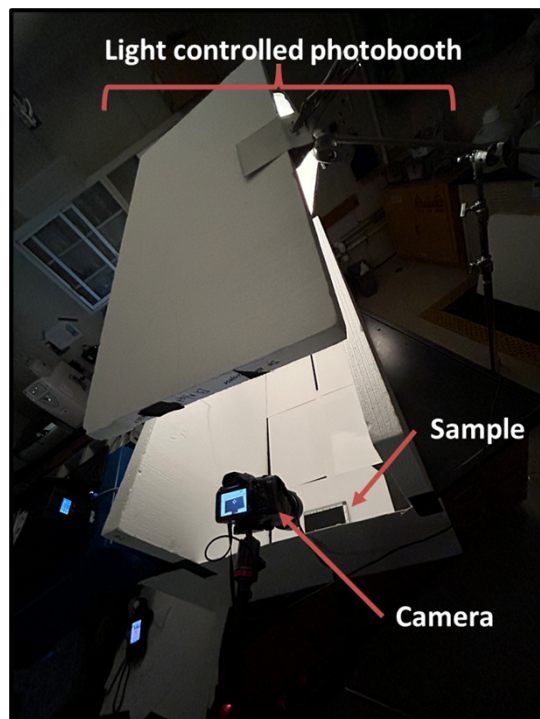


**Figure 3. Photobooth used to photograph the samples in a controlled light environment.**

## 2.1 Surface Treatment Witness Coupons

Surface finish witness coupons were created using the procedure described in Section 0 and imaged using a scanning white light interferometer. Figure 4 shows the interferometer data on a freshly abraded coupon. The average roughness ( $R_a$ ) of the witness coupon ranged from 180 nm to 230 nm, corresponding to a 180-grit sandpaper. This roughness corresponds to what has been previously observed on the surface of a new, unloaded dry storage canisters [32] and is also what the coatings manufacturers agreed should result in the best possible adhesion.

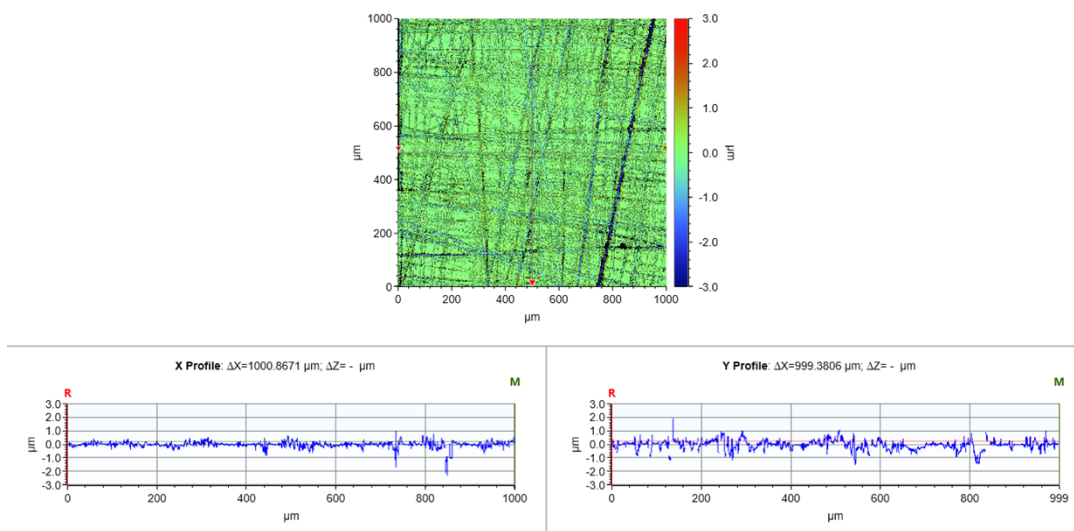


Figure 4. Scanning white light interferometry data on a freshly abraded witness coupon.  $R_a$  ranged from 180nm – 230 nm.

## 2.2 Coating Types

In FY23, SNL continued to work with Oxford Performance Materials (OPM), White Horse Research and Development (WHRD), Luna Labs (LUNA), and Flora Surfaces (FC). In addition to these collaborating partners, SNL also initiated a collaboration with TDA Research (TDA). The coating candidates fell into three categories: polymeric (Section 2.2.1), organic-inorganic hybrid coatings (Section 2.2.2), and coatings that offer galvanic protection utilizing a Zn-rich primer (Section 2.2.3). Some of the coatings evaluated in FY22 were not selected for further evaluation in FY23. The rationale for the down-selection of each coating is found in Section 2.3. The following sections describe the details of each of the coating systems evaluated in FY23.

### 2.2.1 Polymeric Coatings

OPM, TDA, and WHRD proposed polymeric coating systems for use on SNF canisters for prevention, mitigation, and/or repair of potential SCC. In total, there are seven polymeric variants for experimental investigation during tests from FY21-FY23. Of the seven polymeric coatings, 2 of them were not selected for consideration in FY23 – the remaining five were rigorously tested in thermal and radiation environments.

#### 2.2.1.1 Polyetherketoneketone

As described in the FY22 report, OPM provided two variant coatings of their PEKK based coating that differ in deposition method, physical properties, and appearance [1]. The variants provided by OPM were OX-PEKK®-Resin powder coat (OPM-21-01-XX and OPM-23-01-XX), which is applied via electrostatic deposition, fluidized bed, and thermal spray methods, and the OX-PEKK®-SC (OPM-21-02-XX), where

the “SC” refers to solution cast. The OX-PEKK®-SC (OPM-21-02-XX) was not selected for continued evaluation in FY23. For FY23, OPM provided 10 new coupons of OPM-23-01-XX, which are shown in Figure 5. Visually, the OPM-23-01-XX coated samples appear similar to the previous set (OPM-21-01-XX) and have a brown/red/gold appearance. There appeared to be a bit more variability in color for the OPM-23-01-XX samples. This was possibly due to different thicknesses or curing temperatures. It is unclear at this point how these color variations impact the performance. Specifically, OPM-23-01-01 was a deeper red than the rest of the samples. It was confirmed by OPM that this sample was cured at a higher temperature—this sample was not included in any analysis. Overall, the coating appears smooth, but has small, randomly distributed bubble-like features, which likely formed during the curing process. SNL did not receive all of the coatings from OPM prior to the radiation exposure tests; therefore, a sample from FY21 was included in the radiation experiment.

Specific properties of PEKK coatings have been discussed in previous end of year (EOY) reports [1, 2]. Briefly, PEKK belongs to the polyaryletherketone (PAEK) polymer family and are well recognized as effective anti-corrosion materials [33, 34]. Within the PAEK family, PEKK is a semi-crystalline polymer material with robust chemical, thermal, radiation, and mechanical properties. The surface energy of PEKK (both in the melt and solid) facilitates wetting and enables load transfer and increased continuity between the PEKK and the substrate [35, 36]. Application of PEKK coatings could be viable for **prevention, mitigation, or repair** scenarios, though application methods may limit its utility for **repair**.



**Figure 5. Intake photos of OX-PEKK® coating samples OPM-23-01-01 provided by OPM. Also shown are basic attributes (approximate thickness, cure temperature, application methods, coating type, and number of components). *\*Note: OPM-23-01-01 was not used as it appears to have cured at a higher temperature, therefore OPM sent OPM-23-01-11. Because there was delay in the receipt of the coatings, OPM-21-01-15 was used in the radiation studies.***

### **2.2.1.2 Modified Polyimide-Polyurea-Phenolic Resin Coatings**

In total, WHRD provided 3 variants of their organic coatings. The variants are WHRD-21-01-XX or CrackStop® (polyimide-polyurea composite), WHRD-21-02-XX or GammaBlock® (polyimide-polyurea composite), and WHRD-21-03-XX or GammaBlock®*Plus* (phenolic infused polyurea resin which can be loaded with solid particles for improved radiation resistance). No new coating samples were provided by WHRD for FY23 and only WHRD-21-02-XX and WHRD-21-03-XX were selected to continue testing for FY23. Specific details about these coatings can be found in the FY22 report [1]. Visually, the WHRD coating variants look nearly identical apart from the thickness (Figure 6), where WHRD-21-03-XX is thicker than WHRD-21-02-XX. The surface features exhibit visible topographic deviations and crevices. These composite coatings consist of a modified polyimide combined with polyurea and phenol monomer groups with additional functionalization to allow for property tunability to target specific coating properties. Briefly, these composite coatings are widely used industrially and are known for their light weight, great flexibility, thermal stability, and chemical resistance [37, 38]. Specifically, the polyimide component provides a large service temperature range (-300 °C to 300 °C), enhanced electrical insulation (dielectric constant = 3.4 – 3.5), and robust tensile strength after thermal and radiation exposures [38-40]. The polyurea components have a highly developed H-bonding network that reduces the porosity and results in high mechanical strength and barrier properties [41]. Polyimide and polyurea copolymers have a synergistic behavior that is understood to result from the H-bonding acceptor of the polyimides and the H-bonding donor in polyurea, which results in precisely controlled intra- and inter-hydrogen bonding and can result in induced self-assembly [42-44]. Enhanced H-bonding interactions can reduce the surface energy and yield a more compact morphology to reduce the permeability of ionic species [42]. Phenolic resins have been used as corrosion-resistant coatings and have demonstrated excellent thermal resistance (>300 °C) and chemical resistance to salts, non-oxidizing inorganic acids, and other solvents. However, unmodified phenolic resins are brittle and do not perform well under mechanical stress [45].



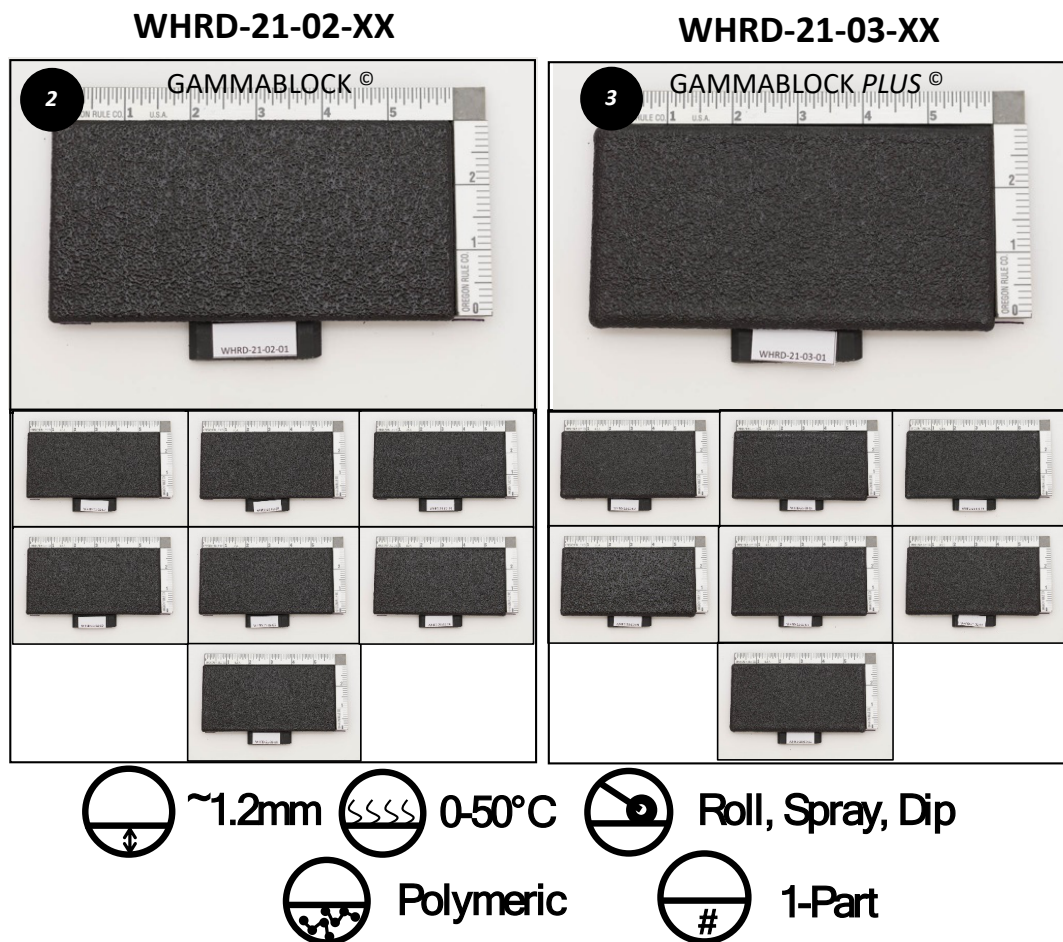


Figure 6. Intake photos of modified polyimide-polyurea-phenolic resin coating samples WHRD-21-02-XX and WHRD-21-03-XX provided by WHRD in FY21. Also shown are basic attributes (approximate thickness, cure temperature, application methods, coating type, and number of components). \*Note: No new samples were provided by WHRD in FY23, therefore untested samples from FY21 were used for radiation testing.

### 2.2.1.3 TDA – Sherwin-Williams Macropoxy 646N with Corrosion Inhibitors

TDA provided one polymeric coating for this work in FY23. This coating is a polyamide epoxy coating that contains TDA proprietary corrosion inhibitors. Specifically, the coating is a modified Sherwin-Williams Macropoxy 646N that contains additional corrosion resistant inhibitors incorporated by TDA and was called “Coating A” by TDA. For this work, the coating can be identified as TDA-23-01-XX and can be seen in Figure 7. Visually, TDA-23-01-XX is a white coating with a surface comparable to the WHRD samples, including visible topographic deviations and crevices. The thickness was not measured by SNL but was provided by TDA. The coating was applied to the coupon using a compressed air paint gun following surface cleaning with acetone and isopropyl alcohol. The coating was cured at 20-25°C. The sample-to-sample variability was low.

Epoxy coatings were identified in the FY20 scoping report as a possible solution for prevention, mitigation, or repair of SCC in SNF canisters. Importantly, it was stated that more research would be required to better understand the radiation stability and thermal properties—specifically thermal expansion coefficient [3]. The Sherwin-Williams Macropoxy 646N has been widely used as a protective

coating in marine settings and in the nuclear industry [46]. Specifically, the Sherwin-Williams Macropoxy 646N has been certified to meet the requirements of ANSI/ASME NQA-1 and 10 CFR Part 50 Appendix B for use in nuclear power plants and fuel reprocessing facilities. More specifically, the Macropoxy 646N met the design requirements for gamma radiation for use in nuclear power plants (ASTM D4082) [47]. Generally, air dried epoxy coatings can offer high mechanical robustness, as evidenced by a Young's Modulus of ~2.4 GPa and tensile strength ~75- 80 MPa [48-50]. Additionally, air dried epoxies have been shown to have great chemical stability in atmospheric and marine conditions and can be easily applied to a variety of different surfaces [51]. Application of epoxy coatings could be viable for **mitigation** or **repair** scenarios once the canister has cooled and is less radioactive.

**TDA-23-01-XX**

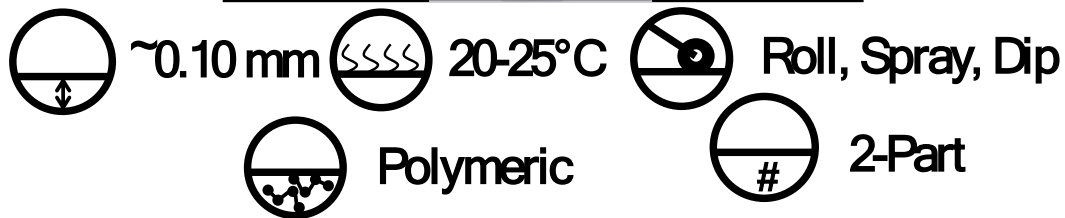
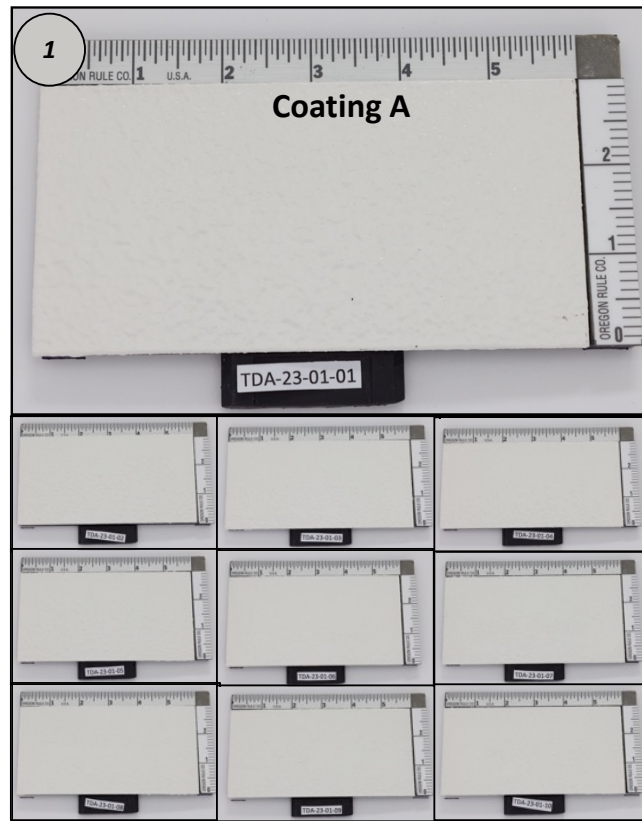


**Figure 7. Intake photos of modified Sherwin-Williams Macropoxy 646N with TDA corrosion inhibitor package, TDA-23-01-XX, provided by TDA in FY23. Also shown are basic attributes (approximate thickness, cure temperature, application methods, coating type, and number of components).**

## **2.2.2 Organic-inorganic Hybrid Ceramic Coatings**

LUNA and FC proposed similar coatings comprised of organic-inorganic hybrid ceramic coatings. These coatings consist of a silica-based ceramic components and an organic polyurethane linker to increase the coating flexibility. In total, there were three different hybrid ceramic coatings under investigation with varying amounts of organic and inorganic components. In FY23, the FC coating and one of the LUNA coatings were selected for continued evaluation. The coatings selected were FC-23-01-XX and LUNA-23-03-XX, where the FC-23-01-XX had the highest organic component, and the LUNA-23-03-XX had the highest inorganic component. The LUNA-21-01-XX coating was not evaluated in FY23, as it was similar to the FC coating.

As described in the FY22 report, the hybrid ceramic coatings contain a polyurethane polymeric linker that resulting in superior corrosion resistance via increased chemical bonding between organic and inorganic components and improved chemical and physical stability [1]. While the incorporation of an organic component to a ceramic coating can improve some properties, it also could make the coating more susceptible to radiation or thermal damage [3, 52]. In the FY20 scoping report, a polyurethane coating was considered nonviable due to issues of thermal expansion which may cause delamination [3]. Hybrid ceramic coatings can alter the physical properties of the coating compared to the organic component alone; therefore, it is unknown if thermal issues are alleviated when polyurethane is combined with a ceramic coating.

In FY23, SNL continued evaluation of the FC-proposed candidate, CLADCO™. CLADCO™ is described as a single component polyurethane polymer linker and a silica-based sol-gel quasi-ceramic component. CLADCO™ is commercially available, as a low viscosity liquid that can be easily applied—using spraying or brushing—to a wide array of substrates and dried under ambient conditions without the need for external heating [1], though it is unknown the impact of curing at higher temperatures. The resulting coating was shown to be a thin, chemically inert, with a hydrophobic surface with decent adhesion properties on SS, though the impact of atmospheric exposure decreased the adhesion properties significantly [1]. The samples provided to SNL by FC in FY23 were applied via spray coating and are shown in Figure 8. Visually, the FY23 samples appear different than the FY21 samples. This may be due to the differences in the surface preparation, as the surface preparation requirements in FY23 were more specific than FY21 coatings. Application of FC-21-01 could be viable for **in situ repair** so long that the coating can be effectively cured at elevated temperatures. It is likely not viable for **ex situ** methods due to the mechanical properties (i.e., prone to scratching).

FC-23-01-XX

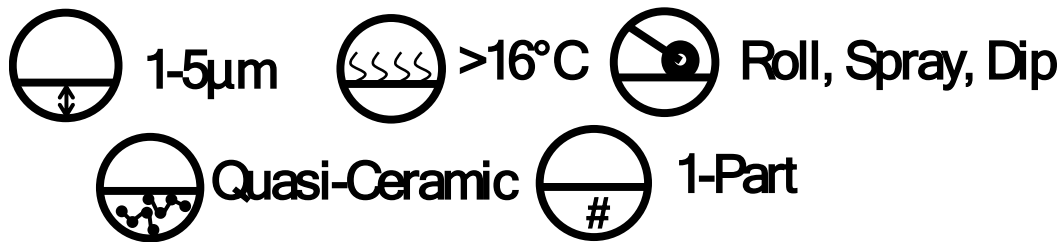


Figure 8. Intake photos of the organic/inorganic quasi-ceramic coating samples FC-23-01-XX provided by FC. Also shown are basic attributes (approximate thickness, cure temperature, application methods, coating type, and number of components).

In total, LUNA proposed two versions of their commercially available Gentoo™ coating (Gentoo™ V1 and Gentoo™ V2) and provided those coatings alone and as a top coating on a commercial-off-the-shelf (COTS) Zn-rich primer. Similar to CLADCO™, Gentoo™ is a hybrid coating consisting of a hard-ceramic hybrid matrix based on a silane-modified polyurethane to produce a coating with high durability and toughness for enhanced abrasion resistance and corrosion protection. Gentoo™ V2, which contained a higher inorganic content, was selected for continued evolution in FY23. LUNA coated ten new coupons in FY23 for LUNA-23-03-XX and are shown in Figure 8. Overall, the samples received in FY23 look very similar to those tested in FY22 and were fully transparent. Importantly, the samples were not

received by SNL in time to do baseline photographs prior to the irradiation experiment, and therefore the color changes in LUNA-23-03-02 to LUNA-23-03-07 are due to radiation and not variability in coating application. Based upon the results of FY22, the LUNA-23-03-XX has the potential to be implemented as **in situ repair** and **ex situ repair** scenarios.

### LUNA-23-03-XX

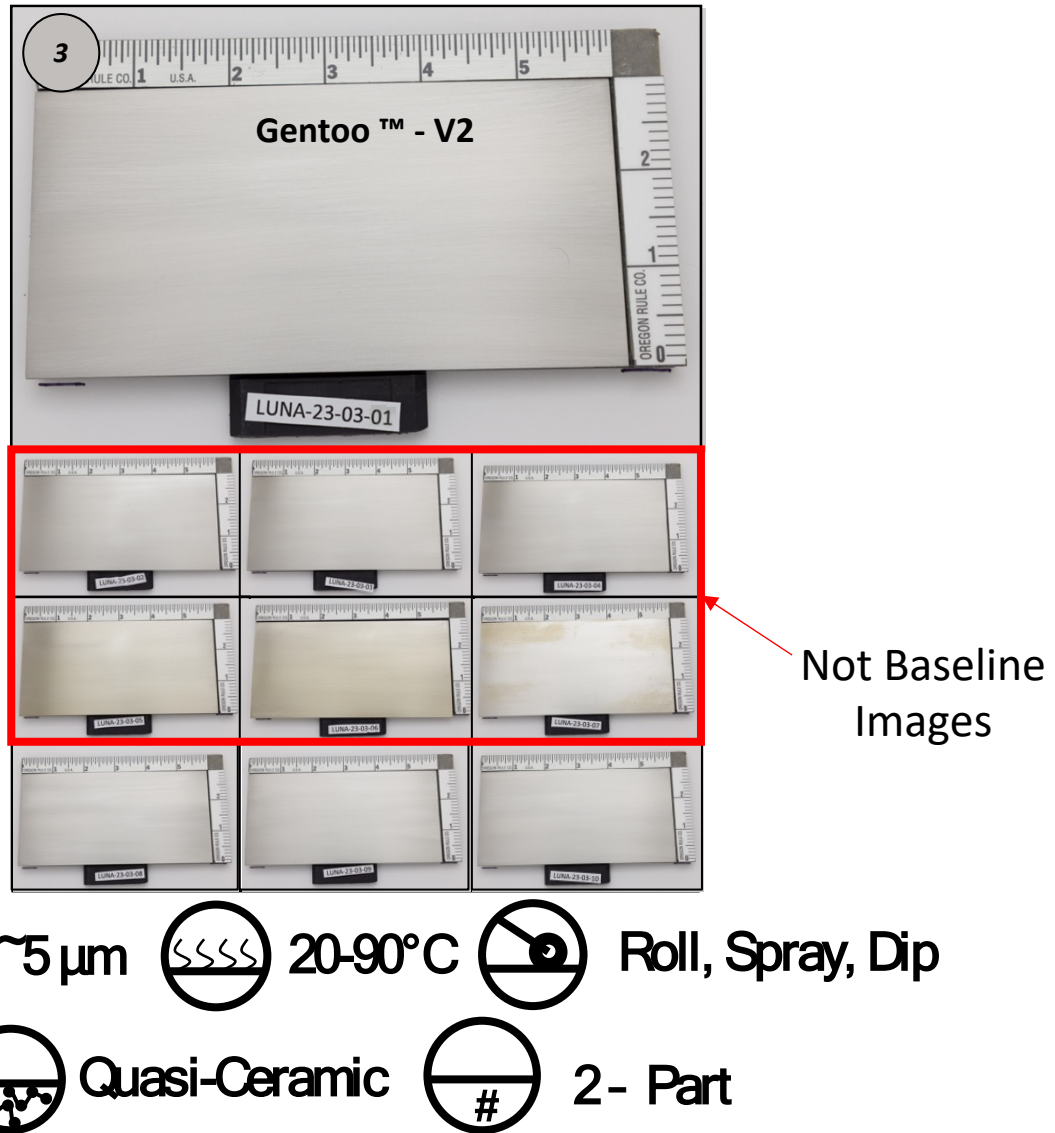
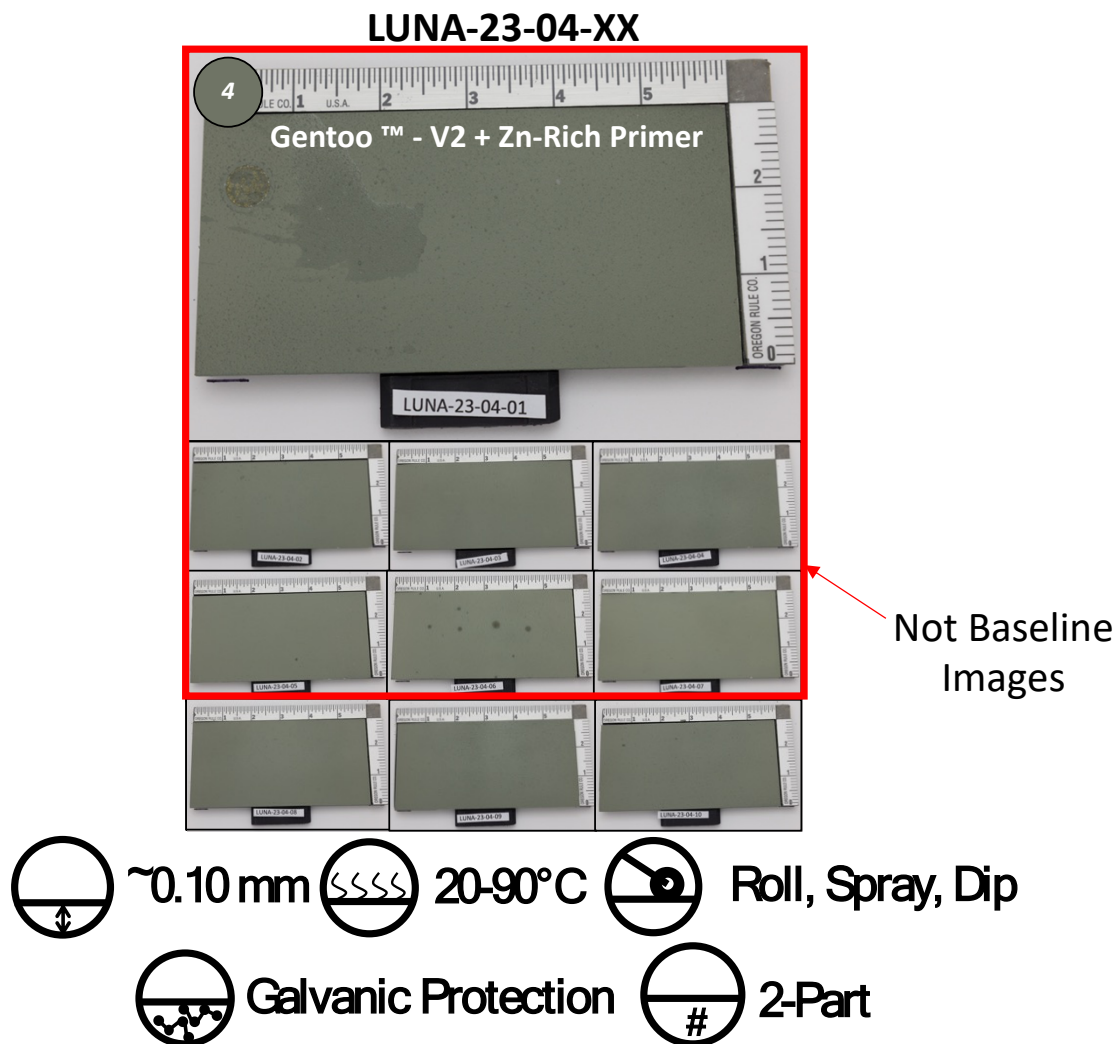


Figure 9. Intake photos of samples of the organic/inorganic hybrid ceramic coating, LUNA-23-03-XX, provided by LUNA. Also shown are basic attributes (approximate thickness, cure temperature, application methods, coating type, and number of components). *\*Note: These samples were not received in time for baseline photos to be taken, therefore some of the images shown have been exposed to radiation.*

### 2.2.3 Zn-Rich Primer Based Coatings for Galvanic Protection

The final class of coatings evaluated for this application are coatings that offer galvanic protection, specifically Zn-rich primers. In this strategy, the Zn present in the primer would passivate the metal surface through galvanic protection, acting as a sacrificial anode. With the use of a Zn-rich primer, specific evaluation for potential occurrence of hydrogen embrittlement must be performed, as it has been demonstrated that Zn-rich primers can lead to cathodic polarization of the substrate (in this case the stainless steel) and thus generate hydrogen [53]. In FY23, SNL evaluated two coating candidates that included a Zn-rich primer provided by LUNA and by TDA. In both cases, the Zn-rich primer used was Sherwin Williams Zn-Clad II, a COTS product. Similar to the Sherwin Williams Macropoxy 646N, Zn-Clad II has been certified to meet the requirements of ANSI/ASME NQA-1 and 10 CFR Part 50 Appendix B for use in nuclear power plants and fuel reprocessing facilities as well as the design requirements for gamma radiation for use in nuclear power plants (ASTM D4082) [46, 47].

LUNA provided a coating that consisted of the combination of Gentoo™ V2 (LUNA-23-03-XX) as a topcoat for the same COTS Zn-rich primer, Sherwin-Williams Zn-Clad II, to add another layer of protection that would aid in the prevention, mitigation, and/or repair of SCC—specifically a focus on crack arrest. This coating was evaluated in FY22, and ten new samples were provided to SNL in FY23 as LUNA-23-04-XX. In this strategy the Zn-rich primer would passivate the metal surface through galvanic protection, and the Gentoo™ V2 on top of the primer will act as a barrier through the addition of a protective, hydrophobic topcoat to slow the Zn-dissolution, thus increasing the protection time for the SS substrate. Therefore, SNL will assess whether the use of a Zn-rich primer provides additional benefit to the viability of Gentoo™ V2 for use on SNF canisters or if the risk of hydrogen embrittlement presents a larger risk than benefit. It is important to note that coatings containing the Zn-rich primer are fundamentally different; therefore, the electrochemical properties are likely to differ from other coating systems, as the Zn is an active metal that is meant to be sacrificial and corrode. The galvanic protection is created by the formation of a galvanic cell. This occurs because Zn is a more active metal than SS, and when damaged or exposed to a corrosive environment, Zn will sacrificially oxidize before the SS. If the SS is exposed, it will act as the cathode in the electrochemical cell and is polarized to more noble potentials. This sacrificial oxidation will form a Zn-oxide protective coating which has been shown to decrease the risk of SCC in Al-Mg alloys [1, 53-55]. Photos of LUNA-23-04-XX are shown in Figure 10. It is important to note that these samples were not received in time for the initial intake photographs; therefore, some of the samples shown have been irradiated. Visually, the LUNA-23-04-XX looks consistent with LUNA-21-04-XX from the FY22 evaluation; however, a few samples appear to have stains or residues present. These proposed solutions from LUNA-23-04-XX have the potential to be implemented as **in situ repair**. **Ex situ** applications would be challenging for this coating due the potential for scratching or delamination [1].



**Figure 10.** Intake photos of samples of the organic/inorganic hybrid ceramic coating on top of a Zn-rich primer, LUNA-23-04-XX, provided by LUNA. Also shown are basic attributes (approximate thickness, cure temperature, application methods, coating type, and number of components).

*\*Note: These samples were not received in time for baseline photos to be taken, therefore some of the images shown have been exposed to radiation and/or a CPP scan.*

TDA provided a coating that consisted of a modified Sherwin Williams Zn-Clad II containing TDA proprietary corrosion inhibitors, identified here as TDA-23-02-XX. This coating differed from the LUNA-23-04-XX coating, as there was no topcoat to protect the Zn coating and that species were mixed into the coating to prevent corrosion of the base metal which may also slow the Zn oxidation. TDA-23-04-XX was applied to the coupon using a compressed air paint gun following surface cleaning with acetone and isopropyl alcohol, in a similar manner to TDA-23-01-XX. The coating was cured at 20-25°C. The intake photos for the TDA-23-02-XX coating can be seen in Figure 11. Overall, the coating was a green/gray color with a rough surface and the sample-to-sample variability was low. In a few cases, the coating looked to have rubbed off during transport, though not down to the metal. Similar to LUNA-23-04-XX, the proposed solution for TDA-23-02-XX is for implementation as an **in situ repair**. **Ex situ**

applications would be challenging for this coating due the potential for scratching or delamination of other Zn-rich primer candidates [1].

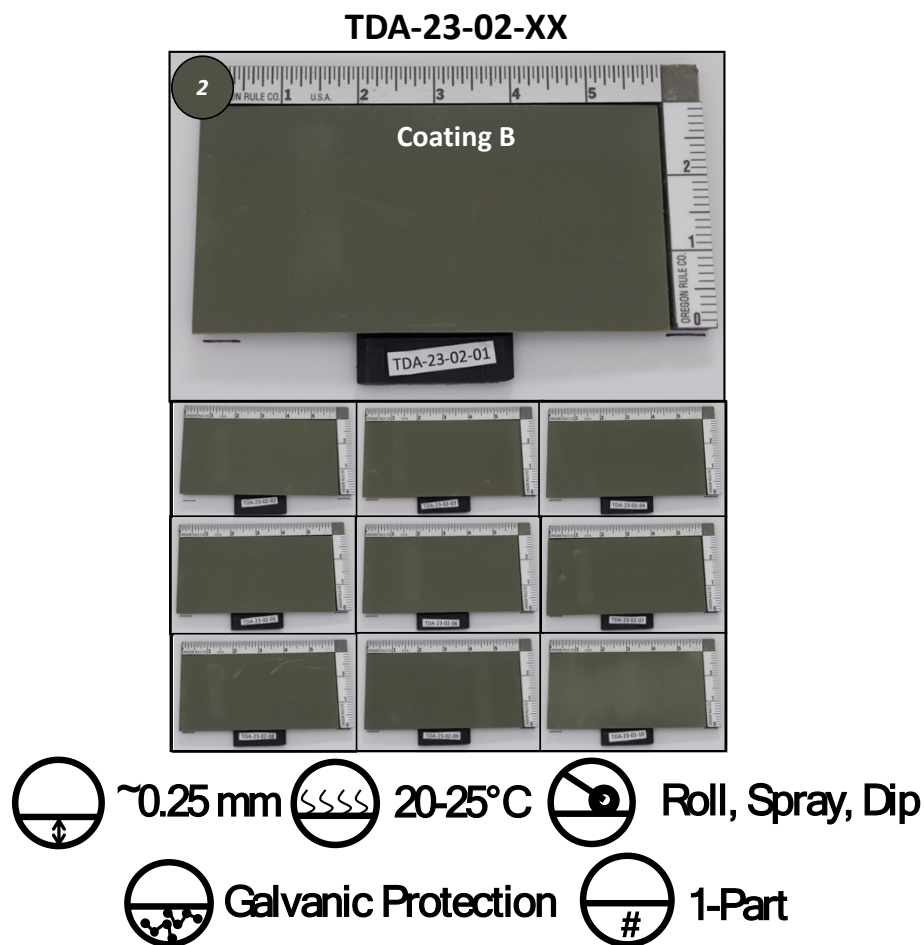


**Figure 11. Intake photos of modified Sherwin-Williams Zn-Clad II with TDA corrosion inhibitor package, TDA-23-02-XX, provided by TDA in FY23. Also shown are basic attributes (approximate thickness, cure temperature, application methods, coating type, and number of components).**

## 2.2.4 Analysis Coupons

In FY23, the coupons were evaluated with respect to thermal and radiation environments relevant to canister conditions. A table of all the evaluated coating candidates is shown in Table 1, including candidates that were not selected for analysis in FY23. To maintain consistency among the samples, efforts were made to expose the same coupon number of each coating to the same environments (i.e., LUNA-23-03-02 and LUNA-23-04-02 were exposed to the same gamma radiation dose). A summary of the exposure conditions and subsequent analyses for each coupon is shown in Table 2. It was not possible to use the same numbering convention for OPM and WHRD samples because they arrived at varying intervals or not at all; therefore, Appendix A summarizes the exposure conditions and analysis for each WHRD and OPM coupon and provides an explanation for deviation in the numbering convention.



**Table 1. Details of the coating candidates. The coupon candidates in bold were downselected and evaluated in FY23.**

Coating Type	Coating Manufacturer	Variant	Trade Name	Details	Comments
Polymeric	Oxford Performance Materials (OPM)	<b>01</b>	<b>OX-PEKK RESIN®</b>	<b>PEKK resin powder coat</b>	-
		02	OX-PEKK SC®	Solution cast Sulfonated PEKK	<i>Not Selected for FY23 Studies</i>
	White Horse Research and Development (WHRD)	01	CRACKSTOP®	Polyurea-polyimide resin	<i>Not Selected for FY23 Studies</i>
		<b>02</b>	<b>GAMMABLOCK®</b>	<b>Polyurea-polyimide resin</b>	-
		<b>03</b>	<b>GAMMABLOCK PLUS®</b>	<b>Phenolic infused polyurea resin</b>	-
	TDA Research (TDA)	<b>01</b>	<b>Coating A</b>	<b>Modified Sherwin-Williams Macropoxy 646N with TDA corrosion inhibitors</b>	<i>Added for FY23 Studies</i>
<b>02</b>		<b>Coating B</b>	<b>Modified Sherwin-Williams Zn-Clad II with TDA corrosion inhibitors</b>	<i>Added for FY23 Studies</i>	
Organic/ Inorganic Hybrid Ceramic or Zn-Rich Primer	Flora Surfaces (FC)	<b>01</b>	<b>CLADCO™</b>	<b>Single-part modified polyurethane macromolecule with quasi-ceramic structure</b>	-
	LUNA Labs (LUNA)	01	GENTOO™ V1	2-part silica-ceramic with polyurethane linker	<i>Not Selected for FY23 Studies</i>
		02	GENTOO™ V1	2-part silica-ceramic with polyurethane linker on Zn-rich primer	<i>Not Selected for FY23 Studies</i>
		<b>03</b>	<b>GENTOO™ V2</b>	<b>2-part silica-ceramic with polyurethane linker</b>	-
		<b>04</b>	<b>GENTOO™ V2</b>	<b>2-part silica-ceramic with polyurethane linker on Zn-rich primer</b>	-
		05	Zn-Clad II	Commercial Zn-rich primer, Sherwin Williams Zn-Clad II	<i>Not Selected for FY23 Studies</i>

**Table 2. Experimental tests performed on each coupon provided by the vendors for FY23 samples.**

Coupon #	Condition	Tests and Evaluation
01	Baseline	Adhesion, Scratch, Hardness, CPP <sup>a</sup>
02	Radiation – 105 Mrad	Adhesion, Scratch, Hardness, CPP <sup>a</sup>
03	Radiation – 211 Mrad	Adhesion, Scratch, Hardness, CPP <sup>a</sup>
04	Radiation – 350 Mrad	Adhesion, Scratch, Hardness, CPP <sup>a</sup>
05	Radiation – 351 Mrad	Adhesion, Scratch, Hardness, CPP <sup>a</sup>
06	Radiation – 724 Mrad	Adhesion, Scratch, Hardness, CPP <sup>a</sup>
07	Radiation – 1305 Mrad	Adhesion, Scratch, Hardness, CPP <sup>a</sup>
08	Thermal (Long Term)	Adhesion, Scratch
09	TBD	-
10	Thermal Degradation	Thermal Gravimetric Analysis

<sup>a</sup> Cyclic potentiodynamic polarization (CPP) scans were only performed on FC-23-01-XX, LUNA-23-03-XX, LUNA-23-04-XX, and TDA-23-02-XX. CPP scans were not performed on WHRD-21-02-XX, WHRD-21-03-XX, OPM-23-01-XX, or TDA-23-01-XX because they were either too thick or too capacitive.

## 2.3 Down-Selection

One goal in the initial coupon evaluation in Phase 1 was to down-select the coating candidates to focus resources on coatings that have the highest likelihood of success. In the FY22 report, coatings were evaluated based on mechanical properties (adhesion and scratch testing), electrochemical properties (electrochemical impedance spectroscopy (EIS)), and atmospheric exposures [1]. The down-selection process was not completed prior to the completion of the FY22 EOY report based on the need to further evaluate the EIS data; therefore, the down-selection data is presented in this report.

### 2.3.1 Continued Evaluation of EIS Data from FY22

EIS was performed in FY22 and the preliminary results for the baseline performance (no atmospheric exposure) and the impact of a 30-day atmospheric exposure were shared previously [1]. Prior to the release of the FY22 report, the samples exposed to 90 days in a corrosive atmospheric exposure environment were not complete. For these tests, ~300 µg/cm<sup>2</sup> of artificial seawater (ASW) was deposited on ¾ of the coating surface, then the coating was aged in an environmental chamber at 76% RH (just above the deliquesce RH of NaCl) and 40 °C. Under these atmospheric conditions, it is expected that a NaCl-rich brine would persist on the surface during the extent of the experiment. A set of coated coupons were removed from the chamber after 30 days and 90 days. These coupons were then analyzed in the same manner as the baseline samples to compare and evaluate the impact of the atmospheric exposure.

For the EIS analysis in FY22, the same equivalent circuit was used to evaluate all of coupons (Figure 12); however, it was also noted that further refinement to gain a more accurate understanding of the coating’s performance was needed. In FY23, the EIS data was re-evaluated to better understand the data quality and the impact of different equivalent circuit elements to better inform conclusions made from the EIS data.

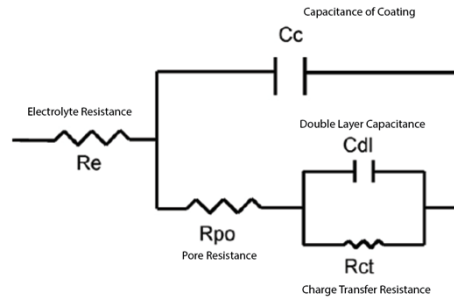


**Figure 12. Equivalent circuit used to fit all EIS data as an initial estimate in FY22. This equivalent circuit is commonly used to represent organic coatings on metallic substrates [56, 57]. The different electrical components are used as analogues to physical or electrochemical behavior of the coating system.**

Another circuit that may be of interest replaces the capacitors seen in Figure 12 with constant phase elements (CPEs), which may be more representative of non-ideal reactive processes in the electrochemical system. A CPE allows for an arbitrary mix of capacitive, resistive, and inductive behavior by introducing a dimensionless term  $-1 \leq n \leq 1$  such that the CPE's impedance is given by:

$$Z_{CPE} = \frac{1}{Q_0(j\omega)^n} \quad \text{Eq. 1}$$

where  $j = \sqrt{-1}$ ,  $\omega$  is the angular frequency of our input voltage signal and  $Q_0 = \frac{1}{|Z|}$  at  $\omega = 1 \text{ rad/s}$ , with  $|Z|$  given by an inductance, resistance, or capacitance depending on the value of  $n$ . Over the range  $n \in [-1,0)$ , the CPE will behave inductively, at  $n = 0$  it will behave as a pure resistor and over  $n \in (0,1]$ , it will behave capacitively. Studies have shown that treating the coating capacitance  $C_c$  as an ideal capacitor in the equivalent circuit can lead to conclusions of excessive water uptake beyond coating saturation [56]. Furthermore, it is well known that double layer capacitance ( $C_{dl}$  in Figure 12) does not behave as an ideal capacitor [58]. Thus, it may be appropriate to replace these elements with constant phase elements.

Upon analysis of the EIS data from FY22, it was noted that the current response was often nonlinear with the input perturbation voltage for lower AC frequencies. We observed current responses at harmonics of the fundamental input frequency and employed total harmonic distortion (THD) as a metric to quantify the extent of these nonlinearities, defined as:

$$THD = \frac{1}{|Y_f|} \sqrt{\sum_{k=2}^N |Y_k|^2} \quad \text{Eq. 2}$$

where  $|Y_f|$  is the amplitude of the current response signal at the fundamental frequency and each  $|Y_k|$  is the amplitude of the current response signal at the  $k^{th}$  harmonic of the input frequency. THD, then represents the amount of the signal contained in the harmonics normalized by the amount of signal in the fundamental.

Figure 13 shows mean THDs calculated for each coating as a function of input AC frequency. A THD threshold of 5% was chosen to classify the impedance measurements at a given frequency as nonlinear in accordance with Biologic [59]. Coatings without a Zn-rich primer experienced rapid increases in THD below about 100 Hz, with the spike centered around 11.837 Hz. The polymeric coatings generally remained highly nonlinear for frequencies below this spike. Of all the non-polymeric coatings, only

LUNA-21-03 was able to remain below the 5% threshold over all frequencies. The observed THD differences between coatings are likely due to varying electrochemical kinetics as well as variance in electrical insulation, which is largely influenced by coating thickness.

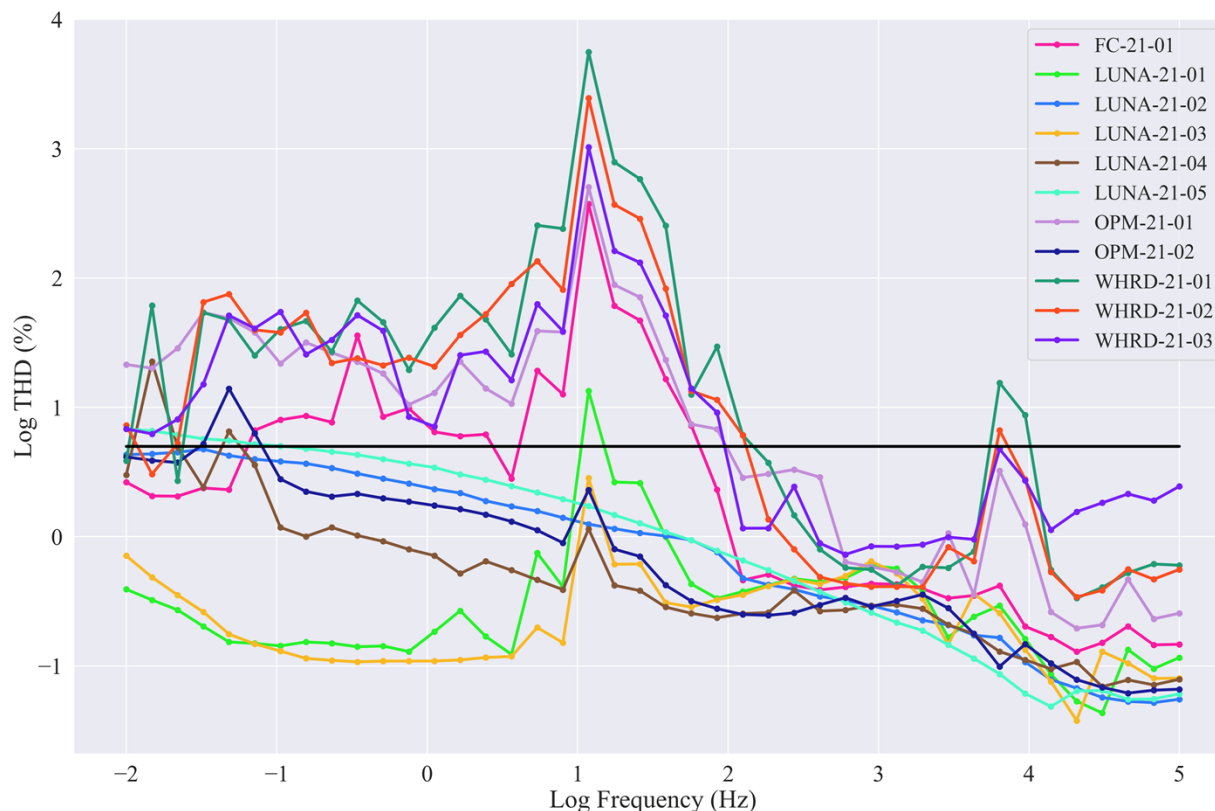


**Figure 13. Logarithm of mean total harmonic distortion (%) of the current response signal observed for baseline coatings as a function of the logarithm of the AC perturbation voltage frequency (Hz). The black horizontal line represents a 5% threshold for nonlinearity. The trends presented for baseline coatings persisted for 30-day and 90-day exposed coatings.**

To validate the quality of the input, we performed the same THD analysis for the input perturbation voltage signal (Figure 14). We observed large spikes in input THD for the polymeric coatings at 11.837 Hz, except for OPM-21-01 whose peak input THD was shifted slightly to 7.988 Hz. It was noted that during EIS, OPM-21-02 was cracked and therefore its electrical behavior diverged from the other polymeric coatings and exhibited characteristics similar to bare SS-304. It is unclear why input THD differs between coatings and as a function of frequency. However, there may be a few possible contributions to this behavior: potentiostat circuitry introducing distortion at particular frequencies, ambient electromagnetic fields introducing extraneous signal into the circuit, non-stationarity of the open circuit potential, or reactive processes in the coatings introducing kick-back into the input lines. Further study of this phenomenon is required to understand the cause of this behavior. In this effort, open circuit potential drift correction and employment of a faraday cage may help diagnose the source of these dependencies.

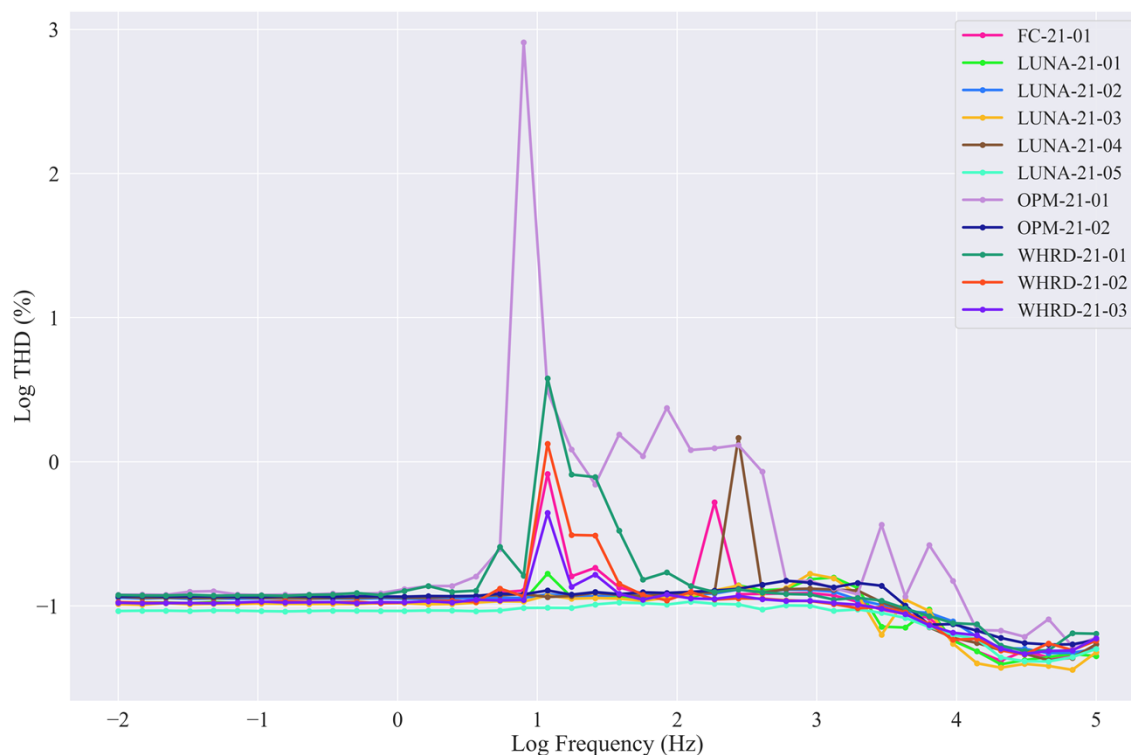


**Figure 14. Logarithm of mean total harmonic distortion (%) of the perturbation voltage input signal observed for baseline coatings as a function of the logarithm of AC perturbation voltage frequency (Hz). The trends presented for baseline coatings persisted for 30-day and 90-day exposed coatings.**

In the absence of a linear response, the notion of impedance is ill-defined due to the definition of impedance requiring a perfectly linear response signal. If most of the response signal is contained in harmonics, the calculated impedance will be much higher than if those harmonics are included. Furthermore, the nonlinear least squares algorithms used to regress the EIS data onto an equivalent circuit are extremely sensitive to data quality and small input deviations. However, electrochemical systems are inherently nonlinear due to the exponential relationship between electrode overpotential and current response [58]. Thus, careful treatment of EIS data must be given to ensure the validity of our calculations and subsequent conclusions. To curtail distortion, in FY22 we began to develop a method to determine the optimal perturbation voltage informed by the previously collected polarization scans and we began development of a mathematical method to handle any nonlinearities that are insurmountable through the control of perturbation voltage alone. However, these studies are ongoing, and conclusions are not yet available. Once developed, these methods will be applied to the EIS of baseline, 30-day, 90-day, and radiation-exposed coatings.

Beyond distortion, the resistivity of the thicker polymeric coatings makes obtaining valid impedance measurements difficult, as their impedances are near the limits of the potentiostat measurement bounds of about  $1 \times 10^{12} \Omega$ . Thus, even if distortion is treated appropriately, we may not be able to obtain EIS measurements for some coatings due to their inability to develop ionic pathways to the SS-304 substrate. This behavior, though experimentally problematic, is indicative of high corrosion resistance. Coatings with this desirable property may be difficult to quantitatively compare using typical EIS methods. The coatings approaching or exceeding the capabilities of the potentiostat are: OPM-21-01, WHRD-21-01, WHRD-21-02, and WHRD-21-03.

### 2.3.2 Justification for Down-Selection

To focus rigorous performance testing on the most promising coating candidates, a down-selection process was performed based upon the FY22 performance testing. This down-selection process was qualitative, but in many cases, there were clear reasons to not continue evaluating a particular coating. The coatings that were not selected for further evaluation in FY23 were OPM-21-02-XX, LUNA-21-01-XX, LUNA-21-02-XX, LUNA-21-05-XX, and WHRD-21-01-XX. The results of the qualitative assessment are shown in Figure 17.

The ability to adhere to the SS surface and the results of the atmospheric exposure test caused OPM-21-02-XX to be removed from consideration. Specifically, when the coating cured it left mud cracks on the surface that were detected by surface roughness analyses [1]. Those mud cracks, when exposed to a corrosive brine, allowed for the brine to infiltrate the surface, and corrode the underlying metal (Figure 15).

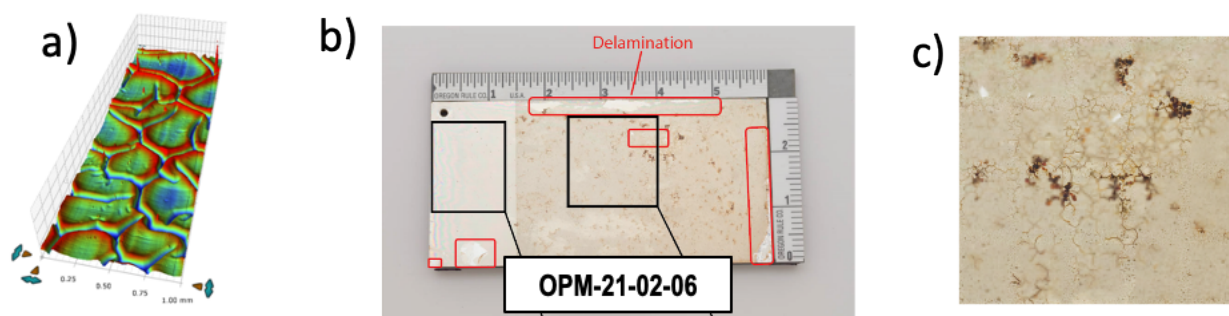


**Figure 15. a) mudcracks that formed during the curing process of OPM-21-02-XX measured by profilometry, b) visual inspection of OPM-21-02-06 after 30 days at 76%RH/40°C with 300 µg/cm<sup>2</sup> ASW showing corrosion damage and delamination, and c) a close up of the corrosion damage following atmospheric exposure.**

LUNA-21-01-XX and LUNA-21-02-XX were not selected to move forward in FY23 because the performance of LUNA-21-03-XX and LUNA-21-04-XX were superior. LUNA-21-01-XX and LUNA-21-03-XX differ by using different version of the Gentoo product, Gentoo V1 and Gentoo V2 specifically. Gentoo V2 had more ceramic-like behavior than Gentoo V1, and its adhesion performance was better. In addition, Gentoo V2 was more different from the FC-21-01-XX than the Gentoo V1—all of which contain silica ceramic components and polyurethane linker. LUNA-21-04-XX contained Gentoo V2 as a topcoat and LUNA-21-02-XX contained Gentoo V1 as a topcoat for a Zn-rich primer. The performance of LUNA-21-04-XX was better than LUNA-02-XX, especially when exposed to atmospheric corrosion environments.

LUNA-21-05-XX, or Zn-Clad II alone, was not selected to continue in FY23 because of its mechanical properties—adhesion tests resulted in adhesive failure to the metal substrate and scratch tests resulted in delamination of both the scratched area and between scratches. Overall, the Zn-Clad II alone is too prone to physical degradation without a topcoat or modification.

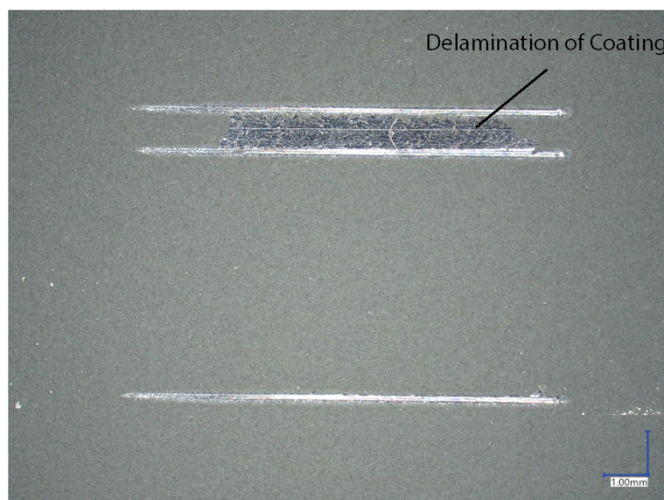
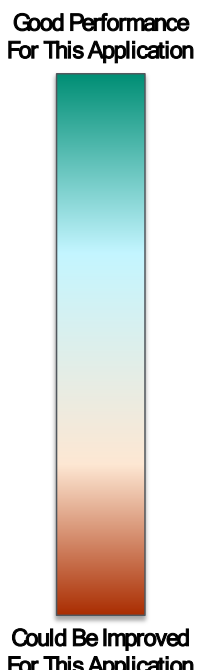


**Figure 16. Optical image of LUNA-21-05-02 (Zn-rich primer only) after scratch testing at 25N force. Adhesive failure occurred at <2N, and a subsequent scratch at a separation distance of 1 mm caused delamination of the coating between the scratches. A scratch performed using a separation distance of 5 mm did not cause delamination between scratches [1].**

Lastly, WHRD-21-01-XX was not continued for evaluation in FY23 because all three WHRD samples performed similarly. For this application the subtle differences between the coatings did not play an important role; therefore, only WHRD-21-02-XX and WHRD-21-03-XX were included in FY23.

Beyond the down-selection, recommendations for improvements were provided to the vendors for coating in FY23 based upon the results of the FY22 performance testing. Specifically, for FC-21-01-XX, it was recommended to improve the surface preparation to allow for better adhesion. For WHRD-21-02-XX and WHRD-21-03-XX, it was requested to coat the coupons with a smooth version of the coating. This would prevent salt and brine from puddling in the large surface features; however, these samples were not received. In addition to these changes, the coatings from TDA were included in the FY23 tests. To date, none of the FY22 tests have been performed on the TDA samples but may be pursued in the future to complete the coatings analysis.

Future work in the down-selection process involves developing a quantitative multifactor analysis to weight the performance results for various applications.



Coating		Baseline Performance		Change as a result of Atmospheric Exposure		Thermal Exposure	Radiation Exposure	Electrochemical Performance (EIS, CPP)
		Adhesion	Scratch	Adhesion	Scratch			
Ceramic/Hybrid Coating	<b>FC-21-01</b>					FY23	FY23	FY23/FY24
	LUNA-21-01							
	LUNA-21-02							
	<b>LUNA-21-03</b>							
	<b>LUNA-21-04</b>							
Zn-Rich Primer	LUNA-21-05							
	<b>TDA-23-02</b>			<i>Not Tested Yet</i>				
Polymeric Coating	<b>TDA-23-01</b>			<i>Not Tested Yet</i>				
	<b>OPM-21-01</b>							
	OPM-21-02							
	<b>WHRD-21-01</b>							
	<b>WHRD-21-02</b>							
	<b>WHRD-21-03</b>							

BOLD coatings have been selected (with modifications) for more rigorous testing.

Figure 17. Table showing a qualitative rationale for the initial down-selection where green shows that the coating performance was “Good for this Application” and red means the observed coating performance “Could be Improved for this Application” with respect to a given test. The coating candidates in bold were selected to be evaluated in FY23.



### 3. THERMAL EVALUATION

Considering the canister thermal environment is a critical factor to determine effective coating performance and timing of the coating application. Canister thermal models have been developed at Pacific Northwest National Laboratory (PNNL) for both horizontal and vertical dry storage systems. These results were implemented in the SNL probabilistic SCC model [60, 61]. Assuming a 24 kW initial heat load and 15.6°C ambient temperature, results from the thermal modeling suggest that initial surface temperatures can exceed 225 °C in some locations for several years [10]. Even after 20 years or more of storage, canister surface temperatures can still exceed 150 °C (Figure 18); therefore, thermal properties of the coatings need to be well understood and any thermal degradation that occurs will be a determining factor to the timing and placement of a possible coating technology.

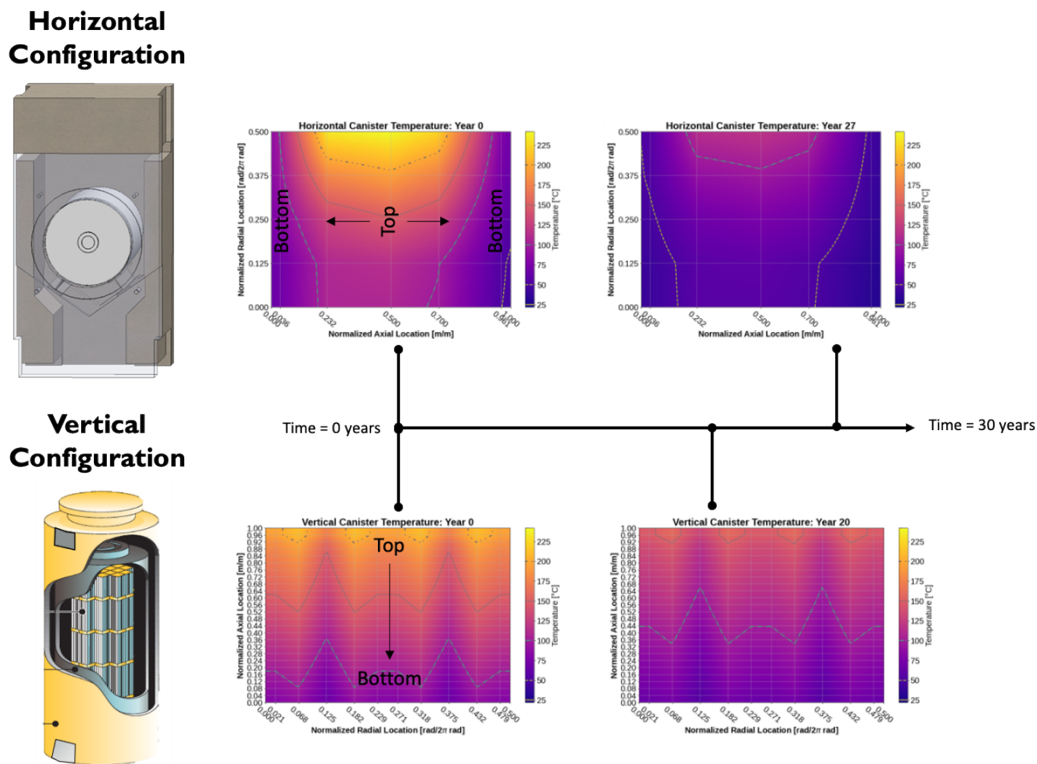


Figure 18. Schematic modified from Gilkey, Brooks [10] showing the canister surface temperatures from horizontal and vertical canisters from 0 year to 30 years.

In FY23, thermal tests were performed to evaluate the coatings’ thermal degradation temperature and glass transition temperature using thermogravimetric analysis (TGA). Temporal tests of coating properties at elevated temperatures were also performed to evaluate the impact of long-term thermal exposures on physical and mechanical properties.

#### 3.1 Thermogravimetric Analysis

TGA was used to determine the onset temperature of thermal degradation and differential scanning calorimetry (DSC) was used in tandem to evaluate thermodynamic processes that occur as the temperature is ramped up [62, 63]. For these measurements weight of sample is continuously monitored while being heated in a purged, highly insulated furnace. A high temperature, high sensitivity balance is used to suspend two vented alumina crucibles—one empty as a reference, and one containing a small amount of the sample—in the middle of the furnace. A small thermocouple is embedded within the

support beams of the balance to provide temperature measurements of the sample and the reference crucible.

TGA was performed to determine the thermal behavior and performance of the candidate coatings. Thermogravimetric data is usually expressed as a percent weight change (relative to the original sample weight at room temperature) measured as the sample temperature is varied. During heating, the thermal power required to raise the sample temperature by a known amount is also measured and expressed as heat flow in Watts (W). Measurements were performed on 2-40 milligrams of the candidate coating which was mechanically removed (cut, scraped, or ground off) from the SS substrate. The samples were heated in compressed air with a constant flow rate of 100 mL/min and the temperature ramped from room temperature to 800°C (to determine onset of degradation, not to simulate any known canister condition) with a ramp rate of 1°C/min. Figure 19 shows the thermogravimetric data for all candidate coatings from ~25 °C to 800°C. From this plot all the purely organic coatings, except for TDA-23-01-10, had nearly complete weight loss by the end of the experiment, whereas the coatings that had inorganic components, such as silica or Zn, maintained some mass at the end of the experiment. The coatings with Zn-rich primers (LUNA-23-04-10 and TDA-23-02-10) had mass gain at elevated temperatures (>500°C), which was likely caused by Zn thermal oxidation.

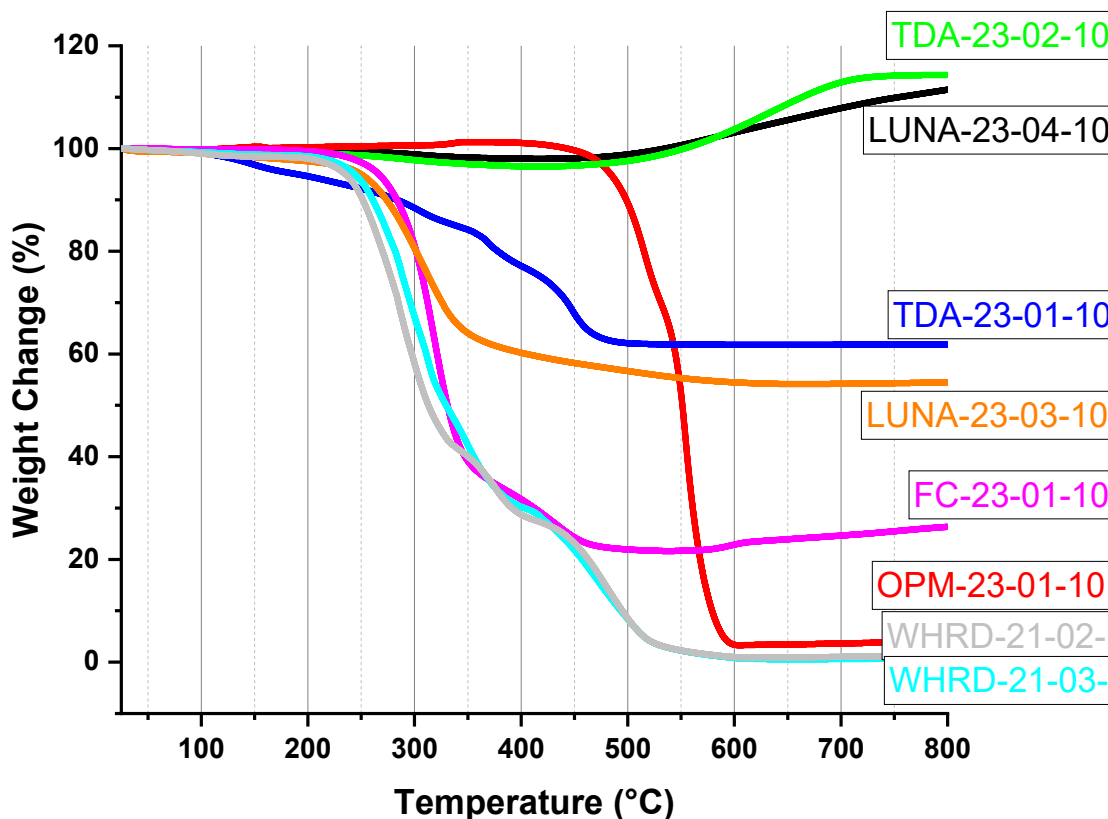
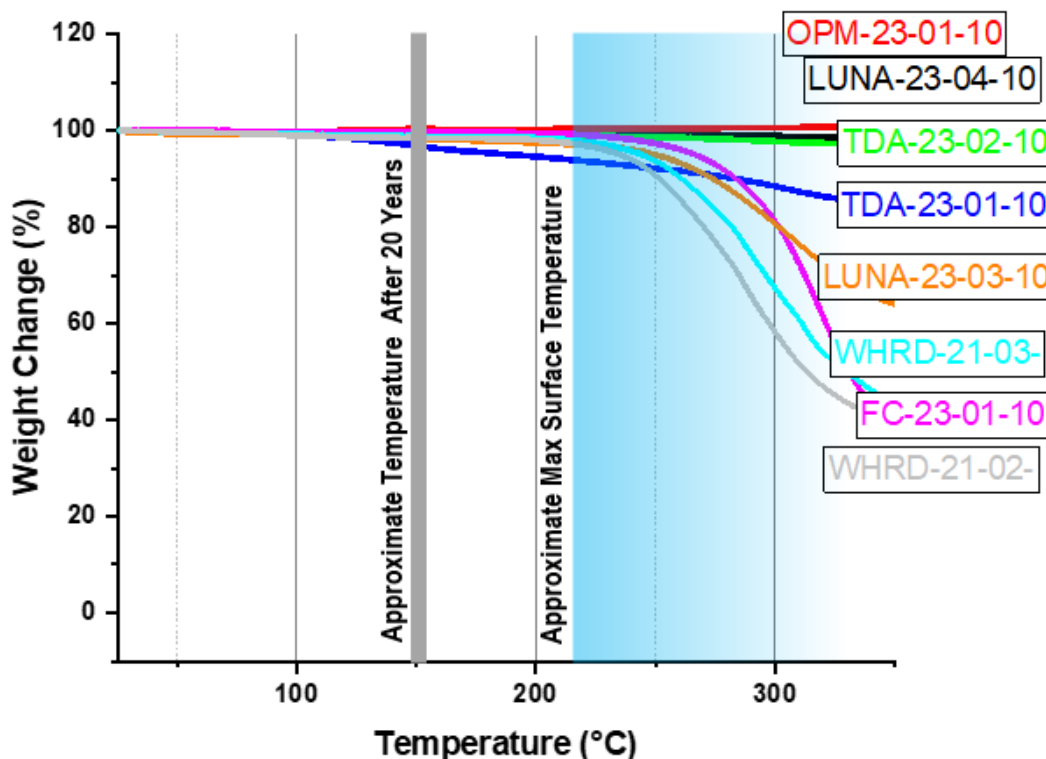


Figure 19. TGA data for all coatings expressed as % weight change. Coatings were tested to temperatures >225°C to determine onset of thermal breakdown.

Importantly, much of the thermal degradation of the coatings occurs at temperatures well beyond the maximum predicted canister surface temperatures. Therefore, Figure 20 focuses in on a canister relevant

temperature range of the TGA data, where the plot shows the approximate maximum temperature of a new canister and the maximum temperature after 20 years of storage. Most coatings, with exception of TDA-23-01-10, did not experience significant mass loss until greater than 200°C. The hybrid ceramic coatings (LUNA-23-03 and FC-23-01) were expected to have high thermal stability, but due to the presence of the polyurethane linker in the coatings mass loss began at approximately 225°C. The OPM-23-01-10 coating showed the highest thermal resistance of the polymeric coatings with no measurable mass loss up to 450°C. The coatings containing Zn- rich primers (TDA-23-02 and LUNA-23-04) had little-to-no degradation under canister relevant temperatures and showed an increase in mass starting at 400°C, which may be due to rapid oxidation of Zn around that temperature [64].

Based on these observations, it appears that most coatings could survive application (from a thermal perspective) on canisters after 20 years of storage, as the maximum canister surface would be cool enough to avoid coating degradation. Further investigation is needed for TDA-23-01-10 to understand what is being lost at 100 °C. Fewer coatings, only OPM-23-01-10 and possibly TDA-23-02-10 and LUNA-23-04-10, would be appropriate to apply on new or freshly loaded canisters, which are estimated to exhibit surface temperatures greater than or equal to 225°C [10]. More investigation is needed to understand the impact of the small mass loss observed from LUNA-23-04-10 and TDA-23-02-10.



**Figure 20. TGA data on all coatings expressed as % weight change. Temperatures above 225°C were tested to determine onset of material breakdown and do not correspond to any known application condition for SNF canisters. Canister surface temperatures (shown as vertical lines) were estimated from thermal models Gilkey, Brooks [10].**

Figure 21 illustrates the mass change for each coating as a function of important temperatures discussed in this report. At 80°C, which represents the temperatures coatings were exposed to in the radiation studies (discussed later in section 4.1), minimal mass loss (<1%) was observed. At 150°C, representing a canister having cooled for 20 years, mass loss increased to <1% for most purely polymeric coatings, with exception of OPM-23-01-10. At 200°C, representing a canister between new and 20 years of cooling, mass loss for most coatings exceeded 1%, with a few purely polymeric coatings approaching 2%. By 225°C, representing a freshly loaded canister as previously described, the purely polymeric coatings (with exception of OPM-23-01-10) exceeded 2% mass loss and LUNA-23-03-10, a hybrid ceramic coating, exceeded 3%. The Zn-rich primer containing coatings seem relatively unaffected by temperature with mass losses less than 0.5% for LUNA-23-04-10 and just over 1% for TDA-23-02-10. Comparing LUNA-23-04-10 to TDA-23-02-10 is difficult since the composition and concentration of corrosion inhibitors present in TDA-23-02-10 is unknown. A larger mass loss is shown in LUNA-23-03-10 than in LUNA-23-04-10 (which also contains LUNA-23-03-10) because the Zn-rich primer contributes mass to the sample, lowering the mass fraction that LUNA-23-03-10 contributes to the sample. It is expected that the LUNA-23-03-10 present in the LUNA-23-04-10 will behave thermally the same as pure LUNA-23-03-10 but since it constitutes a lower mass fraction in the sample the total indicated weight change will be less as is observed.

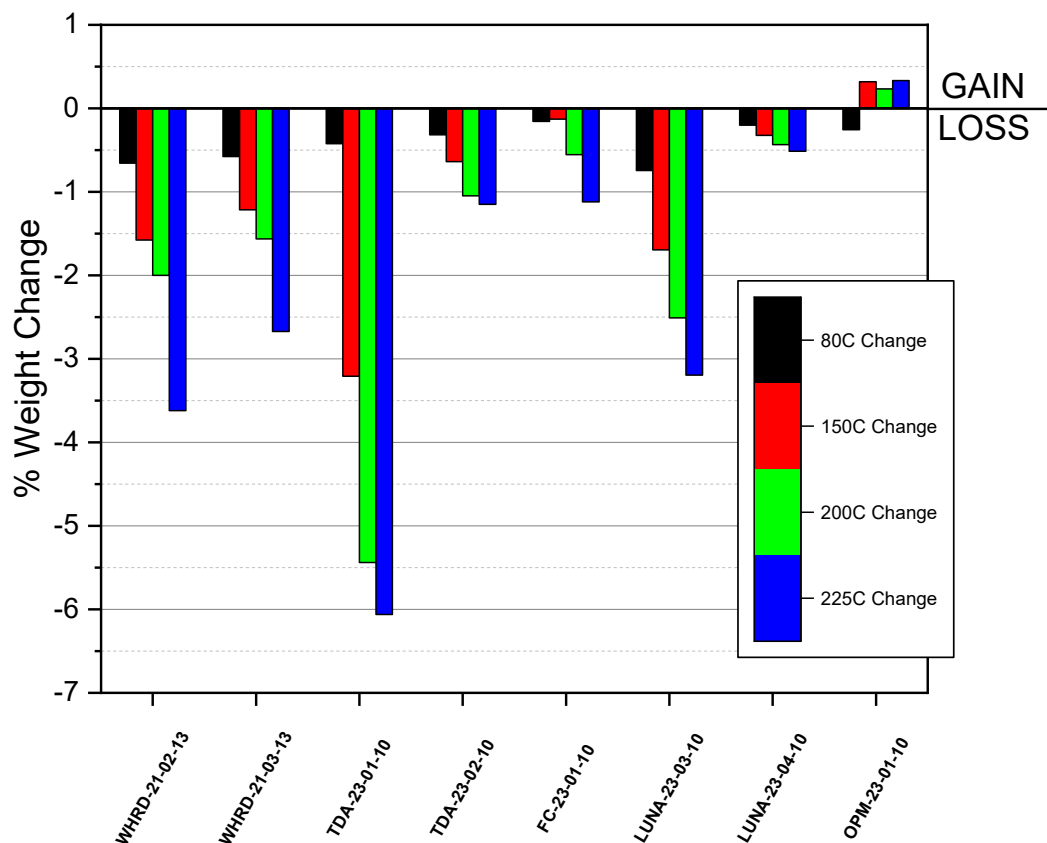
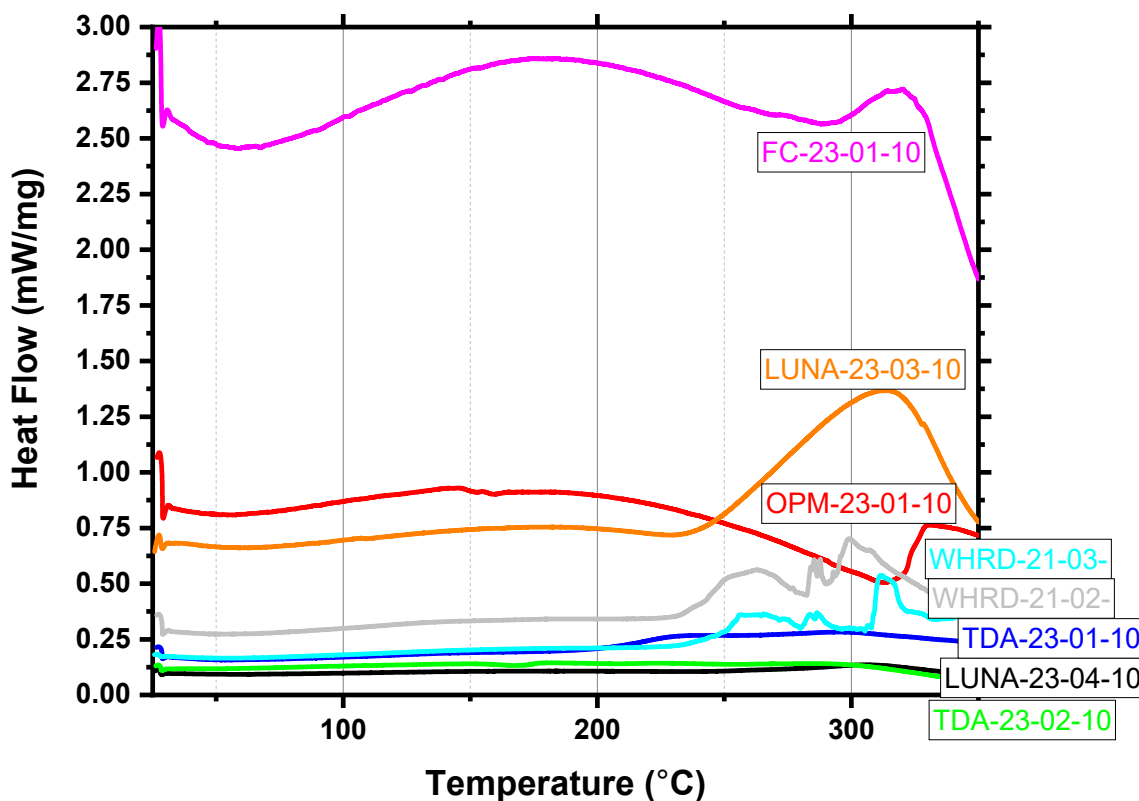


Figure 21. Weight change at 80°C, 150°C, 200°C and 225°C for all coatings.

Figure 22 shows the mass-normalized heat flow as a function of temperature for all coating samples. FC-23-01-10 had the highest weight normalized heat flow (2.5 mW/mg) of all samples; however, it also had the smallest sample mass (2.48 mg). LUNA-23-03-10 and OPM-23-01-10 had very similar heat flow for the duration of the test ranging between 0.75-1 mW/mg. The remaining samples had very similar heat flow values of less than 0.5 mW/mg up to 225°C. Up to 225°C, dramatic phase changes (endothermic valleys) or onset of melting (exothermic peaks) were not observed for any coating, indicating that the measured coating mass loss (shown in Figure 19) is likely due to the evolution of gas-phase organic species or evolution of water from the coating. At temperatures exceeding 225°C large exothermic peaks, representing melting, and endothermic features, representing phase changes, were observed in the data. These high temperature thermal events are unlikely to occur in the interim storage environment but may occur in some locations on hot, freshly-loaded canisters, which is a critical consideration when using a given coating as a prevention method.



**Figure 22. Mass-normalized heat flow (W/g) data collected during Thermogravimetric experiments. Samples were tested past 225°C to determine onset of phase changes or other thermodynamic events.**

Overall, the thermal performance of all candidate coatings was satisfactory. Most coatings did not experience mass loss in conditions simulating the lower temperatures that might be found on the surfaces of aged, cooled canisters (<150°C) while some did not experience mass loss until much higher temperatures exceeding the maximum estimated temperature on new canisters (225°C). Since the mass loss experienced at lower temperatures (<225°C) could not be attributed to phase changes or melting, it is

hypothesized that organic species or water were outgassed from the sample. This highlights the importance of further characterization of the outgassed species to determine whether they pose any additional hazards to the interim storage system.

Comparison of these thermal results to canister conditions is difficult since the TGA measurement incorporates highly dynamic thermal conditions rather than long term isothermal (or quasi-static) holds that would occur on a canister environment. It is unknown whether long term isothermal holds at canister relevant temperatures would result in significant outgassing. Specifically, from a dynamic thermal perspective, only OPM-23-01-10, LUNA-23-04-10, and TDA-23-02-10 could be considered for use on a new canister. For the remaining coatings, it would be necessary to allow for the canister to cool considerably before coating application to ensure the surface temperature would be low enough to prevent thermal degradation.

### **3.2 Outgassing Analysis**

A Hiden Analytic quadrupole residual gas analyzer was used to analyze which gaseous species evolved during TGA measurements for LUNA-23-04-10, WHRD-23-03-13, and TDA-23-01-10. Samples were heated in air at 1 °C/min in the TGA mentioned in the previous section. The exhaust of the TGA was sampled using a heated microfluidic tube resulting in a max RGA chamber pressure of  $4 \times 10^{-6}$  Torr. The partial pressures of species with atomic weights up to 200 atomic mass units (AMUs) were measured as a function of time, which was cross correlated with temperature of the sample in the TGA.

Figure 23 shows the percent concentration of six atomic weights as a function of sample temperature in the TGA. Table 3 shows the measured atomic weights and their corresponding most probable species detected. For example, 17 AMUs corresponds to ammonia in RGA. Interestingly, the two species with any observable change between 50°C and 500°C were atomic weights 18 and 44, corresponding to water and nitrous oxide/carbon dioxide respectively. TDA-23-01-10 began outgassing water around 250°C and nitrous oxide/carbon dioxide around 300°C. WHRD-23-03-13 began outgassing water at 225°C and nitrous oxide/carbon dioxide around 250°C. LUNA-23-04-10 does not appear to have outgassed water but does appear to evolve small amounts of carbon dioxide around 250°C. This is consistent with the hygroscopic behavior of purely polymeric materials. A small increase in ammonia (17 AMU) can be observed at 300°C for WHRD-23-03-13 and TDA-23-01-10. This temperature is higher than the maximum expected canister surface temperature, but it is important to understand what species are evolving from a coating. Even at 1°C/min these thermal exposures are still considered highly dynamic compared to the canister surface environment, thus it might be possible that given enough time ammonia could evolve from WHRD-23-03-13 at lower temperatures, albeit at small concentrations. The presence of high concentrations of oxygen and nitrogen are expected since the measurements were performed in compressed air. Atomic weight 43 was included to verify these compounds (acetone, methyl ethyl ketone, butane, etc) were not outgassed.

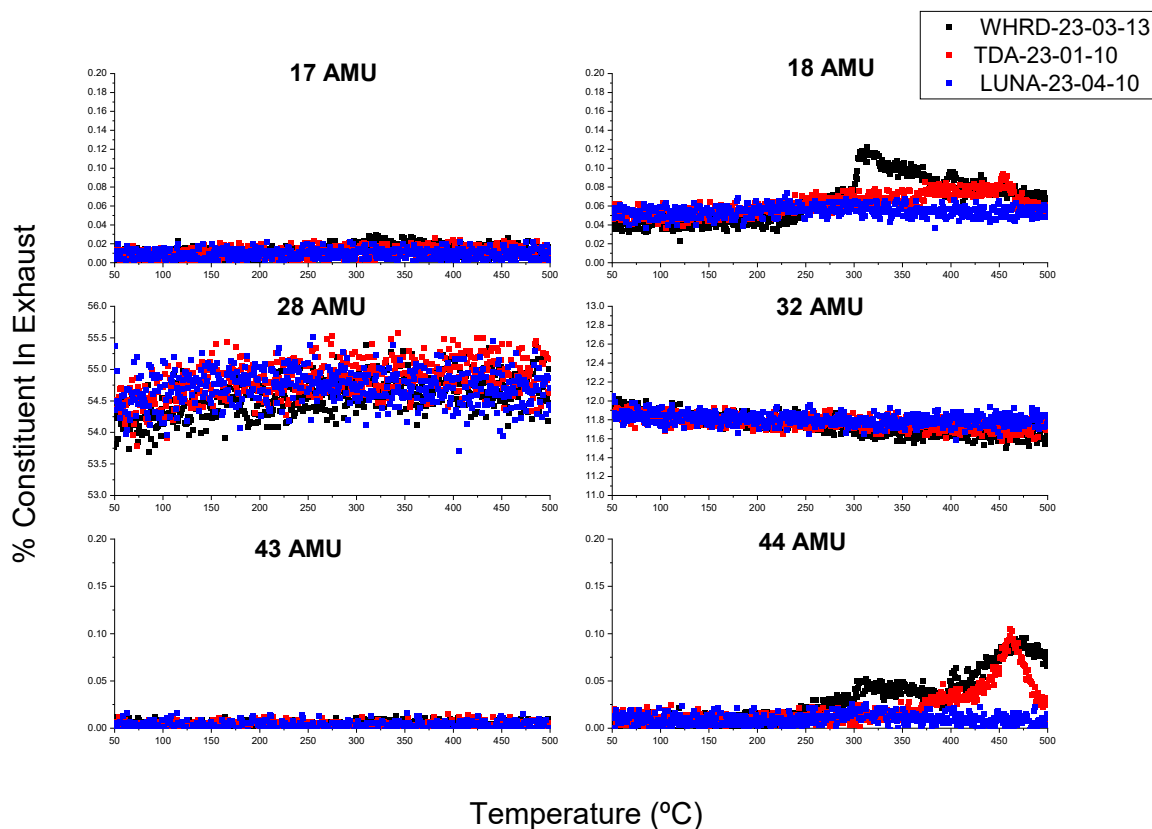


Figure 23. Residual Gas Analysis of exhaust stream during heating in TGA of various species with different atomic weights (in AMU).

Table 3. Residual Gas Analysis spectra atomic weights and probable corresponding species [65].

Atomic Mass Unit (AMU)	Most Probable Species Detected
17	Ammonia
18	Water
28	Carbon Monoxide, Nitrogen, Ethylene, Ethane
32	Oxygen
43	Butane, Acetone, Methyl Ethyl Ketone, Acetic Acid, MP Oil, Turbopump Oil
44	Nitrous Oxide, Carbon Dioxide

The percent mass as a function of temperature is plotted together with the RGA data in Figure 24 to illustrate that the outgassing of water and carbon dioxide out of the coating are responsible for the majority of the weight loss measured in TGA. For WHRD-23-03-13 and TDA-23-01-10, a small amount of NH<sub>3</sub> is present as mass loss begins to accelerate. Further, the lack of change in mass in the same temperature range exhibited by LUNA-23-03-10 seems to correlate to no observable evolution of these species.

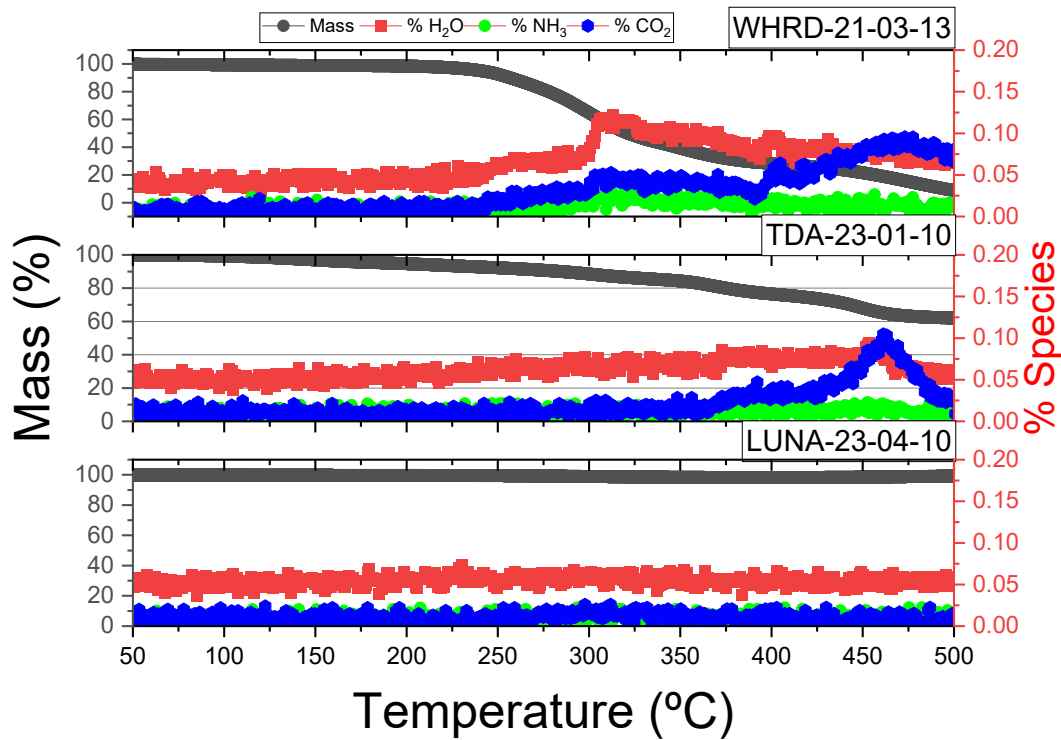
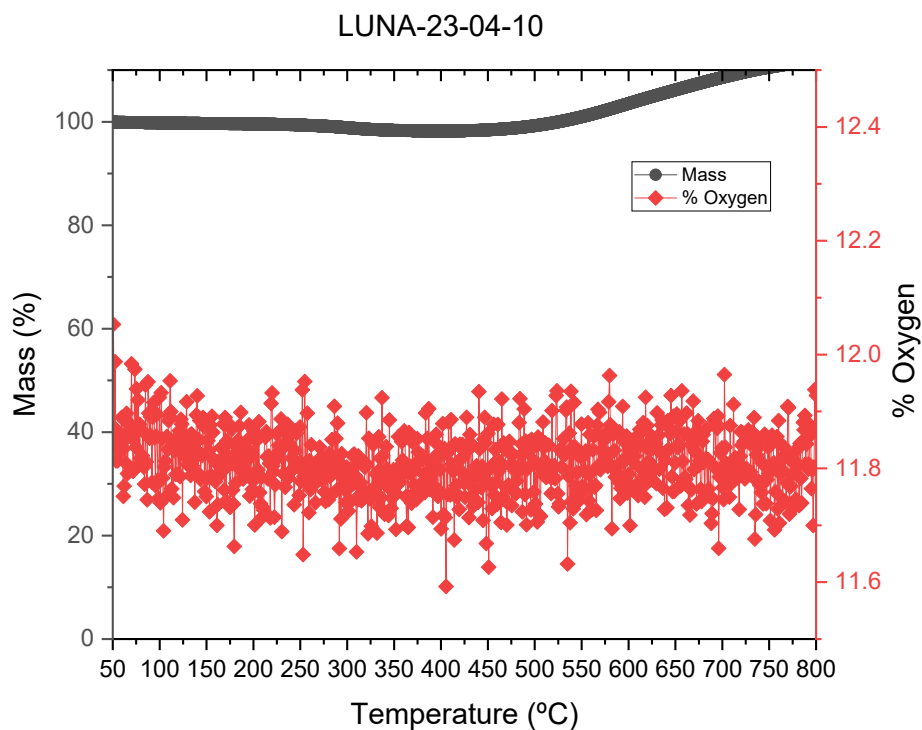


Figure 24. Thermogravimetric mass % plotted with % species detected in the exhaust by residual gas analysis. Listed gas species are most probable detected species [65].

While LUNA-23-04-10 did not evolve any detectable gases, one interesting observation is the gain in mass at higher temperatures. This mass gain is observed in Figure 19 and is attributed to oxidation of the zinc in the Zn-rich primer. To verify this, the relative % concentration of oxygen is plotted together with the TGA data in Figure 25. A slight decrease in the relative concentration of oxygen at temperatures between 250 °C and 500 °C is observed, indicating that the mass gain behavior can indeed be attributed to absorption of oxygen on the surface (i.e. oxidation of the Zn).





**Figure 25. TGA mass % plotted with % oxygen detected in the exhaust by RGA for LUNA-23-04-10. Compressed air was used as a cover gas for the TGA measurement which has an oxygen concentration of 20.5% but since the RGA was not calibrated for high concentrations this data should be regarded as relative concentration only.**

Outgassing analysis is an important metric by which it can be determined whether coatings are appropriate for application on SNF canisters. Further outgassing analysis will be performed on all candidate coatings with the inclusion of long isothermal holds and more sensitive gas analysis.

### 3.3 Long-term Thermal Exposure

In addition to TGA analysis, SNL also started long term thermal exposures. While TGA can be very insightful into the thermal degradation of a material, for this application it is also important to understand coating performance when a coating exists on a hot surface for an extended time, but at a temperature below the onset of thermal degradation. In FY23, SNL aged one of each of the coated coupons in an oven at 80 °C for known time intervals, then hardness, adhesion, and scratch tests were performed to observe the impact of temperature. 80°C was selected for this study because minimal thermal degradation was observed, at a ramp of 1 °C/min, but it is unknown how time at 80 °C would impact performance. This was also chosen because the radiation experiments using the high dose rate array (more details in Section 4.1) were sustained at 80°C during the entire experiment due to material self-heating. This work is ongoing and will be completed in FY24. In addition, FY24 work in this area will explore long term thermal exposures at additional temperatures, specifically 150 °C, 200 °C, and 225 °C. The results of these studies will help identify the canister thermal conditions in which a particular coating could be viable to provide long term protection against SCC.

This page is intentionally left blank.

## 4. RADIATION STABILITY

The ability of a coating to withstand the expected radiation on the surface of the canister is critical to both providing an effective corrosion resistant barrier and ensuring that the coating will not cause future problems during extended storage. A 2013, a study by Wittman [31] evaluated the radiation emitted from an SNF canister as a function of storage time from 0 to 300 years, assuming 45-48 GWd/MTU (4% <sup>235</sup>U) burn up (Figure 26). That data was applied to integrate the total dose a coating could see during its performance lifetime depending on the storage time prior to coating application. Because of radioactive decay, the dose rate is highest at time = 0 and decreases exponentially as a function of time. For example, if a coating was applied as a **prevention** method and was applied prior to the fuel being loaded, then for the 300 years of storage that coating would receive ~ 725 MRad at an initial dose rate of ~3 rad/sec. If a coating was applied as a **mitigation** strategy after five-to-twenty years of storage, then that total dose received from 5-300 and 20-300 years would be ~495 MRad and ~314 MRad, respectively. Storage times of 20 years could be a reasonable time-period to apply a coating as a mitigation strategy as these would align with the timing of the first regulatory inspection. Lastly, if a coating was used as a **repair** after 40 years of storage, then it would experience ~200 MRad from 40-300 years.

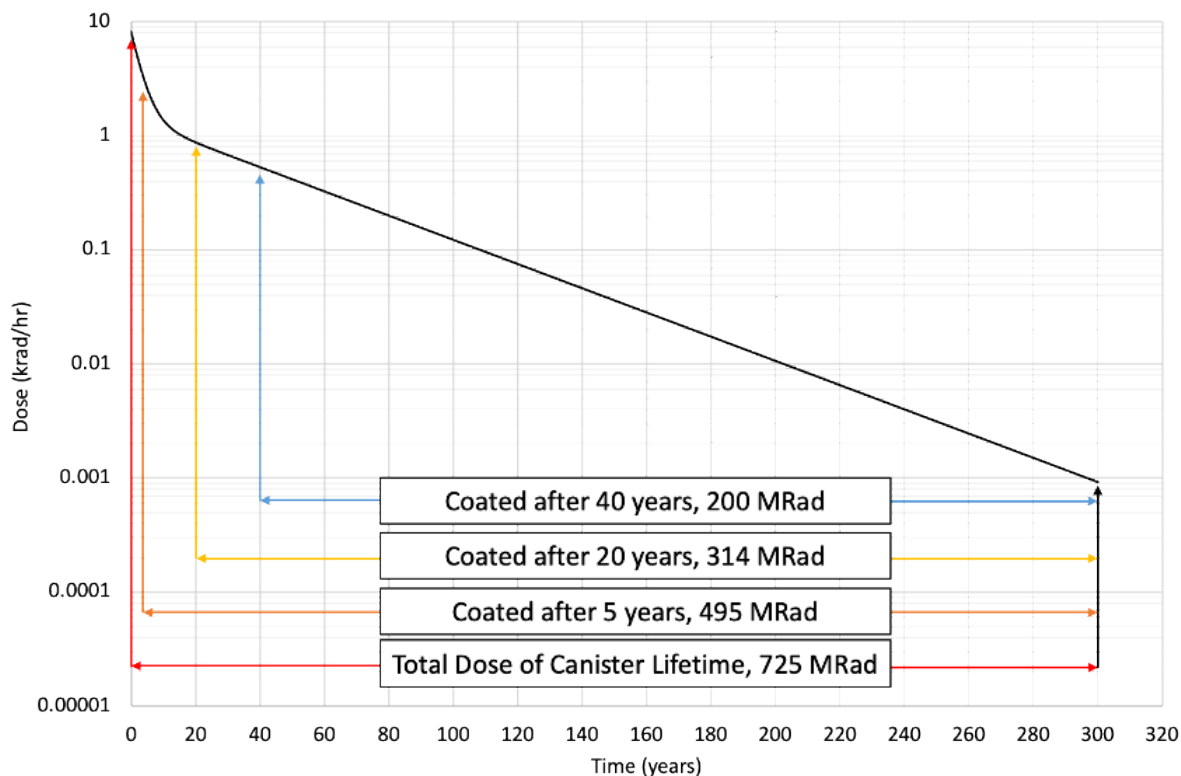


**Figure 26. Estimated dose rate at a canister surface assuming 45-48 GWd/MTU (4% <sup>235</sup>U) burnup over a period of 300 years [66]. Test intervals were chosen based on realistic inspection intervals (such as the first inspection performed after 20 years of storage).**

For this study, SNL evaluated the impact of received dose and dose rate on the physical, mechanical, and electrochemical performance of the coating candidates. This test was performed in February/March of 2023 at the Gamma Irradiation Facility (GIF) at SNL.

## 4.1 Experimental Set up

Six coupons of each of the eight coating candidates were exposed to gamma radiation at the GIF. Samples were placed in two different exposure cells: a linear <sup>60</sup>Co array (LA) and a circular <sup>60</sup>Co shutter array (SA). The LA was capable of a maximum dose rate of 176 rad/s and the SA was capable of 1200 rad/s (which could be adjusted by modifying the array aperture) at the time of testing. Each array was mounted on an elevator which hoisted the array out of the containment pool to start the exposure. The total exposure was calculated based on the time that the elevator was raised (and the samples were exposed to the array) and the measured flux of the array at the sample locations using an ion chamber. Different dose rates were achieved by placing samples at controlled distances from the source. The highest dose rate was achieved closest to the source and the dose rate decreased with the square of the distance from the source.

Six unique exposure conditions were selected and are shown in Table 4, along with the test cell location, dose rate, total dose, and the simulated application interval. The 350 Mrad exposure was performed at two exposure rates (169 rad/s and 1054 rad/s) to enable comparison of dose rate effects on the samples. Due to scheduling constraints at the GIF, the exposures could not be done in one continuous exposure; therefore, the dose rates varied slightly from set to set due to variations in array and sample alignment. The SA, which features an adjustable dose, was adjusted for each test interval as close to 1054 rad/s as possible but variations in the dose rate occurred. Despite these slight differences, further analyses will refer to the maximum dose rate (176 rad/s or 1054 rad/s) or the nominal target total dose (100, 200, 350, 730, and 1300 Mrad). The dose rates used in this study are several orders of magnitude higher than the maximum estimated canister surface dose rates (~ 3 rad/sec maximum); therefore, a rigorous study in dose rate effects is necessary to extrapolate any findings to long term application intervals.

**Table 4. Gamma Irradiation Test Matrix**

Test Cell	Average Dose Rate (rad/s)	Dose (Mrad)	Exposure Time (Hours)	Temperature During Exposure (°C)	Time to Achieve Dose in Prevention Scenario (Years)	Lifetime Dose Received After Storage Time Prior to Coating (Years)
LA	176	105	166	25	~0.6	> 60
LA	176	211	333	25	~ 3.5	> 40
LA	169	350	576	25	~12	> 20
SA	1054	351	93	80	~12	> 20
SA	1027	724	196	80	300	0
SA	957	1305	378	80	>300	Double expected dose

Samples placed in the LA were mounted on custom built wooden fixtures (Figure 27) to hold them at the correct height for uniform exposure in front of the linear source. Minimal metal was used in the construction of the fixtures to reduce attenuation and localized heating during exposure. The fixture was placed adjacent to the containment pool curb to achieve the highest dose rate possible in the linear array (Figure 28a). A short length of SS wire was stretched across the front of the samples to hold them in place during the exposure and to prevent them from falling into the containment pool. Each sample was wrapped in two layers aluminum foil to prevent potential outgassed species from contaminating the surrounding samples. The wrapped samples were stacked on the fixture in groups of three, with one coupon being removed from each group after each exposure interval. For example, after 166 hours all samples achieved 100 Mrad dose; then one coupon was removed from each group. The two remaining coupons were exposed for a further 167 hours to achieve the 200 Mrad dose. A second coupon was removed from each group—leaving one coupon in each group—which was exposed for another 234 hours to achieve 350 Mrad. The average dose rate achieved in the LA was 169-176 rad/s. Previous measurements performed by the GIF have demonstrated that samples exposed to the linear array maintain a temperature around ambient.

Samples placed in the SA (Figure 28b) were grouped into sample stacks. Each sample stack contained one of each coating, which were removed at different time intervals to achieve different doses. The sample stacks were overwrapped with another two layers of aluminum foil and a fiberglass insulated exposed junction T-type thermocouple was placed in the middle of the stack (between the fourth and fifth coupons) to measure the temperature of the stack during exposure. Three stacks of samples were placed into the SA and thermocouple wires were routed through the wall of the exposure cell to a data acquisition system with a cold junction compensated thermocouple amplifier. The SA was adjusted to a dose rate of average 957-1,054 rad/s at the time of testing. Because the sample stacks were approximately four inches thick, it is possible that some gamma attenuation occurred. Actual sample dose rates depend on each sample's location in the stack and in the basket; however, for this test, specific dose rates for each coupon were not determined and it was assumed all the samples within a stack experienced the same average dose rate.



**Figure 27. Wooden fixtures used to hold coating specimens in front of the linear  $^{60}\text{Co}$  array at Sandia's Gamma Irradiation Facility. Thin gauge 304 stainless steel wire was used to prevent the specimens from falling into the containment pool and to hold the specimens flat against the fixture during exposure. Samples were wrapped in foil to prevent abrasion against the wire (not shown).**

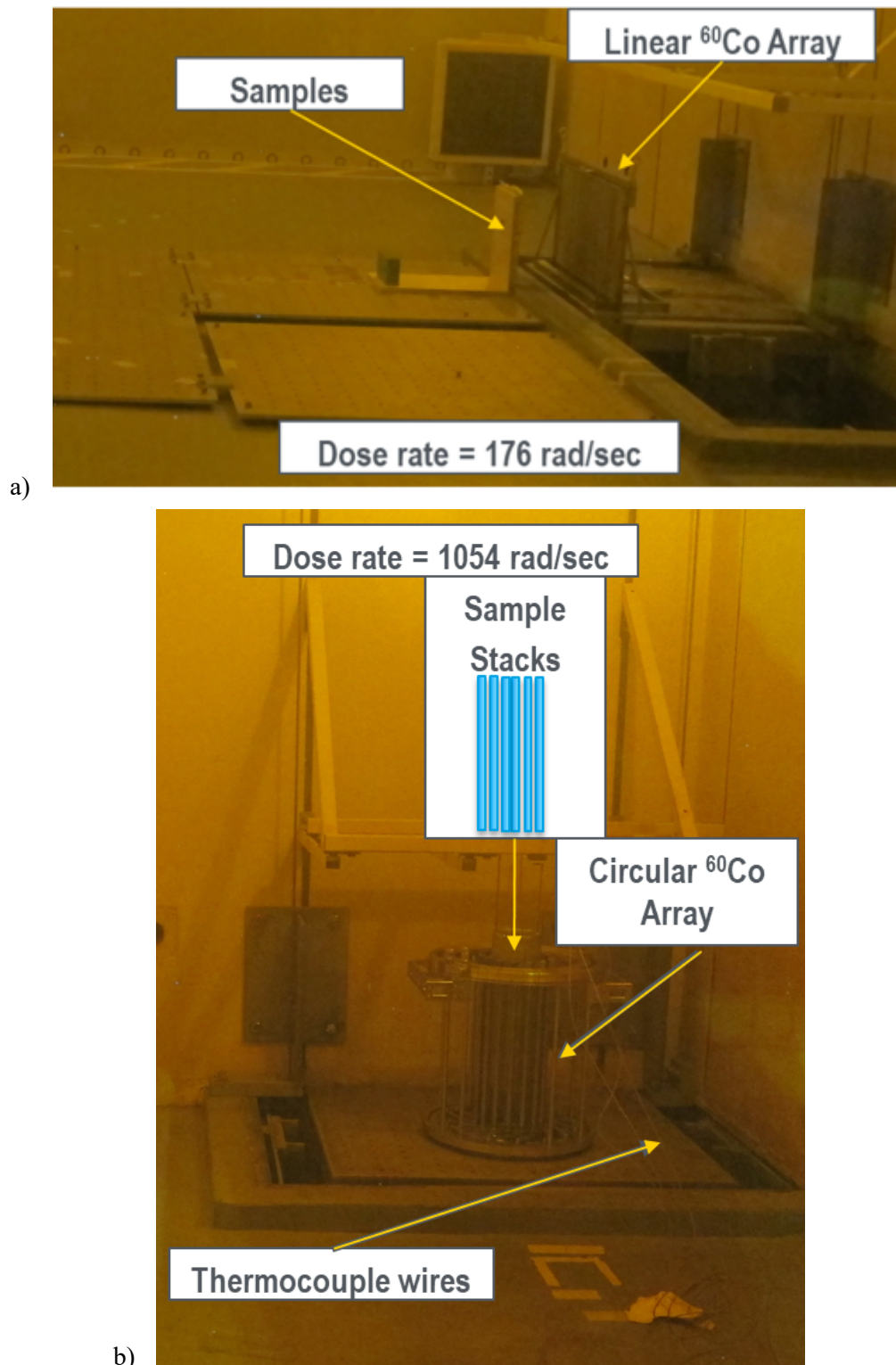
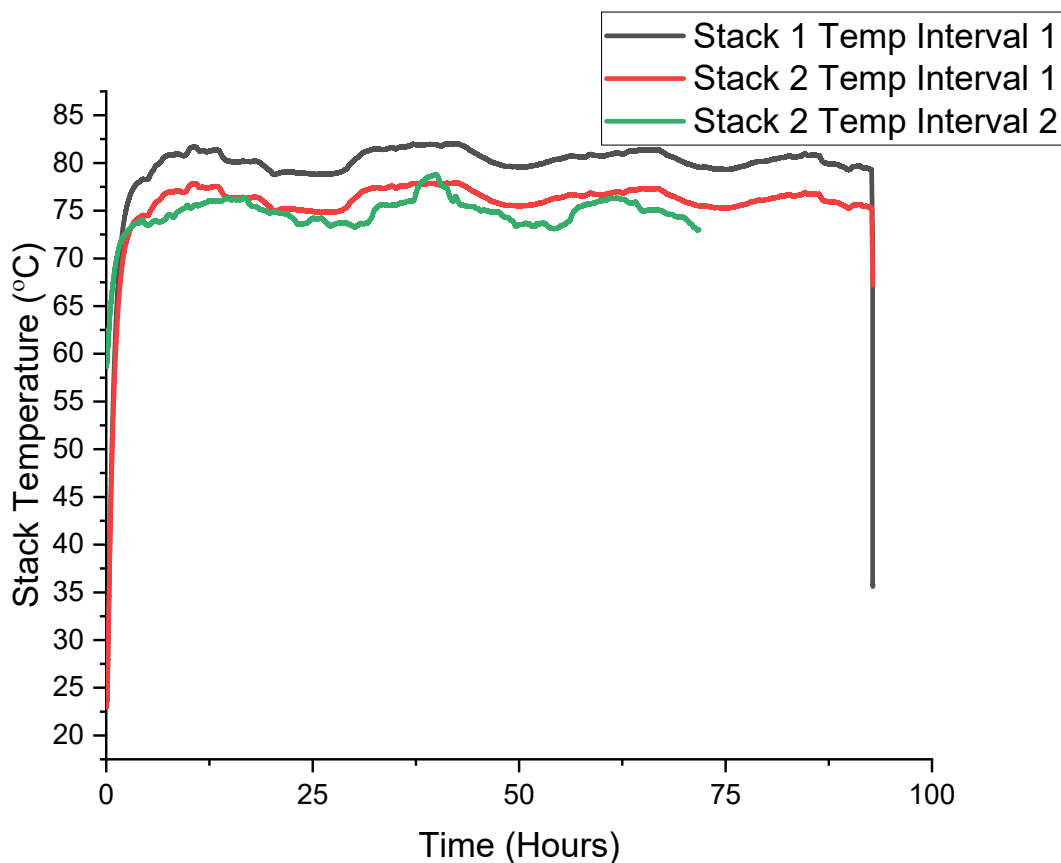


Figure 28. a) The linear array and b) the shutter array at Sandia's Gamma Irradiation Facility. Thermocouples were used to monitor the temperature of the sample stack during exposure using the shutter array.

The stacks placed in the SA self-heated during exposure due to the large mass of the stack and the high flux. The stack temperature stabilized between 72°C-82°C during exposure in the shutter array and varied about 5°C diurnally (Figure 29). The temperature of Stack 2 was monitored before and after a pause in the exposure (to remove stack 1) and showed similar temperatures before and after the pause (Figure 29 “Stack 2 Interval 1” vs “Stack 2 Interval 2”). Since Stack 1 was removed before “Stack 2 Interval 2” measurements were made and the temperature returned to the approximately same value, it is unlikely that the stacks were heating each other.



**Figure 29. Stack temperature during exposure in the GIF shutter Array (dose rate 1054 rad/s). Stack 1 was removed after 93 hours (achieved 350 Mrad). Stack 2 (735 Mrad) was replaced and self-heated to the same temperature.**

The experimental setup performed at the GIF is similar to the ASTM D4082 method—gamma radiation for use in nuclear power plants [47]—though the method here does not fully meet the specification provided by the standard. Deviations from the standard were performed to have better resolution in our understanding of the effect of radiation as well as dose rate effects. In addition, more rigorous evaluation of the coating performance as a function of radiation was performed in these studies. The goal of this test was not to qualify a particular coating for use in a nuclear power plant, but to understand its performance following gamma irradiation.

In the ASTM standard, coupons are to be exposed to 1000 Mrad at a dose rate of ~275 rad/sec using a <sup>60</sup>Co source or greater with 10% uniformity from sample to sample and maintain a temperature <60 °C. Specific differences between the ASTM standard and the work at SNL are as follows.



- Samples irradiated with the LA were subjected to dose rates that were too low (176 rad/s max) and the total dose was too low (350 Mrad). It is important to note that for this application, a lower dose rate is more applicable.
- While samples irradiated in the SA were subjected to dose rates that were high enough (1,054 rad/s max) and only the 1300 Mrad samples met the dose threshold specified in the standard (1000 Mrad), the samples achieved temperatures > 60 °C (exceeding the standard); therefore, some of the observed degradation that occurred could have been due to temperature effects in addition to the radiation effects.
- The examination method recommended in the ASTM standard are primarily visual inspection methods, specifically evidence of chalking (ASTM- D659), cracking (ASTM- D661), blistering (ASTM – D 714), flaking (ASTM – D 772), or delamination [47]. These tests were not specifically performed, but visual inspection of these specific defect types was performed at SNL.
- SNL performed mechanical tests including scratch, hardness, and adhesion, to determine the impact of irradiation.

## **4.2 Visual inspection and Color Change**

All coating samples were photographed after exposure to document any defect and color changes that may have occurred due to irradiation. Color changes are a strong indication of chemical changes in polymeric coatings and have been previously investigated [67, 68] and could be a good qualitative assessment of coating condition in the field. Three coatings exhibited dramatic color changes (Figure 30) as a result of irradiation. At baseline TDA-23-01-01 was a brilliant white color, but with increasing amounts of irradiation the coating developed a yellow hue. The changes in FC-23-01-XX are subtle at lower doses but at the highest dose yellowing was also observed as was obvious cracking on the surface. LUNA-23-03-XX showed more yellowing on samples exposed in the SA at higher rates. The LUNA-23-03-07 with the highest total dose (far right of the image) appears to have delaminated or flaked off the substrate entirely as a result of exposure.

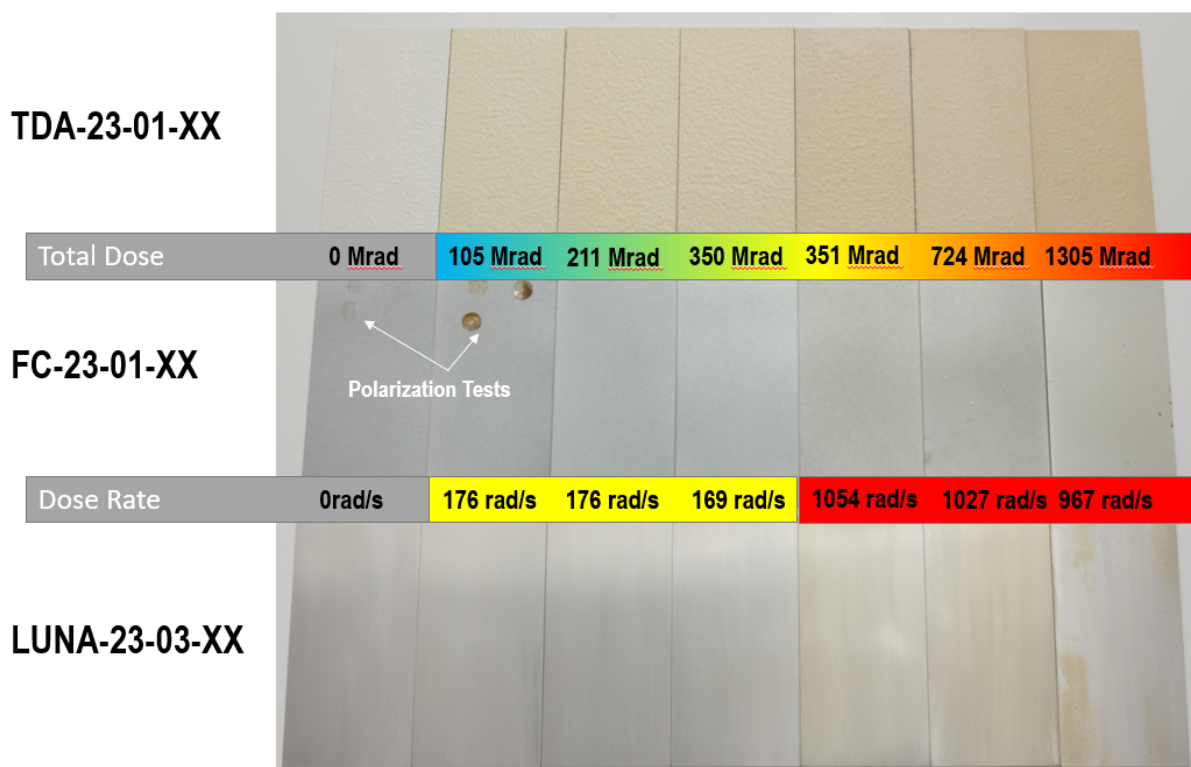


**Figure 30. Color comparison of coatings after exposure to increasing (left to right) doses of gamma radiation. These coupons exhibited the most obvious color changes, yellowing with increasing exposure.**

Individual images of each coupon were captured before and after exposure, and colorimetric comparison was conducted consistent with the procedure used in the FY22 report [1]. A 500x500 pixel area in the middle of each coupon was extracted from each image and the RGB pixel values were averaged to obtain a representative color. The representative colors are shown for each coating, dose rate, and total dose in Figure 31. Most coatings do not appear to change dramatically with irradiation other than those noted previously, including TDA-23-01-XX, FC-23-01-XX, and LUNA-23-03-XX. For OPM-23-0-XX color variations in the “as-received” coupons were significant—particularly the 350 Mrad (SA) coupon from FY22 which was a different color from the rest of the coupons for that coating.

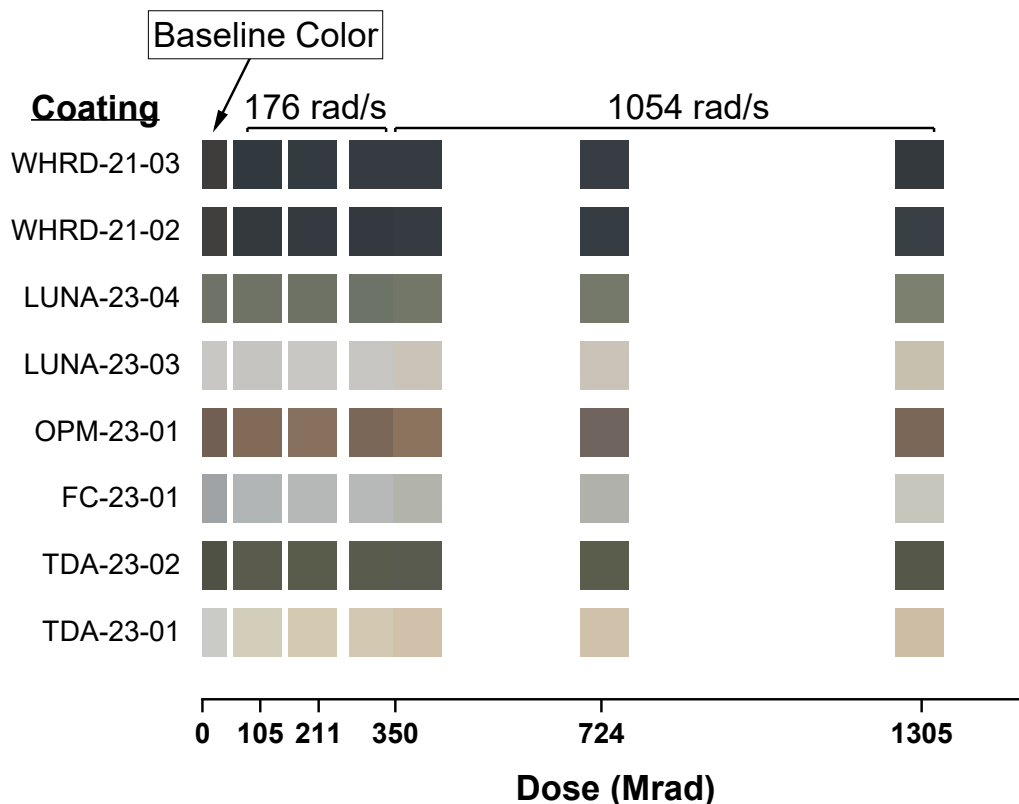


**Figure 31. Colorimetric representation of baseline and gamma irradiated samples. Some coatings had high variability in baseline color while others exhibited yellowing with increasing dose.**

Averaged RGB values shown in Figure 32 show the influence of irradiation on each color component. In general coatings that exhibited visible yellowing showed darkening in the green and blue color contributions. The remaining coupons that did not appear to yellow showed slight lightening in the red color contribution but minor changes in the red and blue components. Color changes in polymers exposed to gamma radiation have been documented in previous studies as thermal-oxidation or photo-oxidation [69, 70] which is also sensitive to thermal conditions—this may explain why the 350 Mrad samples appeared to be more yellow when exposed in the SA versus the LA.

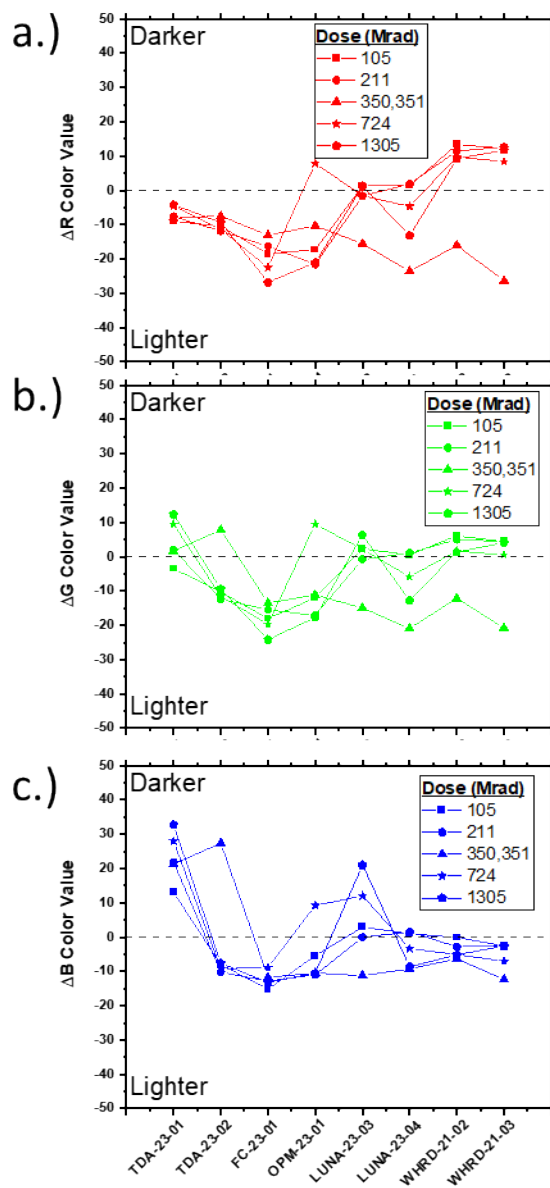


Figure 32. Colorimetric analysis of Red (a), Green (b), and Blue (c) color channels relative to baseline values.

### 4.3 Mechanical Testing

Mechanical and physical tests were performed on each of the coating candidates as function of radiation dose. These tests included hardness testing, adhesion testing, and scratch testing. Material hardness can be an indication of material integrity and possible changes in chemistry because of the exposure environment. Specifically for materials with organics, gamma irradiation can cause material softening by breaking the polymer linking bonds in a process known as chain scission. While coating softening can be an indication of radiation damage, it may not disqualify a coating if its performance is still adequate. Adhesion and scratch tests were performed similar to the FY22 report [1]. These tests were also performed as a function of radiation dose and dose rate and can provide useful information regarding

susceptibility to delamination or scratching. This will help inform what types of mitigation and repair scenarios are possible for a given coating. Sufficient surface adhesion is important to consider if the canister will be moved or handled following coating application; specifically, for **ex situ prevention** and **ex situ repair** scenarios. This may also be true for **in situ repair** if the canister needs to be moved to another location. Adhesion, scratch, and hardness testing help provide a clear picture of the ability of the coatings to adhere to the surface and begin to ascertain if their adhesive properties are sufficient to withstand the most extreme canister-specific forces as they age in a radiation environment. As mentioned in the FY22 report, no formal acceptance criteria have been determined for the necessary adhesive strength of a coating. However, it has been suggested that adhesion > 5000 psi is required but it is unclear how that specific number was determined, and is likely not feasible for many coatings [1, 27].

### **4.3.1 Hardness**

To understand the hardness of the coatings, a REED Instruments R9030 Leeb hardness tester was used to examine the hardness changes for each coating at various radiation exposures. Leeb hardness was the chosen method due to its ease of application, portability, and quick test results. The Leeb hardness test is described in ASTM A956-22 [71] as a dynamic method to determine the hardness value of a test piece. The Leeb hardness test method determines the hardness of a test piece from the ratio of an impactor's (typically a tungsten carbide ball) velocity before and after impact at 1 mm from the test subject's surface. The Leeb hardness value is calculated using the following equation:

$$L = \frac{\text{Rebound Velocity}}{\text{Impact Velocity}} \times 1000$$

There are many disadvantages of Leeb hardness testing given our application, one being that the method is designed for stiff metallic materials and can give varying results depending on sample surface roughness and thickness. Leeb hardness testing also isn't suited for test objects less than 5kg. Given the wide variety of coating thicknesses, material composition, surface roughness, and the thin coupons on which the coatings were applied other hardness testing methods are being explored and applied in FY24.

The hardness tester was configured for a vertical impact direction and measurement tolerances of 170HL-950HL with a substrate of stainless steel. Samples were rigidly clamped on a large steel block weighing approximately 5kg.

A minimum of six tests were performed on each coating variation, and the averages were plotted (Figure 33). The purely polymeric coatings (OPM-23-01-XX, TDA-23-01-XX, and all WHRD) had the highest initial hardness but had the highest spread in hardness values. Sensitivity to self-heating in the SA is also evident at 350 Mrad as most purely polymeric coatings had higher hardness in the SA than in the LA. At higher doses (SA), hardness increased to approximately the same value as unirradiated baseline values. The hardness values for the ceramic hybrid coatings did not exhibit strong sensitivity to dose or to the self-heating in the SA. This is consistent with expectations since these coatings are designed with higher temperature operating conditions in mind. The zinc rich primer coatings had high variability in hardness at baseline and at lower doses (in the LA), but with increasing dose the variability decreased and converged to nearly the same value for both coatings ( $L \approx 350$ ).

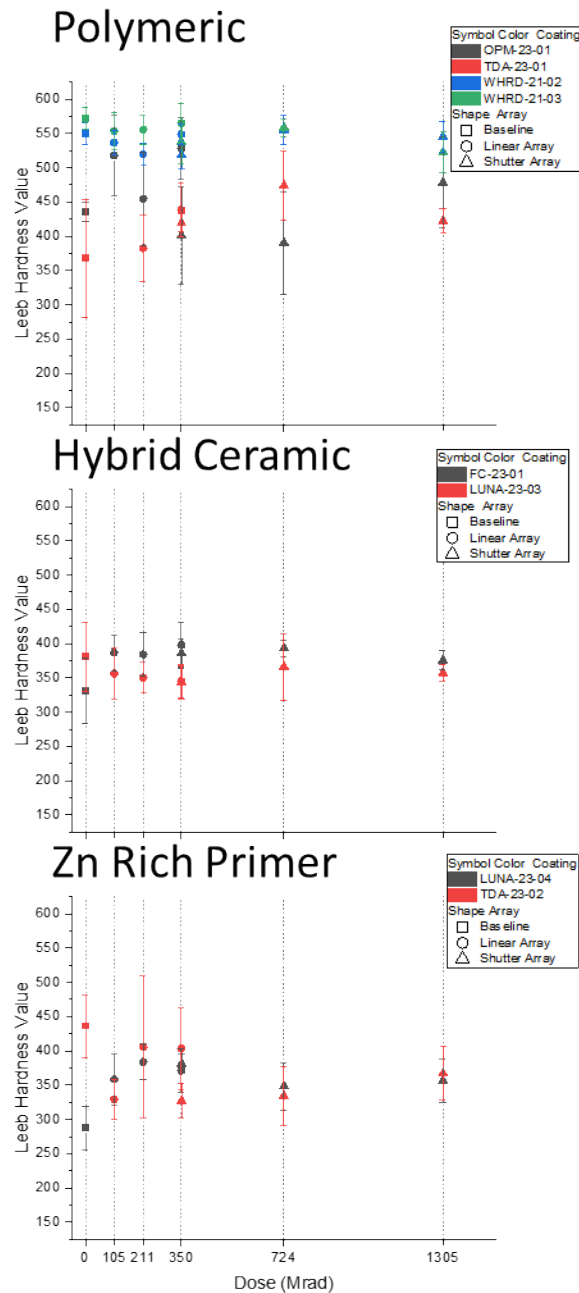


**Figure 33 Leeb hardness values for all coatings before and after exposure to gamma radiation. LUNA-23-04 comprises LUNA-23-03 coated on top of a zinc rich primer underlayer.**

To implement different hardness testing methods, nanoindentation will be performed on all coatings following radiation exposure. So far in FY23, the nanoindentation tests were only performed on a small selection of coatings to determine changes in hardness and modulus of elasticity after irradiation. A Micro Materials NanoTest pendulum nanoindenter equipped with a Berkovich diamond indenter was used for analysis. The indenter was first calibrated with a fused silica sample to apply an accurate diamond area function to displacement measurements of tested samples. Due to variability in thickness and roughness between sample coatings, different load-controlled experiments were performed thus far. For the TDA-

23-01 samples, which had a more uneven coated surface, several single indentation tests were done at 250 mN. For the LUNA-23-03 samples, a 5 x 5 array of increasing loadings (5mN, 50 mN, 100 mN, 150 mN, and 250 mN) was conducted to determine radiation effects with respect to depth. Parameters for all experiments had a loading rate of 2 mN/s, dwell at maximum load for 30 s, and drift correction dwell of 30 s after unloading.

From initial tests, effects from radiation are apparent (Figure 33), with irradiated samples experiencing greater plastic depths with increasing dose, resulting in lower elastic modulus and hardness compared to non-irradiated, baseline coatings (Table 5). This softening effect has been observed in other studies and is largely understood to be due to thermal oxidative reactions and resultant chain scission [67, 72].

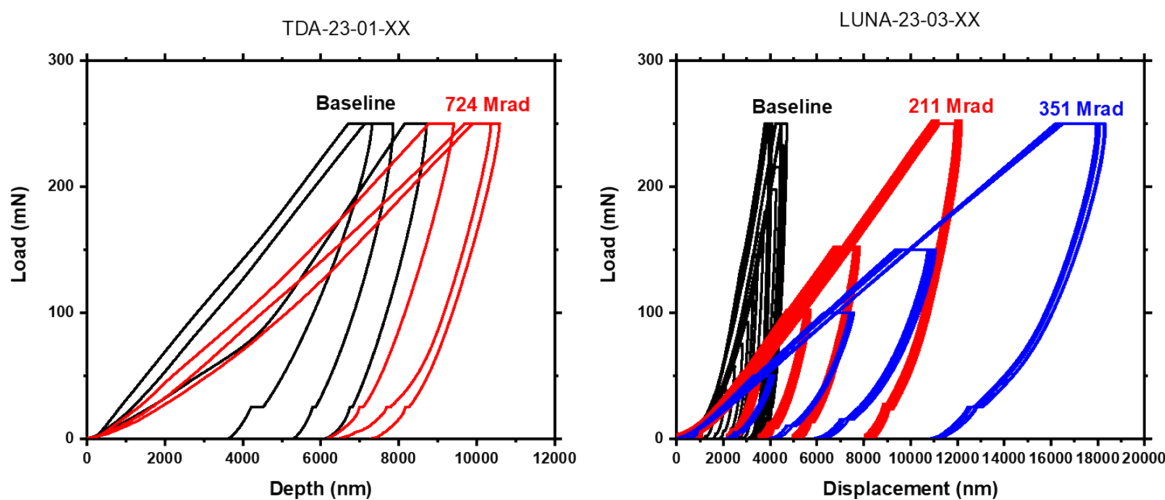


**Figure 34. Nanoindentation data from two coatings exposed to gamma radiation. Samples generally exhibited softening with increasing dose.**

**Table 5. Nanoindentation summary data on gamma irradiated coatings.**

Coating	Dose (Mrad)	Dose Rate (rad/s)	Modulus (GPa)	Hardness (MPa)
TDA-23-01-01	0	0	4.68	362
TDA-23-01-06	724	1054	3.50	200
LUNA-23-03-01	0	0	53.16	0.94
LUNA-23-03-03	200	175	4.97	0.265
LUNA-23-03-05	351	1054	2.88	0.205

Due to sample geometry and space requirements for the NanoTest instrument, samples will be cut in FY24 to facilitate the measurement of these coupons.

### 4.3.2 Adhesion Tests

Similar to FY22, the adhesive strength of the coatings was quantified using *ASTM D4541-17*, which is a direct approach to characterize the adhesion of a coating [1, 73]. In this test, the load required to remove a coating from a substrate is quantified by measuring the “pull-off” force by using a DeFelsko PosiTest AT-A hydraulic pull off tester. A 0.393 inch (10 mm) diameter aluminum test dolly (adhered using epoxy to the coating surface) is loaded at a rate of 100 psi/sec to a maximum achievable pull off force for the instrument, which is ~1,700 lbs, or until failure occurs [74]. Since the pull-off force is distributed over a known area (in this case a 10mm dolly has an area of 0.122 square inches), results are reported in psi. In FY22, it was determined that the epoxy used to mount the dolly to the coating surface is a critical component to this measurement as failures observed at the epoxy|coating or epoxy|dolly interfaces do not provide any useful information regarding the coating adhesion. This is referred to as Type 3 failure.

Therefore, it was important to find an epoxy that would sufficiently bind to the coating surface and the aluminum dolly. In FY22, it was determined that Loctite EA-1C and the Araldite 2011 had sufficient bonding strength to most of the coatings to result in coating failure. Additionally, higher pull off forces were attained following plasma surface cleaning using an Diener Nano plasma chamber in an 80:20 Ar:O<sub>2</sub> environment for 1 min at 100 W and 0.5 mbar (which activated the coating surfaces) and by curing the dolly epoxies at 40°C for 2-3 days [1]. Following plasma cleaning, coupons were transferred to clean bags and the dollies were mounted in less than four hours. The 10 mm aluminum dollies were lightly abraded with 180 grit sandpaper and cleaned with organic solvent. The epoxy (either EA-1C or Araldite 2011) was mixed (per manufacturer mixing instructions) and applied to the cleaned coating surface and to the dolly. The dolly was pressed firmly onto the surface of the coating. The coatings with the attached dolly were then cured in an oven at 40 °C for 48-72 hours to ensure a solid bond. For each coating, two-to-four dollies were adhered for a given test. Then, the PosiTest AT-A was affixed to the dolly and a uniform, gradual load was applied to the stud perpendicular to the coating surface. The load continued to increase until the dolly was removed from the surface and failure was achieved.

In adhesion testing, three possible failure modes exist;

- 1) *adhesive* failure to substrate,
- 2) *cohesive* failure within the coating,
- 3) epoxy failure and coating remains fully intact.

Depending on the failure mode, the information gained from the tests are different. For example, when a coating experiences *adhesive* failure (Type 1), the pull off force required to cause failure represents the strength of the coating to adhere to the SS surface. When a coating experiences *cohesive* failure (Type 2), the force required to pull the dolly off does not necessarily represent the strength of the adhesion of the coating to the SS surface, but rather the intra-coating strength. Lastly, when epoxy failure occurs (Type 3), the force required to remove the dolly from the surface only represents a minimal value for the adhesive strength of the coating to the surface and the intra-coating strength. For both cohesive failure and epoxy failure (Type 2 and 3) the adhesive strength of the coating is greater than the reported value (though unknown) and the SS surface remains protected.

Building off the results from last year, effort was made to find the right epoxy and cleaning procedure to maximize the Type 1 or Type 2 failures so that the test evaluates the coating adhesion to the substrate. Loctite EA-1C was used on OPM-23-01-XX, and LUNA-23-03-XX. Araldite 2011 was used on WHRD-21-02-XX, WHRD-21-03-XX, FC-23-01-XX, and LUNA-23-04-XX. Both epoxies were tested with TDA-23-01-XX and TDA-23-02-XX because these coatings were not evaluated in FY22. To date, Type 1 or Type 2 failure was induced in all coatings as a function of dose except for OPM-23-01-XX, on which only Type 3 failure was observed.



For each coating candidate, the adhesive strength of the coating was evaluated as a function of radiation dose (see Figure 35, and Table 6 -Table 8 ). In general, the adhesion results show that the adhesive properties the coatings were negatively affected by radiation exposure. This was observed by a decrease in the pull off force required to remove the dolly and, in some cases, a change in the failure mode to a more severe failure was observed (for example, a baseline failure mode of Type 3, followed by a transition to Type 2 and Type 1 as radiation dose increased). The exception was OPM-23-01-XX, only Type 3 failure was observed – for baseline samples and all irradiated samples.

**Table 6. Detailed summary of the adhesion tests as a function of radiation for the zinc rich coatings candidates.**

Zinc Rich Coatings		Baseline	LA 105Mrad	LA 211Mrad	LA 350Mrad	SA 351Mrad	SA 724Mrad	SA 1305Mrad
LUNA-23-04	Failure Type	1	1	1	1	1	1	1
	% psi change from baseline		-19%	-16%	-17%	-12%	1%	-29%
	% psi change from previous exposure		-19%	4%	-2%	7%	15%	-30%
	Average psi to failure	558.33333	452.33333	470.33333	461	491	565.66667	395.66667
	Trend	No significant change in adhesive strength with an increase in radiation.						
TDA-23-02	Failure Type	1	1	1	1	1	1	1
	% psi change from baseline		40%	45%	34%	24%	30%	4%
	% psi change from previous exposure		40%	3%	-8%	-7%	5%	-20%
	Average psi to failure	403	565.66667	582.5	538.5	498.33333	525.5	418.5
	Trend	Adhesive force increases with initial radiation exposure. No significant change in adhesive strength with a further radiation exposure.						

**Table 7. Detailed summary of the adhesion tests as a function of radiation for the ceramic coating candidates.**

Ceramic Coatings		Baseline	LA 105Mrad	LA 211Mrad	LA 350Mrad	SA 351Mrad	SA 724Mrad	SA 1305Mrad
FC-23-01	Failure Type	3	1	1	1	1	1	1
	% psi change from baseline		-50%	-51%	-64%	-54%	-63%	-71%
	% psi change from previous exposure		-50%	-2%	-26%	27%	-21%	-20%
	Average psi to failure	864	432	424	315	399.66667	316.33333	252.66667
	Trend	Coating adhesive force decreases with an increase in radiation exposure. Adhesive force increases when transitioning from linear to shutter array.						
LUNA-23-03	Failure Type	3	3	2	1	1	1	1
	% psi change from baseline		-9%	-39%	-28%	-42%	-55%	-36%
	% psi change from previous exposure		-9%	-33%	18%	-19%	-22%	44%
	Average psi to failure	850.5	772.5	516	608.5	490.5	380.5	547.33333
	Trend	Coating adhesive force decreases with an increase in radiation exposure.						

**Table 8. Detailed summary of the adhesion tests as a function of radiation for the polymer coating candidates.**

Polymer Coatings		Baseline	LA 105Mrad	LA 211Mrad	LA 350Mrad	SA 351Mrad	SA 724Mrad	SA 1305Mrad
TDA-23-01	Failure Type	3	2	2	2	2	1	1
	% psi change from baseline		0%	-24%	-43%	-56%	-65%	-74%
	% psi change from previous exposure		0%	-25%	-25%	-23%	-20%	-25%
	Average psi to failure	1369.5	1376	1037.3333	778.66667	600	480	361.33333
	Trend	Adhesive force decreases with an increase in radiation exposure.						
OPM-23-01	Failure Type	3	3	3	3	3	3	3
	% psi change from baseline		112%	93%	99%	132%	81%	109%
	% psi change from previous exposure		112%	-9%	3%	17%	-22%	15%
	Average psi to failure	540	1146.5	1042.5	1073.75	1253	979.75	1130.75
	Trend	*Epoxy to coating adhesive strength increased with initial radiation exposure.						
WHRD-21-02	Failure Type	3	2	2	2	2	2	2
	% psi change from baseline		-43%	-61%	-66%	-47%	-56%	-63%
	% psi change from previous exposure		-43%	-32%	-12%	57%	-17%	-16%
	Average psi to failure	2138.3333	1213.3333	824.66667	725.5	1138.6667	941.66667	795.33333
	Trend	Coating adhesive force decreases with an increase in radiation exposure. Adhesive force increases when transitioning from linear to shutter array.						
WHRD-21-03	Failure Type	3	2	2	2	2	2	2
	% psi change from baseline		-52%	-56%	-65%	-41%	-57%	-55%
	% psi change from previous exposure		-52%	-9%	-21%	68%	-27%	6%
	Average psi to failure	1755.3333	851	776	615	1031.6667	749.33333	791.33333
	Trend	Coating adhesive force decreases with an increase in radiation exposure. Adhesive force increases when transitioning from linear to shutter array.						

\* - OPM-23-01-XX irradiated coatings' surface was roughened prior to test. OPM-23-01-XX baseline coatings were not roughened prior to test. This could be a reason for the increase in adhesive force required to induce failure. Future work will be done on OPM-23-01-XX baseline coatings with roughened coating surfaces to maintain consistency in data acquisition.

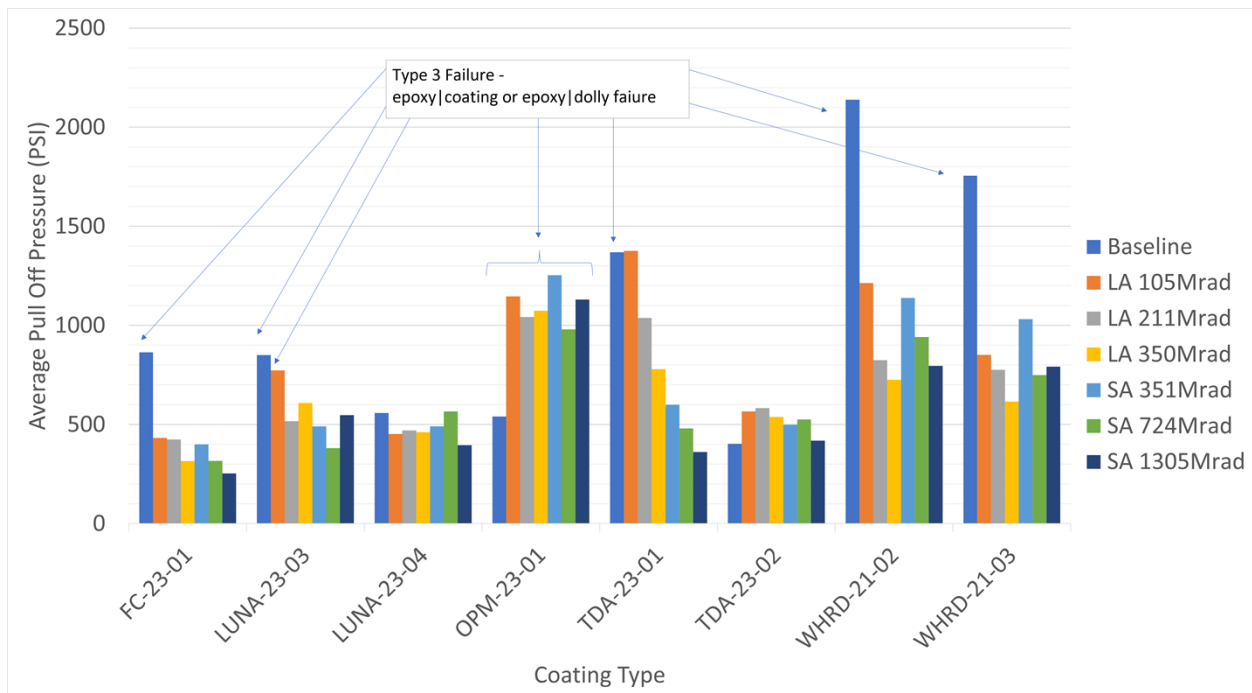


**Figure 35. Average pull off pressure (psi) as a function of coating type with clustered columns of total radiation exposure (Mrad).**

The change in adhesion from the baseline value may be an easier way to compare the behavior of coatings after exposure to gamma radiation (see Figure 36). As observed previously, most coatings exhibited a decrease in adhesion values and a corresponding change in failure mode, not shown here. OPM-23-01 was the exception, indicating an increase in adhesion strength, but due to the Type 3 failure mode this is only attributed by an increase in the strength of the dolly/coating interface. TDA-23-02 showed a small increase as well but this could have been within the noise of the measurement.

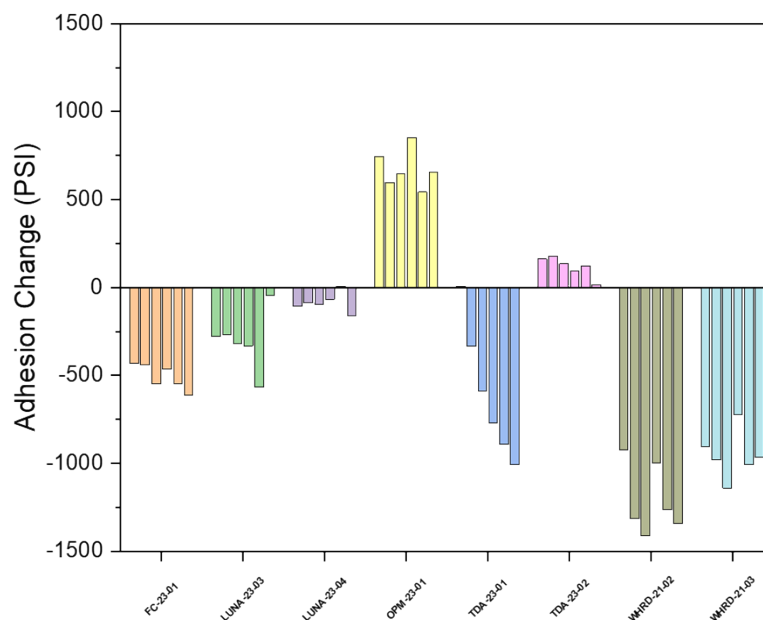


**Figure 36. Adhesion value change for each coating with respect to baseline, unirradiated coatings. Each sample group is organized by increasing dose (left to right). High positive change in adhesion for OPM-23-01 represents an increase in surficial bond between adhesion test dolly and coating surface but does not represent an increase in actual adhesion strength.**

Coatings consisting of purely organic components typically had the highest baseline adhesive strengths (>1000 psi/Type 3 failure) but are possibly most susceptible to radiation damage. Adhesion tests of TDA-23-01-XX resulted in a clear relationship between coating adhesion, failure mode, and radiation dose [(Figure 37)]. Adhesion tests of the non-irradiated sample resulted in the higher pull off forces and occurred via Type 3 failure at the epoxy/coating interface. As radiation dose increases, the pull off force required to remove the dolly decreased and the failure mode shifted from primarily Type 3 (baseline, 105 Mrad) to primarily Type 2 (211, 350, and 351 Mrad), to primarily Type 1 failure (724 and 1305 Mrad). These results clearly demonstrate that exposure to gamma radiation impacts the adhesive strength of the TDA-23-01-XX epoxy based coating. While it is unknown exactly which bonds within the epoxy are breaking, the unconjugated C-C or C-O may be most susceptible due to the weakest bond energies.

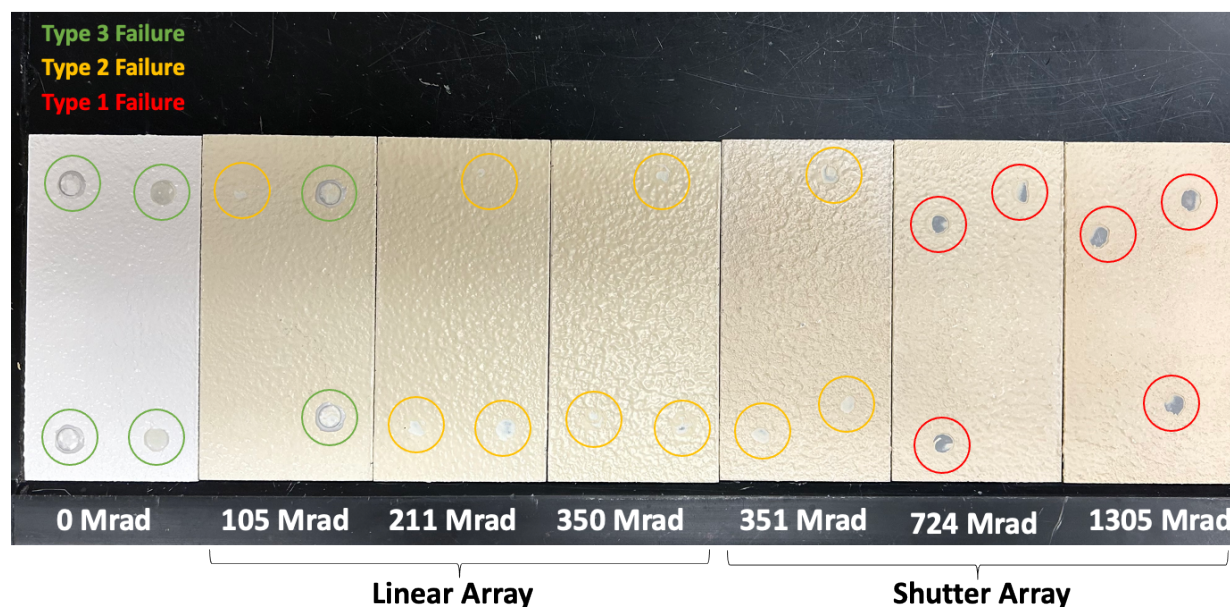


**Figure 37. Photo showing the type of failure observed during the adhesion tests for TDA-23-01-XX as a function of radiation.**

When unexposed, the WHRD-21-02-XX and WHRD-21-02-XX had very high adhesion strength and only observed failure are epoxy/coating interface for Type 3 failure. However, when irradiated, a significant decrease in the pull off force was observed. In addition, the failure type changes from Type 3 to Type 2 in all irradiated samples. This suggests that some coating degradation is occurring when exposed to gamma radiation. Interestingly, there is a distinct discontinuity between the pull off force in samples exposed to the LA versus the SA, which the SA samples had a noted increase in the pull off force relative to the trend seen with the LA. It is also possible that self-heating at 80 °C may have altered the adhesive strength of the sample. While the OPM-23-01-XX sample is a polymeric coating, no adhesive failure was seen in the baseline sample nor at any exposure dose, as these samples only failed via Type 3 failure.

In FY24, further improvements to the adhesion testing of OPM-23-01-XX will be attempted. In preliminary experiments, simple abrasion increased adhesion on OPM-23-01-XX by up to 154%. Future improvements include primers or tribological surface activation techniques, such as media blasting. [75]

The ceramic hybrid coatings, FC-23-01-XX and LUNA-23-03-XX had moderate baseline adhesive behavior (~900 psi/Type 3). When these samples were exposed to radiation their adhesive strength decreased and transitioned from Type 3 failure to Type 1 failure. This was more obvious for FC-23-01-XX, as there is a larger amount of polyurethane in that coating relative to LUNA-23-03-XX. A photo of the FC-23-01-XX coupons following radiation and adhesion tests is shown in Figure 38. Interestingly, when exposed to 351 Mrad-SA, the FC-23-01-04 coupon had improved adhesion behavior relative to the existing trend. This could be a result of thermal effects during the exposure in the SA. Overall, radiation effects decreased the adhesive strength of LUNA-23-03-XX. Interestingly, the results after exposure to 1305 Mrad exhibit behavior similar to bare SS, suggesting the coating may have disintegrated. Future SEM/EDS analysis of this coating will be used to confirm this hypothesis.

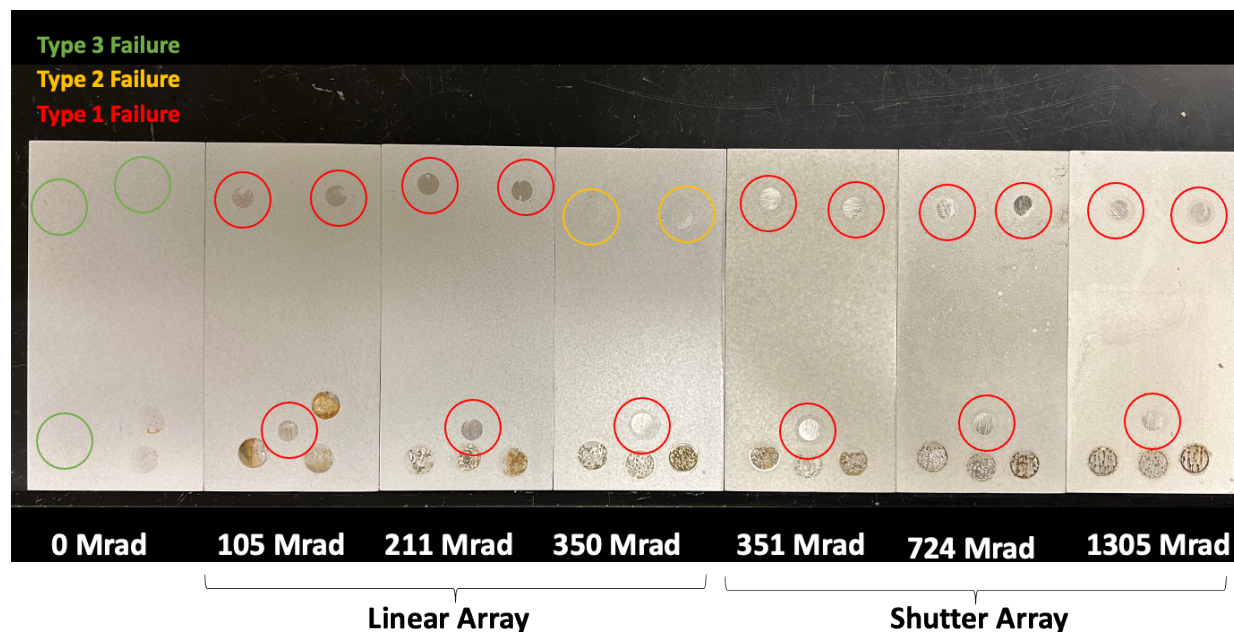


**Figure 38. Photo showing the type of failure observed during the adhesion tests for FC-23-01-XX as a function of radiation.**

The samples with the Zn-rich primer, including LUNA-23-04-XX and TDA-23-02-XX, behaved similarly. The non-exposed samples failed adhesively (Type 1), and that failure mode was maintained throughout all radiation exposures. The pull off force slightly decreased as function of radiation exposure; however, overall, the pull off force was more consistent from sample to sample compared to the other types of coatings.

### 4.3.3 Scratch Tests

Scratch resistance is being evaluated, by ASTM D7027-13 [76], using a commercial scratch tester from Anton Paar GmbH Revetest® RST<sup>3</sup> on the coatings at each radiation exposure of interest, similar to the scratch resistance procedure used in FY22 [1]. Scratch testing was used to qualify and quantify surface damage of the coating by measuring many significant material parameters. These surface damage measurements, as a function of radiation, can further identify coating resistance to different levels of radiation exposure. Scratches were performed using a 200-micron radius diamond stylus over a scratch length of 10 mm at a scratch speed of 1 mm/min. Three scratches per coating were performed. Final load and load rate of coatings scratches were varied to better represent the variation in coating thickness and stiffness. Final loads were chosen based off the results from FY22 coating thickness evaluations [1].

Panoramic photomosaics of the scratch area were created using a Keyence VHX-5000 digital optical microscope at 100x magnification. The width and area of the scratch was measured using Bluebeam. TDA-23-01-XX was scratched and imaged and is shown in Figure 39. With increasing dose, the scratch area generally decreased, which implies that the coating hardened. The loads, speeds, and scratch lengths in these images remained the same.

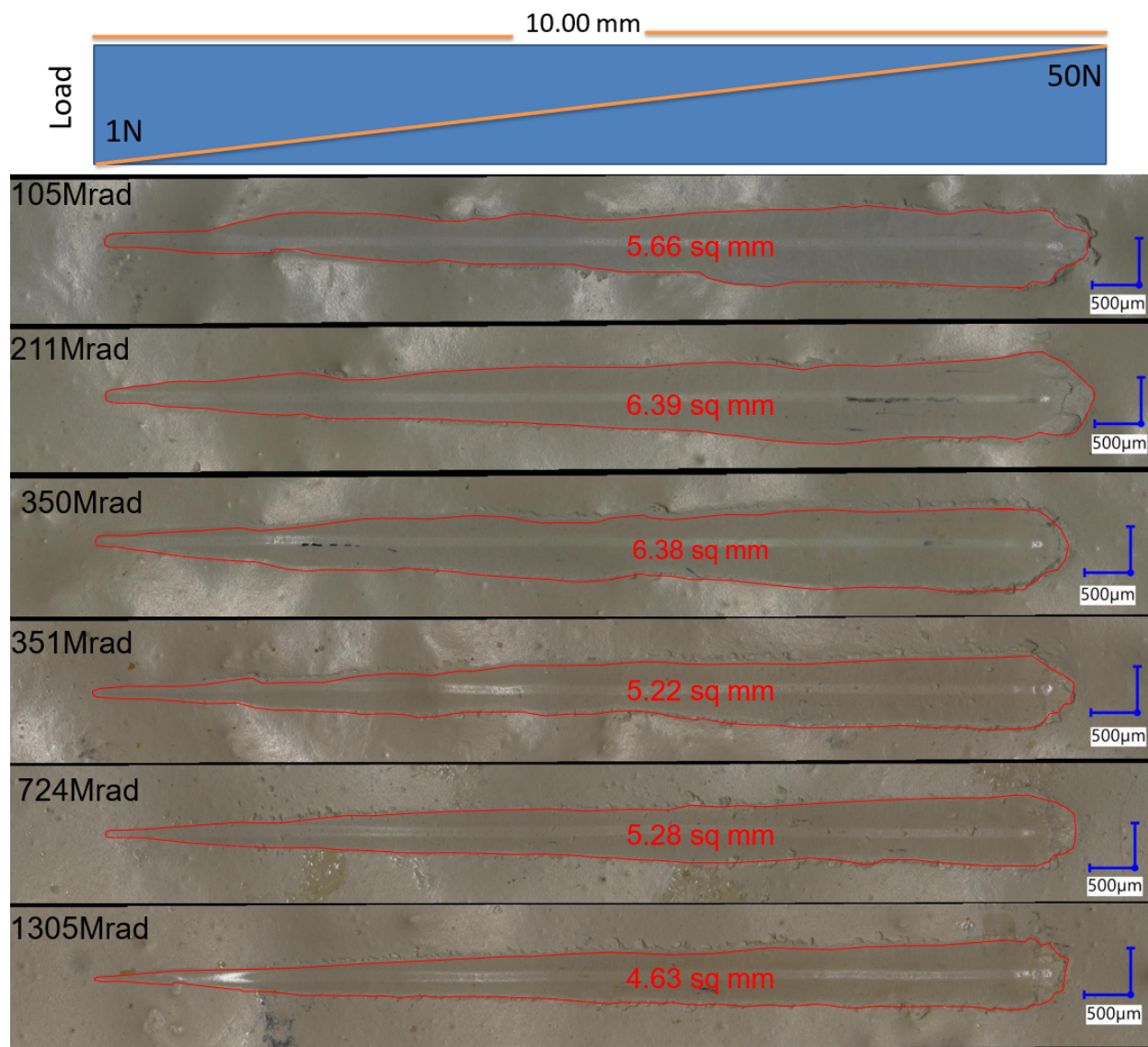


**Figure 39. Images of scratches performed on TDA-23-01-XX after irradiation. Scratch areas were calculated in Bluebeam Inc. image processing software by outlining the plastically deformed area.**

Figure 40 shows the stiffness of three polymeric coatings as a function of exposure to gamma radiation. The influence of self-heating for samples exposed in the shutter array is reflected in the increased stiffness of SA stiffness values. Overall, the polymeric coatings appeared to have roughly the same stiffnesses and exhibited the same behavior with increasing dose. The TDA-23-01-XX results are contradictory of the nanoindentation results (Section 4.3.1, which showed softening of the coating) probably due to the sliding and highly destructive nature of the scratch test and lack of sensitivity to the surface properties (represents the bulk). Nanoindentation has a much higher surface sensitivity due to higher resolution of depth measurements. Further investigation into the best method for measuring stiffness/hardness will be performed.

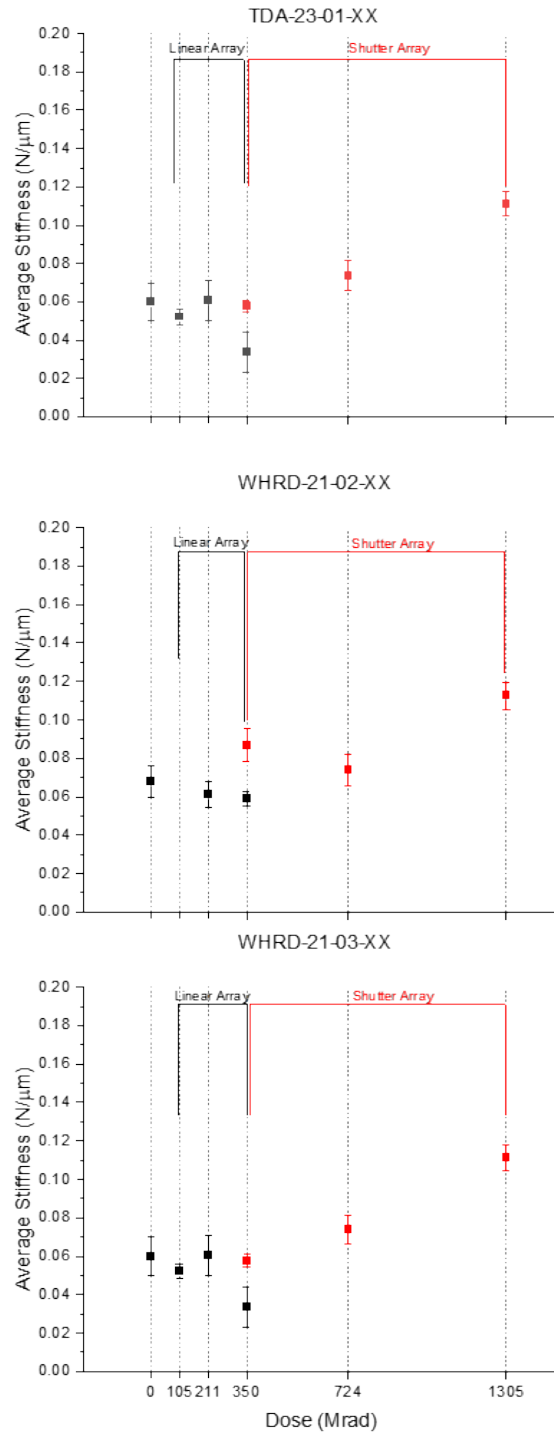


**Figure 40 Stiffness vs gamma radiation dose derived from scratch testing data for three polymeric coatings.**

Image analysis of the scratch area (Figure 41) for TDA-23-01-XX shows agreement with stiffness change with increasing dose (Figure 40). A decreased scratch area represents a harder material since the forces in

the scratches were kept the same. The self-heating effect in the SA appears to result in hardening and decreased scratch area at all doses.

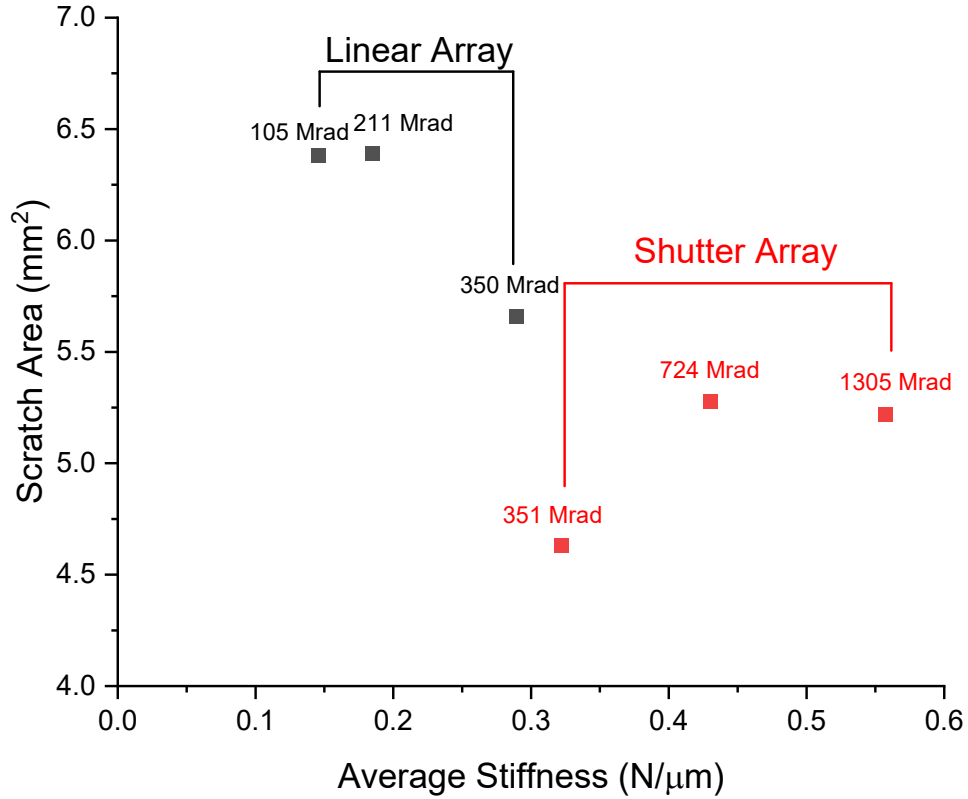


Figure 41 Scratch area vs average stiffness for TDA-23-01-XX. Scratch area was measured from image data. Decreased scratch area represents an increase in material stiffness.



## 4.4 Electrochemical Properties

The electrochemical properties of the coatings were evaluated as a function of radiation dose. These tests were performed to evaluate how radiation affects the ability of the coating to prevent corrosion. Because some of the coatings offer no path for ion or charge transfer through the coating, only some of the coatings were evaluated. Specifically, polarization scans were performed on the ceramic-hybrid coatings (FC-23-01-XX, LUNA-23-03-XX) and the samples with the Zn-rich primers (TDA-23-02-XX and LUNA-23-04-XX) when exposed to 0, 105, 211, 350, 724, and 1305 Mrad.

### 4.4.1 Chemical and Electrochemical Properties

Cyclic potentiodynamic polarization (CPP) scans were performed on FC-23-01-XX, TDA-23-02-XX, LUNA-23-03-XX, and LUNA-23-04-XX to gain a better understanding of the corrosion resistance and pitting susceptibility following exposure to canister relevant gamma radiation for each of the coating candidates. All CPP scans were run in triplicate under the specific conditions and parameter settings. Coupons were run individually in electrochemical flat cells with 0.6 M quiescent sodium chloride aqueous solution at room temperature, where a surface area of approximately 1.267 cm<sup>2</sup> was exposed on each coupon (Figure 42). An open circuit potential (OCP) was acquired for 1 hour prior to the start of each CPP scan. It should be noted that data was not collected for thicker or more capacitive coatings including WHRD-21-02-XX, WHRD-21-03-XX, OPM-23-01-XX, and TDA-23-01-XX due to potential overloads exceeding this range. CPP scans were performed using a scan rate of 0.167 mV/sec and had a potential range of -0.2 V vs OCP to 1.2 V vs Ag/AgCl, respectively. Once the scan reached 1.2V, it was reversed down to -0.5 V Ag/AgCl. In the plots showing the CPP scans, Figure 43 - Figure 46, the initial potentiodynamic scan (sweep from -0.2 V to 1.2 V) is labeled as prime, Run X' (where X = 1, 2, or 3 corresponding to the sample run) is a lighter color. The reverse scan from 1.2 V to -0.5 V is denoted without apostrophe, Run X (where X = 1, 2, or 3 corresponding to the sample run), and is a darker color. The first OCP scan (e.g. Runs 1') represents the coating + coupon after irradiation, but before any corrosion has taken place. The second OCP scan represents the coating + coupon response to radiation and corrosion. The instability in the OCP value may indicated potential breakdown of the coating. In addition to measuring the OCP, the bend over potential ( $E_{\text{bend}}$ ) and the passive current density ( $i_{\text{pass}}$ ) were also evaluated for each coating tested as a function of dose received.

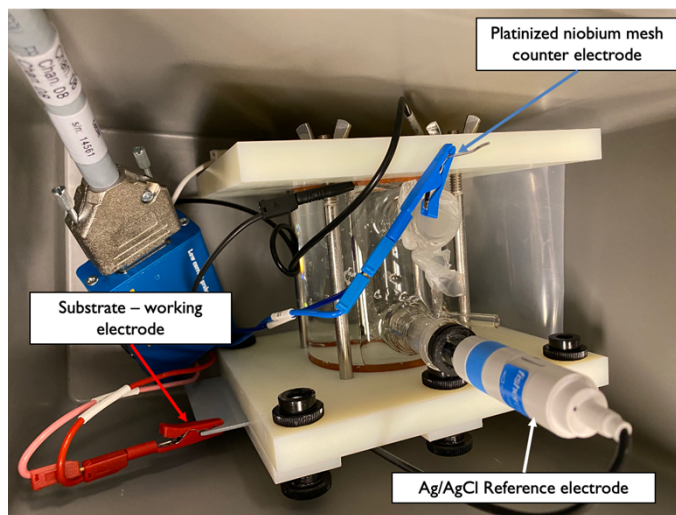
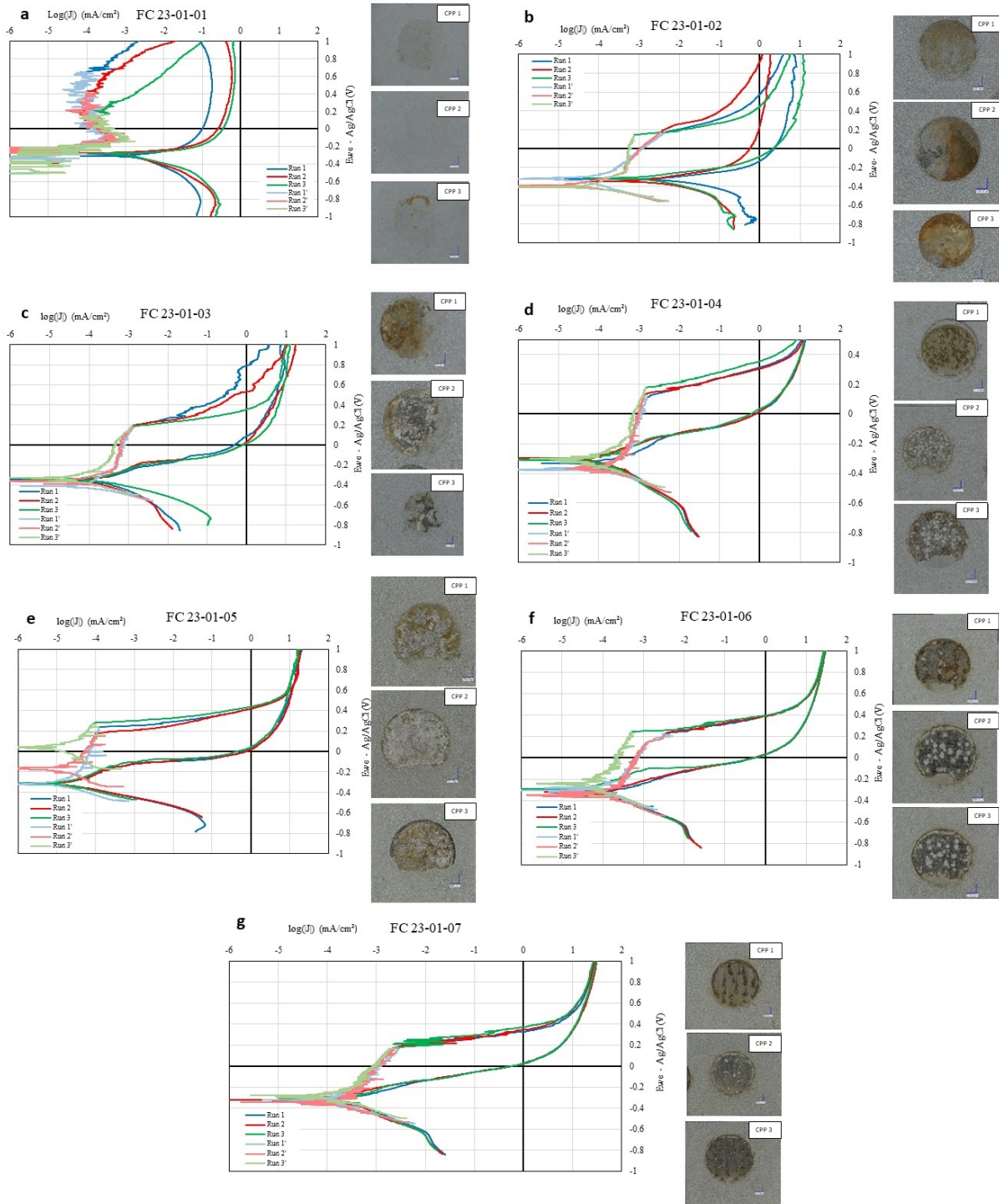


Figure 42. Three-electrode electrochemical cell for electrochemical measurements

The results are shown in Figure 43 - Figure 46, along with corresponding images of the areas post-test to link visual changes in the sample to the measured electrochemical behavior. The CPP scans provide a detailed understanding of the pitting corrosion that may be occurring. Also, these scans allow evaluation of metastable pitting to quantify the material's transition from a stable passivation regime into an active corrosion regime. This transition can occur above the 'V' pitting potential, however the  $E_{\text{bend}}$  reported here is the potential onset for active pitting corrosion for a specific sample. In these experiments, this transition was determined by visually estimating the inflection point on each plot for each run, then averaging the three run potentials to produce one  $E_{\text{bend}}$  value per testing condition. The passive current density was measured at this point. It is also shown for each sample and averaged in a similar way.

Corrosion was observed in the baseline sample, FC-23-01-01, as well as all samples which were exposed to gamma radiation. The severity of the corrosion appeared to increase with increasing radiation dose suggesting that the coating is degrading from the gamma radiation. The OCP was measured to be between -0.2V and -0.4V vs Ag/AgCl for the majority of the tests, which is likely due to penetration of the coating to the SS substrate [20-22]. There is a relationship between metastable pitting intensity versus radiation dosage. As radiation dose increases, the metastable pitting region becomes more pronounced. Inspection of the CPP locations following the test showed that the size and depth of the corrosion pits increased with increasing dose, suggesting more aggressive corrosion was occurring as the coating was becoming less protective. A rust color was present on test areas from all the radiation doses. After receiving 1305 Mrad, FC-23-01-07 showed clear evidence of cracking across the surface, which likely allowed for the brine to easily pass through the coating and attack the metal surface (Figure 43 g). The increase in corrosion damage in the FC-23-01-XX coating was likely due to the degradation of the polyurethane linker. This linker helps provide flexibility in the coating and increases the adhesive strength. As the polyurethane linker degrades, the coating provides less protection to the SS surface and more easily delaminates.



**Figure 43. Polarization scans of FC-23-01-XX following gamma irradiation to a) 0 Mrad, b) 105 Mrad-LA, c) 211 Mrad-LA, d) 350 Mrad-LA, e) 351 Mrad-SA, f) 724 Mrad-SA, and g) 1305 Mrad-SASA**

Similar to the FC-23-01-XX samples, the LUNA-23-03-XX samples had observable pitting at every radiation intensity. However, in 2 of the 3 CPP scans of the baseline sample little to no corrosion was observed. For Run 1 of the unirradiated sample, no corrosion is observed in either the CPP scan or image. Run 2 CPP shows two regions where corrosion occurred. The third run has visible corrosion in both the CPP plot as well as the image – though minor compared to samples that had been irradiated. When exposed to 105 Mrad, one run appears to have resisted corrosion; however, the other two runs did corrode. This result demonstrates the stochastic behavior of both radiation damage in coatings as well as corrosion processes. Increasing radiation leads to further corrosion in all runs. The OCP value also tends to shift more negative, except for the 350 Mrad- LA condition where it appears to hover around -0.2V vs Ag/AgCl. As can be seen by the images, the pit structure transitions from tunneling along the surface at the lowest radiation dosage, to deep pitting at higher radiation dosages. Like FC-23-01-XX, the degradation that is occurring on the LUNA-23-03-XX sample is likely driven by the radiolytic degradation of the polyurethane linker. In fact, in the sample exposed to 1305 Mrad, it appears that much of the coating has been removed from the surface during the exposure.

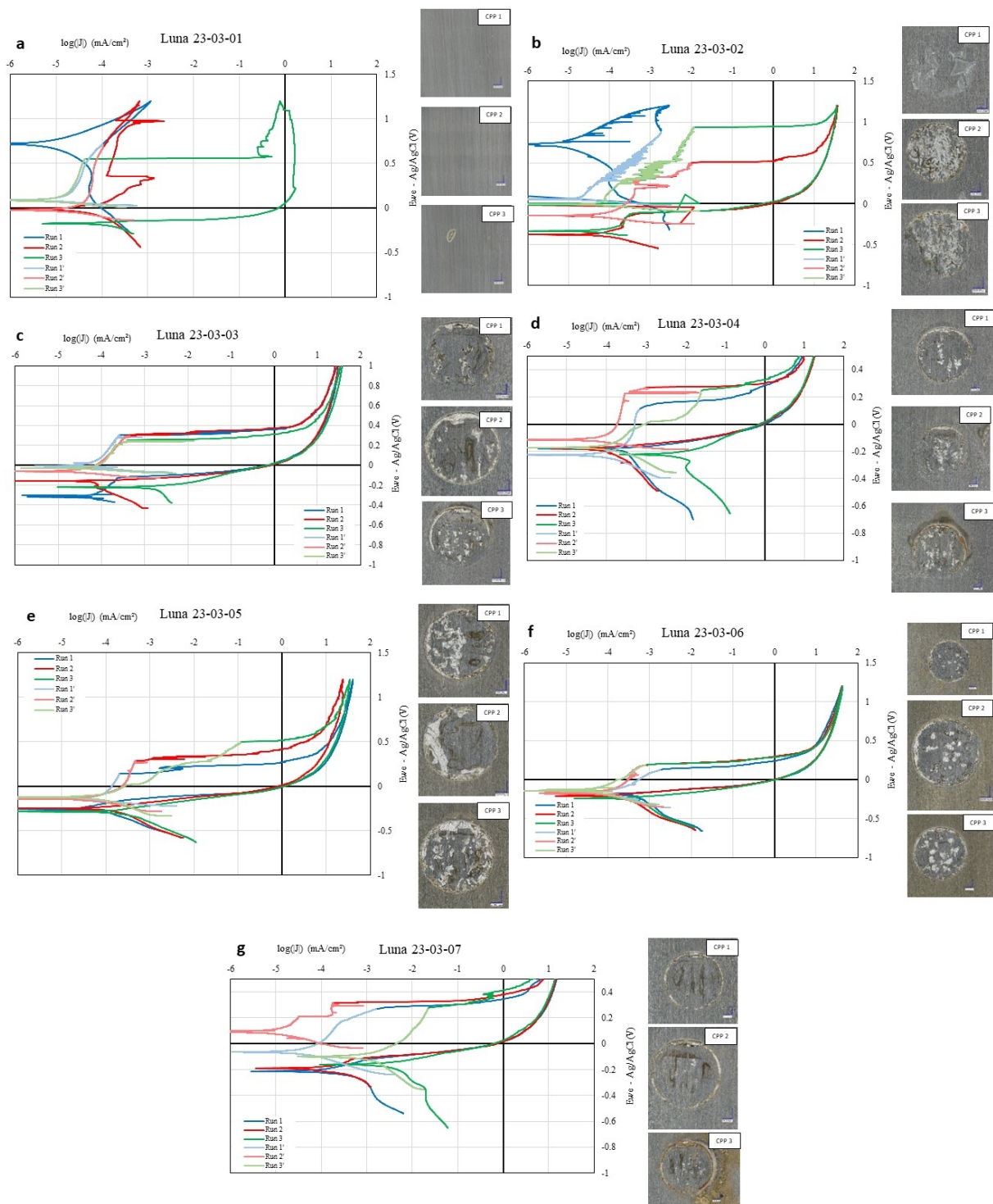
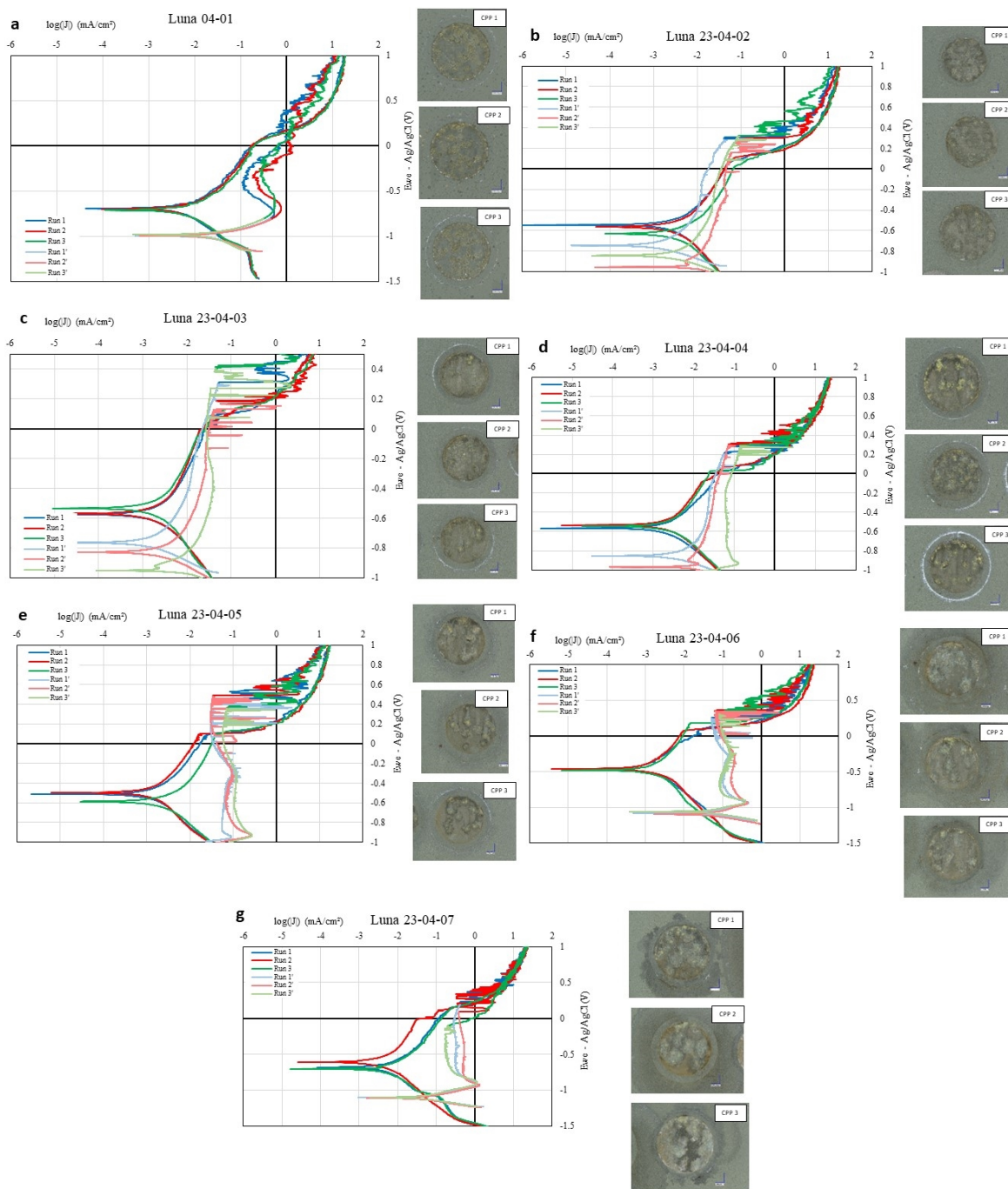


Figure 44. Polarization scans of LUNA-23-03-XX following gamma irradiation to a) 0 Mrad, b) 105 Mrad-LA, c) 211 Mrad-LA, c) 350 Mrad-LA, e) 351 Mrad-SA, f) 724 Mrad-SA, and g) 1305 Mrad-SA.

The CPP scans for the final two samples, LUNA-23-04-XX and TDA-23-02-XX are more complex due to the presence of the Zn-rich primer being active in the measurement. The LUNA-04-XX sample is a Zn-rich primer with the LUNA-23-03-XX coating as a topcoat.  $E_{\text{bend}}$  and Current density values were not able to be determined for the un-radiated sample because the CPP scan is dominated by the Zn oxidation, and thus the scan appears as active corrosion. As Zn oxidizes, it provides protection to the SS surface. For the radiated samples, the first OCP is located at -0.8V vs Ag/AgCl or more negative. This is believed to be due to activity of the Zn. The second OCP peak is significantly more positive. This is believed to be due contributions from the SS. On the first OCP sweep, there is still Zn left in the coating to oxidize and form a protective layer. But once the potential is positive enough, the coating gives way and the sample enters the SS corrosion regime. On the sweep back down, one of two things occurs, either 1) all the Zn has been corroded away, or 2) the Zn/Fe form a mixed potential more positive than the initial OCP. Both scenarios indicate the SS coupon is corroding and the coating no longer provides protection. On the anodic branch of the first OCP, the V-J line bends back on itself. It is believed this is characteristic of anodic behavior metallic species [77], specifically the formation  $\text{Zn}(\text{OH})_2$  or ZnO [78]. Metastable pitting is present in some of the runs, though the trend is not as clear as the trend in other coatings, such as the FC-23-01-XX sample.



**Figure 45. Polarization scans of LUNA-23-04-XX following gamma irradiation to a) 0 Mrad, b) 105 Mrad-LA, c) 211 Mrad-LA, d) 350 Mrad-LA, e) 351 Mrad-SA, f) 724 Mrad-SA, and g) 1305 Mrad-SA.**

The TDA-02-XX sample contains Zn-rich primer with corrosion resistant inhibitors. Unlike the LUNA-23-04-XX sample, this sample does not have a topcoat to decrease the Zn oxidation rate. Samples show a strong interaction between Zn oxidation and the radiation dose received. The unirradiated sample is the only condition where all three experiments have a second OCP below -0.5V vs Ag/AgCl. This is

suspected to be a mixed potential of Zn and Fe in the SS or possibly do to the mixed potential between Zn and the corrosion additives in the coatings. All irradiated samples have beginning OCPs around -1.0V vs Ag/AgCl. The second OCP values range between -0.3V to -0.6V vs Ag/AgCl. As the radiation dose increases, there is more hysteresis between OCP values between runs. For the sample exposed with the LA (105,211, and 350 Mrad), all three runs are similar in shape and OCP values. Samples exposed using the SA (351, 724, and 1305 Mrad), the OCPs between runs begin to drift and vary in value more. For example, at 1305 Mrad exposure, Run 1 had an OCP around -1V vs Ag/AgCl which corresponds to a Zn OCP, however after anodic polarization and a reverse scan, an ending OCP of -0.5V vs Ag/AgCl is observed– which is a suspected mixed potential between Zn and Fe. Runs 2 and 3 have beginning OCP values around -0.6V vs Ag/AgCl- again likely a mixed potential between Zn and Fe and ending OCP values around -0.3V vs Ag/AgCl, which more closely aligns with Fe in SS. This suggests the Zn is sacrificed during radiation exposure, and once the Zn is depleted, corrosion of the SS begins. The idea of Zn sacrifice is further strengthened by the images taken of the samples post CPP testing. One hypothesis to explain the discoloration around the outside of the CPP test area is that Zn could be migrating in to protect the coupon from corrosion. Future work will evaluate the chemical composition of the different colored regions in the CPP analyzed areas to identify which chemical species are formed on the surface. This will further inform the state of the coating and the degree of protection offered to the SS surface.



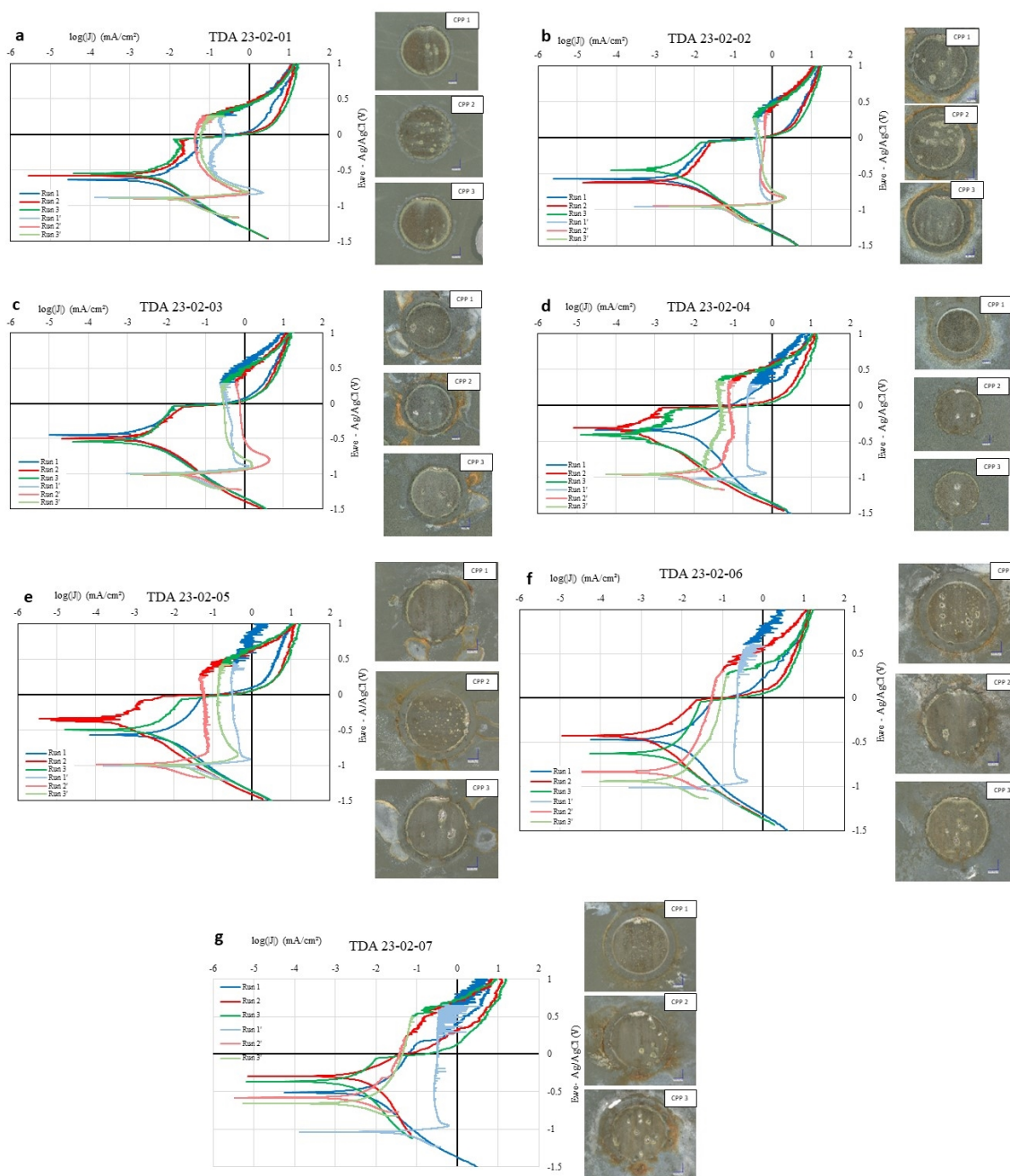


**Figure 46. Polarization scans of TDA-23-02-XX following gamma irradiation to a) 0 Mrad, b) 105 Mrad-LA, c) 211 Mrad -LA, c) 350 Mrad- LA, e) 351 Mrad -SA, f) 724 Mrad -SA, and g) 1305 Mrad-SA.**

Only TDA-23-02-XX has a clear trend for  $E_{\text{bend}}$ : as radiation dosage increases, the potential becomes more positive. The other three samples show no such relationship. The two samples containing a Zn-rich primer (Luna-23-04-XX and TDA-23-02-XX) have higher current densities compared to the polymer/silica coatings (FC-23-01-XX and Luna-23-03-XX), which is expected as Zn is electrically conductive and is actively oxidizing during the experiment. One possible reason for the lack of a clear

relationship between dose and either  $E_{\text{bend}}$  or current density is the fact that the surface area may be changing as the coating degrades and corrosion is occurring.

In conclusion, all four coatings tested showed different electrochemical responses; however, in general it was clear that radiation impacted the electrochemical performance of these coatings. This suggests that—even at relatively low doses—the ability of these coatings to protect the SS surface is impacted, which may necessitate a waiting period prior to coating and use of these types of coatings in **ex situ repair/mitigation** type applications only. Specifically, the FC-23-01-XX coating had a correlation between metastable pitting intensity and radiation dosage. As radiation dose increased, metastable pitting increased. The LUNA-23-03-XX samples tend to have their OCPs shifted more negative towards -0.2 vs Ag/AgCl. The Luna-23-04-XX coatings had strong Zn electrochemical activity, and their OCPs shift more positive. The TDA-23-04-XX samples also have OCP values which shift more positive. The beginning OCP values for the LUNA-23-04-XX and TDA-23-02-XX coatings are suspected to be due to Zn sacrificial corrosion. Additional information regarding the degree of coating degradation will be evaluated by SEM/EDS and XRD to identify the composition of the phases that exist following the CPP scan. Lastly, experimental modifications or different approaches will be used to try to evaluate the electrochemical behavior of the more capacitive coatings (OPM-23-01-XX, WHRD-21-02-XX, WHRD-21-03-XX, and TDA-23-01-XX).

## 5. FUTURE WORK

Future work plans to encompass two main thrusts for demonstrating the feasibility of coatings for use on SNF storage canisters: continue isolated coating performance tests and simulated application testing. These planned tests will both inform how the coatings will perform in the range of environments seen on the canister surface as well as identify the range of implementation conditions for when a coating could be successfully applied to a canister.

### 5.1 Isolated Coating Performance Tests

Isolated coating performance, specifically electrochemical, mechanical, radiolytic and thermal behavior, is critical to demonstrate that the properties of the coatings do not breakdown when exposed to accelerated environmental and mechanical conditions. Completion of these tests would ideally yield a coating that is corrosion resistant, is mechanically robust, and has limited susceptibility to thermal and radiolytic degradation in accelerated conditions. Specifically, planned future isolated performance tests include:

- Evaluate the combined effects of thermal and radiolytic exposures by performing gamma irradiation experiments at the GIF. This test would use the SA while holding coupons at canister relevant temperatures (150°C and 225°C) for the entirety of the exposure. This test will help identify the survivability of a given coating in a **prevention** application scenario and provide definitive evidence if use in the scenario is viable.
- Perform more detailed thermal analysis by performing head space gas analysis on samples exposed to long isothermal holds (for example 150°C for 3-6 months). These results will provide us with compositional analysis of the outgassing species to verify that these materials are or are not creating corrosive or other problematic species as they degrade.
- Continue adhesion testing to quantify Type 1 failure in all the coatings. Specifically, identify a primer or surface activation method [75] for PEKK coatings (OPM-23-01-XX) to enable more informative adhesion testing. Adhesion testing to date has shown failure in most of the coatings however further refinements are required for a more detailed, quantitative understanding of the adhesive properties of the most robust coatings.
- Complete electrochemical analyses of atmospherically exposed samples and perform electrochemical analysis on irradiated coupons to determine if corrosion resistance is affected by radiological exposure. A detailed electrochemical assessment on the impact of atmospheric corrosion and gamma irradiation will provide a more complete understanding of coating performance under specific conditions that will inform coating behavior on the canister.
- Perform salt/atmospheric exposure testing on the irradiated coupons and evaluate the combined effective radiation and atmospheric corrosion via mechanical, chemical, and electrochemical analyses. These tests will provide evidence regarding the ability of the coating to withstand a corrosive environment as a function of radiolytic degradation.

### 5.2 Simulated Application Testing

Application testing is necessary to demonstrate the feasibility of coatings for use in real-world application scenarios. For example, application of a coating onto a hot, salt/dust-covered surface mimicking the canister surface (such as would be found after years of storage) or application of a coating to a surface held at a constant canister-relevant temperature for many years, would present many more challenges than experienced in a laboratory-controlled setting. A number of the proposed tests will take multiple years to complete, since the goal is to avoid accelerated testing and the need for collaboration.

Specifically, some of these planned tests include:

- Facilitate coatings vendor participation in Hanford Lead Canister coatings panel exposure project led by PNNL. While this project involves the storage of Cs/Sr capsules and not SNF, the opportunity to apply the coatings to an in-field test canister with a known, elevated thermal environment will be a critical step to help determine the application viability of these coating candidates.
- Perform a rigorous surface preparation study to evaluate whether feasible surface preparation methods are sufficient to ensure a coating can adhere to a canister surface, especially after prolonged storage. In doing so, a better understanding of the possible surface preparation methods will be determined. Additionally, it is important to evaluate the possibility of reapplication. It will be important to determine if reapplication is possible and what surface preparation would be required to do so.
- Explore implications of applying coatings on a heated surface. The curing requirements for the coating candidates vary from one to another, however unless a coating is applied prior to loading SNF, it is likely the coating will be applied to a hot surface. It is unknown what the impact of applying the coating to a heated surface will have on the coating performance and must be evaluated.
- Perform corrosion tests on coating interfaces between bare SS surface and coating. Evaluating the coating/SS interface will be very important because it is likely that many mitigation and repair technologies would be applied as a patch on a specific area. This requires a detailed understanding of the performance and aging of that that interface to ensure that the material is not more susceptible due to crevice corrosion or delamination.

## 6. CONCLUSIONS AND IMPLICATION OF COATING PERFORMANCE FOR CANISTER USE

The results obtained in FY23 have provided strong differentiation between coating types and their potential feasibility for use on SNF canisters. At the beginning of the year, a fifth coating vendor was added to the MOU, a down-selection (in response to a qualitative comparison) was performed to focus experimental efforts on the most promising candidate coatings, and a new batch of coated coupons received more rigorous testing. Thermal analysis was performed on the as-received coatings. A subset of the new coupons was exposed to canister-relevant doses of gamma radiation at highly accelerated dose rates. The irradiated coatings were compared to the as-received coatings through visual inspection, along with mechanical and electrochemical evaluation.

Major advances were made in the measurement of coating thermal behavior at canister-relevant temperatures, showing that most coatings outgas water or carbon dioxide and that some coatings did not outgas or react with the environment until extremely high temperatures – beyond the scope of this application. Further, mass loss for most coatings did not begin until well after 150°C which qualifies them (thermally) as a repair coating once the maximum surface temperature is below 150 °C. This serves as early evidence that coatings meet the “first, do no harm” criterion required to be considered for application on new or existing SNF canisters.

Three coatings (LUNA-23-03-XX, TDA-23-01-XX, and FC-23-01-XX) exhibited obvious color changes with increasing dose, while the remaining coupons appeared unchanged (calorimetrically). Color change itself does not necessarily demonstrate severe degradation but has been used in the past as an indicator for changes (deleterious or beneficial) in coatings.

The influence of gamma radiation on the mechanical behavior of the coatings was mixed. For some coatings (OPM-23-01-XX, LUNA-23-04-XX, and TDA-23-02-XX), the coatings did not appear to be affected or were minimally affected by gamma radiation up to 1300 Mrad. OPM-23-01-XX did not fail during adhesion testing but showed increased surface bonding strength (between the test dolly and the coating) with increasing dose. When exposed to 100 Mrad, all the coatings (except for OPM-23-01-XX) exhibited >250 psi decrease in adhesion strength when compared to as-received coatings. The adhesion failure mode also varied in some coatings as a function of radiation. For example, when irradiated at lower doses (<351 Mrad) TDA-23-01-XX exhibited Type 2 cohesive failure and Type 1 adhesive failure was observed at higher doses (>724 Mrad). Nanoindentation showed that LUNA-23-03-XX and TDA-23-01-XX softened when exposed to gamma radiation. The nanoindentation tests are ongoing and will be completed in FY24.

Electrochemical measurements (CPP) were performed on coatings to determine the pitting and repassivation potentials of some baseline and irradiated coupons. The coatings evaluated showed obvious degradation in corrosion resistance with increased radiation dose. The thick, polymeric coatings (i.e., OPM-23-01-XX, WHRD-21-02-XX, WHRD-21-03-XX, and TDA-23-01-XX) could not be evaluated using CPP due to its extremely resistive behavior (i.e., open circuit potential could not be measured as there was no pathway for ionic conduction).

Figure 47 shows an updated qualitative comparison of the results collected to date on all candidate coatings. Green is denoted as having good relative performance for application on SNF canisters, while red indicates the coating would need to be improved before being considered for use. Based upon these specific performance tests during FY22-FY23, the polymeric coatings performed well. OPM-23-01-XX shows strong potential for use across a wide range of possible exposure environments. The WHRD-21-02-XX and WHRD-21-03-XX, also demonstrate promising behavior, although its application may be limited to **mitigation** or **repair** once the canister surface temperature has decreased considerably. TDA-23-01-XX generally performed well, however the dramatic color change as a function of radiation

coupled with the change in adhesion suggests that radiation damage may be an important consideration for its use on a SNF canister. The ceramic hybrid coatings, including FC-23-01-XX and LUNA-23-03-XX were also susceptible to radiation – likely arising from the degradation of the polyurethane linker. This observed degradation had a deleterious impact on the corrosion testing. Lastly, the samples with the Zn-rich primer (LUNA-23-04-XX and TDA-23-02-XX) showed promising resistance to simulated atmospheric conditions (TDA-23-02-XX was not tested yet), and performed well in thermal tests, however the baseline mechanical durability of the coating and the radiation resistance need improvement.

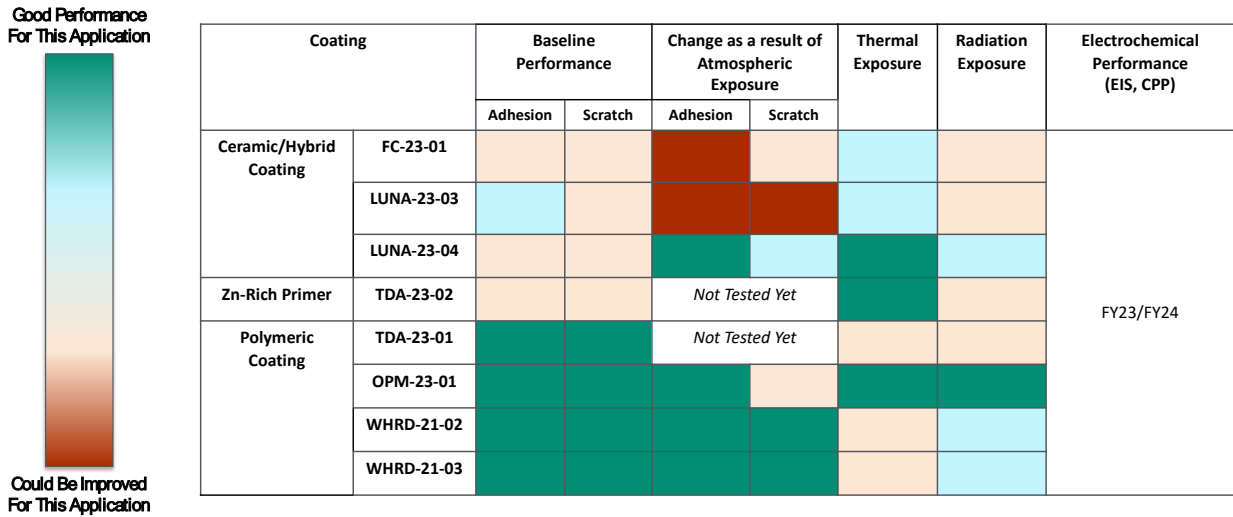


**Figure 47. Qualitative comparison of results to date on all coatings.**

## 7. REFERENCES

1. Knight, A., et al., *FY22 Status: Corrosion-Resistant Coatings on Spent Nuclear Fuel Canisters to Mitigate and Repair Potential Stress Corrosion Cracking* D.o. Energy, Editor. 2022, Sandia National Laboratories: Albuquerque, New Mexico.
2. Knight, A., et al., *FY21 Status Report: SNF Canister Coatings for Corrosion Prevention and Mitigation*. 2021, Sandia National Laboratories: Albuquerque, New Mexico.
3. Knight, A.W., et al., *Corrosion-Resistant Coatings for Mitigation and Repair of Spent Nuclear Fuel Dry Storage Canisters*. 2020, Sandia National Laboratories Albuquerque, New Mexico.
4. Schindelholz, E., Bryan, C., Alexander, C., *FY17 Status Report: Research on Stress Corrosion Cracking of SNF Interim Storage Canisters*. 2017, Sandia National Laboratories.
5. Bryan, C. and E. Schindelholz, *FY18 Status Report: SNL Research into Stress Corrosion Cracking of SNF Interim Storage Canisters*. 2018, Sandia National Laboratories: U.S. Department of Energy.
6. Schaller, R., et al., *FY19 Status Report: SNL Research into Stress Corrosion Cracking of SNF Dry Storage Canisters*. 2019, Sandia National Laboratories
7. Schaller, R.F., et al., *FY20 Status Report: SNF Interim Storage Canister Corrosion and Surface Environment Investigations*. 2020, Sandia National Laboratories.
8. Schaller, R., et al., *FY22 Status for Corrosion and Surface Environment Investigations*. 2022: Albuquerque, New Mexico.
9. Bryan, C., et al., *FY21 Status Report: SNF Interim Storage Canister Corrosion and Surface Environment Investigations*. 2021, Sandia National Laboratories.
10. Gilkey, L., et al., *Probabilistic Model for Stress Corrosion Cracking of SNF Dry Storage Canisters*, D.o. Energy, Editor. 2022, Sandia National Laboratories: Albuquerque, New Mexico.
11. Bryan, C. and D. Enos, *Analysis of Dust Samples Collected from Spent Nuclear Fuel Interim Storage Canisters at Hope Creek, Delaware, and Diablo Canyon, California*. 2014, Sandia National Laboratory: Albuquerque, NM.
12. Bryan, C. and D. Enos, *Analysis of Dust Samples Collected from an Unused Spent Nuclear Fuel Interim Storage Container at Hope Creek, Delaware*. 2015 Sandia National Laboratories: Albuquerque, NM
13. Bryan, C. and A.W. Knight, *Analysis of Dust Samples Collected from an Inland ISFSI Site ("Site A")*. 2020, Sandia National Laboratories: Albuquerque, NM.
14. Knight, A.W. and C. Bryan, *Analysis of Dust Samples Collected from an Inland ISFSI Site ("Site B")*. 2020, Sandia National Laboratories: Albuquerque, NM
15. NRC. *NRC Maps of Independent Spent Fuel Storage Installations (ISFSI)*. 2021 [cited 2022 July 6, 2022].
16. Bryan, C. and D. Enos, *SNF Interim Storage Canister Corrosion and Surface Environment Investigations. FCRD-UFD-2015-00511*. 2015 Sandia National Laboratories: Albuquerque, NM.
17. Bryan, C. and D. Enos, *SFY16 Status Report: SNF Interim Storage Canister Corrosion and Surface Environment Investigations. FCRD-UFD-2015-00511*. 2016, Sandia National Laboratories: Albuquerque, NM.
18. Bryan, C. and E. Schindelholz, *Analysis of Samples Collected from the Surface of Interim Storage Canisters at Calvert Cliffs in June, 2017: Revision 01*. 2017, Sandia National Laboratories Albuquerque NM.
19. Enos, D. and C. Bryan. *Understanding the Risk of Chloride Induced Stress Corrosion Cracking of Interim Storage Containers for the Dry Storage of Spent Nuclear Fuel: Evolution of Brine Chemistry on the Container Surface*. in *CORROSION 2016. NACE 2016*. Vancouver, B.C. .
20. Katona, R.M., et al., *Importance of the hydrogen evolution reaction in magnesium chloride solutions on stainless steel*. *Corrosion Science*, 2020. **177**: p. 108935.

21. Katona, R.M., et al., *Use of in situ Raman spectroelectrochemical technique to explore atmospheric corrosion in marine-relevant environments*. Electrochemistry Communications, 2020. **118**.
22. Katona, R.M., et al., *Quantitative assessment of environmental phenomena on maximum pit size predictions in marine environments*. Electrochimica Acta, 2021. **370**: p. 137696.
23. Schaller, R.F., et al., *FY20 Status Report: SNF Interim Storage Canister Corrosion and Surface Environment Investigations*. 2020: U.S. Department of Energy. p. M2SF-21SN010207055.
24. Bryan, C.R., et al., *Physical and chemical properties of sea salt deliquescent brines as a function of temperature and relative humidity*. Science of The Total Environment, 2022. **824**: p. 154462.
25. Ross, K., et al., *Investigation of Cold Spray as a Dry Storage Canister Repair and Mitigation Tool*. 2020, Pacific Northwest National Laboratory.
26. NRC, *Potential Chloride-Induced Stress Corrosion Cracking of Austenitic Stainless Steel and Maintenance of Dry Storage System Canisters*, U.S.N.R. Commission, Editor. 2012: Washington, DC.
27. *Dry Cask Storage System Welded Stainless Steel Canister Repair and Mitigation Guidance for Application and Acceptance 2021*, EPRI: Palo Alto, California.
28. Escp, E., *Canister mitigation & repair epri escp*. 2019.
29. Tatman, J., *Welding and Repair Technology Center: Extended Storage Collaboration Program Canister Mitigation and Repair Subcommittee – Industry Progress Report*. 2018.
30. Knight, A., et al., *FY22 Update: Development of Surface Sampling Techniques for the Canister Deposition Field Demonstration 2022*, Sandia National Laboratories: Albuquerque, New Mexico.
31. Wittman, R., *Radiolysis Model Sensitivity Analysis for a Used Fuel Storage Canister*, D.o. Energy, Editor. 2013, Pacific Northwest National Laboratory: Richland, Washington.
32. Bryan C.R., et al., *FY21 Status Report: SNF Interim Storage Canister Corrosion and Surface Environment Investigations*. 2021, Sandia National Laboratories: US Department of Energy Spent Fuel and Waste Science and Technology.
33. Pritchard, G., *Anti-corrosion Polymers: PEEK, PEKK and Other Polyaryls*. 1994: Rapra Technology Limited.
34. Kemmish, D., *Update on the Technology and Applications of Polyaryletherketones*. 2010: ISmithers.
35. Choupin, T., *Mechanical performances of PEKK thermoplastic composites linked to their processing parameters*. 2017, Ecole nationale supérieure d'arts et métiers - ENSAM, France.
36. Alqurashi, H., et al., *Polyetherketoneketone (PEKK): An emerging biomaterial for oral implants and dental prostheses*. Journal of Advanced Research, 2020. **28**: p. 87-95.
37. Huttunen-Saarivirta, E., et al., *Corrosion protection of galvanized steel by polyimide coatings: EIS and SEM investigations*. Progress in Organic Coatings, 2011. **72**(3): p. 269-278.
38. Sezer Hicyilmaz, A. and A. Celik Bedeloglu, *Applications of polyimide coatings: a review*. SN Applied Sciences, 2021. **3**(3): p. 363.
39. Gao, H., et al., *Study on performances of colorless and transparent shape memory polyimide film in space thermal cycling, atomic oxygen and ultraviolet irradiation environments*. Smart Materials and Structures, 2017. **26**(9): p. 095001.
40. Gouzman, I., et al., *Advances in Polyimide-Based Materials for Space Applications*. Advanced Materials, 2019. **31**(18): p. 1807738.
41. Nagaraj, S. and S.P. Kumaresh Babu, *Protective polyurea coating for enhanced corrosion resistance of sole bars in railway coaches*. Materials Today: Proceedings, 2020. **27**: p. 2407-2411.
42. Feng, L. and J.O. Iroh, *Polyimide–polyurea copolymer coating with outstanding corrosion inhibition properties*. Journal of Applied Polymer Science, 2018. **135**(9): p. 45861.
43. Feng, L. and J.O. Iroh, *Corrosion resistance and lifetime of polyimide-b-polyurea novel copolymer coatings*. Progress in Organic Coatings, 2014. **77**(3): p. 590-599.



44. Feng, L. and J.O. Iroh, *Novel polyimide-b-polyurea supramacromolecule with remarkable thermomechanical and dielectric properties*. European Polymer Journal, 2013. **49**(7): p. 1811-1822.
45. Seymour, R.B., *The Chemical Resistance of Phenolic Resins*. Corrosion, 1951. **7**(5): p. 151-155.
46. *Sherwin-Williams Coatings Meet Strict NRC Requirements*, in *Paint and Coatings Industry*. 2010.
47. ASTM, *Standard Test Method for Effects of Gamma Radiation on Coatings for Use in Nuclear Power Plants*. 2017.
48. Garton, A., et al., *Additives for improving the strength, stiffness, and ductility of epoxy resins*. Polymer Engineering & Science, 1987. **27**(21): p. 1620-1626.
49. Pethrick, R.A., *Composite to metal bonding in aerospace and other applications.*, in *Welding and Other Joining Technologies*, M.K. Besharati-Givi and A.M. Chaturvedi, Editors. 2012, Woodhead Publishing. p. 288-319.
50. *Epoxy Resin: Flexible*. 2001 [cited 2020 July17]; Available from: <https://www.azom.com/article.aspx?ArticleID=651>.
51. Ding, R., et al., *Study on graphene modified organic anti-corrosion coatings: A comprehensive review*. Journal of Alloys and Compounds, 2019. **806**: p. 611-635.
52. Zheng, S. and J. Li, *Inorganic-organic sol gel hybrid coatings for corrosion protection of metals*. Journal of Sol-Gel Science and Technology, 2010. **54**(2): p. 174-187.
53. McMahon, M.E., et al., *A Review of Modern Assessment Methods for Metal and Metal-Oxide Based Primers for Substrate Corrosion Protection*. Frontiers in Materials, 2019. **6**: p. 190.
54. McMahon, M.E., J.T. Burns, and J.R. Scully, *Development of new criteria for evaluating the effectiveness of Zn-rich primers in protecting Al-Mg alloys*. Progress in Organic Coatings, 2019. **135**: p. 392-409.
55. McMahon, M.E., J.R. Scully, and J.T. Burns, *Mitigation of Intergranular Cracking in Al-Mg Alloys via Zn-Based Electrode Potential Control in Sodium Chloride Solution*. Corrosion, 2019. **75**(8): p. 911-928.
56. Amirudin, A. and D. Thierry, *Application of electrochemical impedance spectroscopy to study the degradation of polymer-coated metals*. 1995.
57. Murer, N. and J.-P. Daird *Introduction to EIS (Electrochemical Impedance Spectroscopy) with EC-Lab/EC-Lab Express*. 1-23.
58. Orazem, M.E. and B. Tribollet, *Electrochemical Impedance Spectroscopy*. 2017, Hoboken New Jersey: John Wiley & Sons Inc.
59. *Introducing EC-Lab® EIS quality indicators: THD, NSD and NSR*. 2018, Bio-Logic Science Instruments.
60. Cuta, J. and H. Adkins, *Preliminary Thermal Modeling of HI-STORM 100 Storage Modules at Diablo Canyon Power Plant ISFSI*, D.o. Energy, Editor. 2014, Pacific Northwest National Laboratory: Richland, Washington.
61. Suffield, S.R., et al., *Thermal Modeling of NUHOMS HSM-15 and HSM-1 Storage Modules at Calvert Cliffs Nuclear Power Station ISFSI*, D.o. Energy, Editor. 2012, Pacific Northwest National Laboratory: Richland, Washington.
62. *Thermogravimetric Analysis - TGA: Method, Technique and Applications*, N.G. GmbH, Editor.
63. *TA Instruments Thermal Analysis Product Brochure*, T. Instruments, Editor. 2010.
64. Tuck, C.D.S., M.E. Whitehead, and R.E. Smallman, *A fundamental study of the kinetics of zinc oxidation in the temperature range 320–415°C in atmospheres of pure oxygen and oxygen doped with gaseous impurities*. Corrosion Science, 1981. **21**(5): p. 333-352.
65. *RGA Application Bulletin #208 Spectra Reference*. 2005, MKS Instruments Inc. p. 2.
66. Whittman, R., *Radiolysis Model Sensitivity Analysis for a Used Fuel Storage Canister*. USDOE Used Fuel Disposition Campaign, 2013. **PNNL-22773, FCRD-UFD-2013-000357**.

67. Shulman, H. and W.S. Ginell, *Nuclear and Space Radiation Effects on Materials*. 1970, National Aeronautics and Space Administration.
68. Pastorelli, G., et al., *Environmentally induced colour change during natural degradation of selected polymers*. *Polymer Degradation and Stability*, 2014. **107**: p. 198-209.
69. Spencer, M., et al., *Color as a tool for quantitative analysis of heterogeneous polymer degradation*. *Materials Today Chemistry*, 2023. **29**: p. 101417.
70. Fifield, L.S., et al., *PNNL-31443 Inhomogenous Aging of Nuclear Power Plant Electrical Cable Insulation*, in *Light Water Reactor Sustainability Program*. 2021, US Department of Energy Office of Nuclear Energy.
71. ASTM, *A956-22 Standard Test Method for Leeb Hardness Testing of Steel Products*. 2022.
72. Celina, M., et al., *Overview of accelerated aging and polymer degradation kinetics for combined radiation-thermal environments*. *Polymer Degradation and Stability*, 2019. **166**: p. 353-378.
73. ASTM International, *D4541 – 17: Standard Test Method for Pull-Off Strength of Coatings Using Portable Adhesion Testers*. 2017.
74. Defelsko Corporation, *PosiTest AT Series Pull-Off Adhesion Testers*. 2021.
75. Younis, M., et al., *The impact of non-thermal plasma on the adhesion of polyetherketoneketone (PEKK) to a veneering composite system*. *Journal of the Mechanical Behavior of Biomedical Materials*, 2020. **112**: p. 104065.
76. ASTM international, *D7027 – 13: Standard Test Method for Evaluation of Scratch Resistance of Polymeric Coatings and Plastics Using an Instrumented Scratch Machine*. 2013.
77. Brusich, V., et al., *Corrosion and Protection of a Conductive Silver Paste*. *Journal of The Electrochemical Society*, 1995. **142**(8): p. 2591.
78. El-Sayed, A.E.-R., H.A.E.-S. Shilkamy, and M. Elrouby, *The passivity breakdown of zinc antimony alloy as an anode in the alkaline batteries*. *Scientific Reports*, 2022. **12**(1): p. 18925.

## **APPENDIX A.**

Irradiated coupons not conforming to standard numerical order described Table 2 in Section 2.2.4. This accommodation was needed due to the timing of when the irradiation experiment started and when samples were received or not.

<b>Dose Received</b>	<b>Coupon ID</b>		
105	OPM-23-01-02	WHRD-21-02-05	WHRD-21-03-05
211	OPM-23-01-03	WHRD-21-02-07	WHRD-21-03-07
350	OPM-21-01-15	WHRD-21-02-09	WHRD-21-03-09
351	OPM-23-01-05	WHRD-21-02-11	WHRD-21-03-11
724	OPM-23-01-06	WHRD-21-02-13	WHRD-21-03-14
1305	OPM-23-01-04	WHRD-21-02-15	WHRD-21-03-15